Carbon Dioxide in ultrapotassic silicate melts: Experimental insights on solubility and decompression induced vesicle nucleation

GEORG-AUGUST-UNIVERSITÄT
GÖTTINGEN

Dissertation

zur Erlangung des mathematisch-naturwissenschaftlichen Doktorgrades
"Doctor rerum naturalium"
der Georg-August-Universität Göttingen

im Promotionsprogramm Geowissenschaften / Geographie
der Georg-August-University School of Science (GAUSS)

vorgelegt von

Maximilian Schanofski

aus Dortmund

Göttingen 2021

Betreuungsausschuss

Erstbetreuerin: Dr. Sara Fanara
Zweitbetreuer: Dr. Burkhard C. Schmidt
Drittbetreuer: Prof. Dr. Andreas Pack

Prüfungskommision

Erstgutachterin: Dr. Sara Fanara
Zweitgutachter: Prof. Dr. Andreas Pack
Dr. Burkhard C. Schmidt
Prof. Dr. Sharon Webb
Dr. Lucia Pappalardo
Prof. Dr. Francoir Holtz

Tag der mündlichen Prüfung

03.09.2021

Abstract

Until today, the explosivity of volcanic eruptions cannot be forecasted by even the most modern monitoring techniques. The processes causing these events, endangering the lives of millions of people, happen deep inside the magma plumbing system. Some of these explosive eruptions are characterized by melts with high CO_2 contents that originate from CO_2 flushing directly from the Earth mantle or magma plumbing systems being rooted in carbonate substrata. In the latter case, CO_2 is produced by interaction of the magma with the carbonate basement leading to carbonate break-down and assimilation. Making use of high pressure high temperature experiments, this PhD project focuses on reproducing of magma storage conditions and simulating magma ascent processes to improve the knowledge on the role of CO_2 for volcanic degassing mechanisms and their effect on explosive volcanic eruptions.

The first study of this project focusses on the solubility of mixed CO_2-H_2O volatile phases in K-rich leucititic and phonolitic melts as a function of pressure to shed light on the storage conditions of those melts in the Earth's crust. Synthetic melt analogues to the composition of the Pozzolane Rosse eruption of the Colli Albani volcanic District 456 ka ago (SULm) and the famous 79 AD Mt. Somma-Vesuvius eruption (VES79) were used. Solubility experiments were carried out in an internally heated pressure vessel (IHPV) at 1250 °C a constant oxygen fugacity of NNO +3 ±1 and pressures between 50 and 300 MPa for fluid compositions of $X^{fl}_{H_2O}$= 0.0, 0.2, 0.4, 0.6, 0.8, 1.0. It was found that the highly depolymerized SULm melt is capable of dissolving a very large amount of CO_2 (up to 8500 ppm at 300 MPa) that is five times higher than in the polymerized VES79 composition at similar pressures. At the same time H_2O solubility is fairly similar in both compositions throughout the studied pressure range. Furthermore, evidence for a

depolymerizing effect of H_2O on the VES79 melt was found, leading to an elevated CO_2 solubility in CO_2-H_2O bearing samples.

In the second study we experimentally investigated the decompression induced volatile exsolution of mixed CO_2-H_2O bearing SULm melts that occurs during magma ascent through the crust. In an IHPV at 1250 °C, the pressure was decreased from 200 MPa to about 150, 100, 50 and 30 MPa at a fast, constant decompression rate of dP/dt= 1 MPa/s for sample series with $X^{fl}_{H_2O}$= 0.0, 0.5, 1.0. After rapidly quenching the samples to room temperature, optical analysis was done to obtain parameters important for interpretation of the melt degassing behavior such as vesicle number density (VND) and porosity. We successfully implemented a new procedure to enable porosity measurements of the entire sample capsule matching calculated porosities very well. To preserve the entire capsule, we used a diamond wire saw to cut the closed capsule in half with minimal damage to the fragile sample. One half of the sample is embedded in epoxy and polished before taking an image in reflected light. To improve the statistics for porosity and VND measurements, we polished the sample down by approx. 500 µm while taking a total of three pictures at different depths. We demonstrate that the exsolution mechanisms of H_2O strongly differ from those of CO_2. In contrast to the single homogeneous nucleation event of H_2O bubbles, CO_2 bearing melts tend to continuously nucleate new bubbles after surpassing the critical supersaturation pressure. In CO_2-H_2O bearing melts we found that CO_2 degasses exclusively at higher pressure before H_2O exsolves from the melt, rapidly decreasing the volatile supersaturation at low final pressure. We propose that this causes increased magma ascent rates at shallow depths (where H_2O exsolution starts) leading to enhanced volcanic explosivity.

The high CO_2 concentrations in the SULm melts are at the limit of analytical capability of the conventionally used infrared-spectroscopic technique in transmission. Here the peakheights of the carbonate doublet easily exceed two absorbance units (depending on the sample thickness). Since the dependence of the peakheight on the concentration is not linear in such a

case, the carbonate content of these samples cannot be quantitatively evaluated. To account for this problem we implemented a novel application in the third study, using micro Attenuated Total Reflectance (µ-ATR) FTIR Spectroscopy to quantify high CO_3^{2-} contents (> 0.17 wt%) in silicate glasses. µ-ATR analyses only a very restricted sample volume (< 10 µm depth). Here the carbonate signal shows absorbances that are roughly two orders of magnitude lower compared to transmission measurements. The spectra have shown to nicely separate the CO_3^{2-} doublet from the SiO_2 lattice vibration allowing for a simple straight baseline. A linear correlation coefficient of k= 2.28 ± 0.02 was determined for the studied SULm composition with CO_2 contents between 0.17 and 4.28 wt%.

Acknowledgements

My special thanks goes to **Sara Fanara** for giving me the chance to work on this project and for the supervision throughout my PhD studies even after leaving the University for a next step in her career. Over the years I had countless questions about experimental procedures and findings that were discussed with undivided attention and genuine interest. I always had enough freedom to follow my own ideas and really enjoyed the close collaboration and personal contact.

I am extremely thankful for the support of my second supervisor **Burkhard Schmidt** who spend countless hours with me interpreting data and teaching me experimental as well as analytical skills. I particularly thank him for becoming my first point of contact in the later stage of my PhD and for correcting the countless pages I handed to him towards the end of the project.

I thank **Sharon Webb** for her help regarding various viscosity related questions, as well as her support regarding any bureaucratic obsticles.

Thanks to **Andreas Pack** for being my third supervisor and for the constructive suggestions during discussions of the next steps for my research.

Thanks to **Kirsten Techmer** for the introduction to the SEM technique and her help with the SEM analysis required for this thesis.

I want to thank **Bettina Schlieper-Ludewig**, **Marina Horstmann**, **Petra Wolfrath**, **Christin Kleest** and **Alexander Masurowski** for their support over the years. I felt very welcome and really enjoyed being part of the work group.

Finally, i am particularly thankful for my **family and friends**, their unconditional love, friendship and support at any time.

Contents

List of Figures

List of Tables

1

Introduction

1.1 Structure of the thesis and manuscript contributions

This cumulative PhD thesis consists of five chapters of which this first one is a general introduction to the topic. Chapters two, three and four are scientific manuscripts that are either already published or submitted to peer reviewed journals. The fifth and last chapter is a general conclusion, summing up the results of the manuscripts and giving an outlook for further research. The following tables are meant to clarify the contribution of all authors to the scientific manuscripts that build up the main body of this thesis.

Table 1.1: Author contributions to Study I

Author	Research idea	Experiments	Analytics	Interpretation	Writing
Maximilian Schanofski	0 %	50 %	60 %	50 %	70 %
Sara Fanara	80 %	0 %	0 %	25 %	20 %
Burkhard C. Schmidt	20 %	0 %	0 %	25 %	10 %

Study I: Schanofski M, Fanara S, Schmidt BC (2019) CO_2-H_2O solubility in K-rich phonolitic and leucititic melts. Contributions to Mineralogy and Petrology. 174:52. https://doi.org/10.1007/s00410-019-1581-7

It has to be stated at this point, that for the first study of this PhD project, a large part of the Experiments (∼50 %) and Analytics (∼40 %) were part of my master's thesis. The experiments and analytical data derived from my master's thesis were

reconsolidated and due to changes in extinction coefficients the volatile contents for all samples are different to those presented in the master's thesis.

Table 1.2: Author contributions to Study II

Author	Research idea	Experiments	Analytics	Interpretation	Writing
Maximilian Schanofski	50 %	100 %	100 %	80 %	90 %
Dr. Sara Fanara	50 %	0 %	0 %	5 %	0 %
Dr. Burkhard C. Schmidt	0 %	0 %	0 %	15 %	10 %

Study II: Schanofski M, Fanara S; Schmidt BC (2021) Bubble nucleation and growth in H_2O-CO_2 bearing, leucititic melts from decompression experiments. Under review in Contributions to Mineralogy and Petrology

Table 1.3: Author contributions to Study III

Author	Research idea	Experiments	Analytics	Interpretation	Writing
Maximilian Schanofski	70 %	80 %	80 %	80 %	80 %
Dr. Burkhard C. Schmidt	30 %	20 %	20 %	20 %	20 %

Study III: Schanofski M, Schmidt BC (2021) CO_2 quantification in silicate glasses using µ-ATR FTIR spectroscopy. To be submitted to American Mineralogist

1.2 The importance of CO_2 and H_2O in volcanic systems

Earth's carbon undergoes constant cycling and recycling on the basis of the long-term carbon cycle. Rocks store roughly 1000 times the amount of carbon compared to the oceans, the atmosphere, the biosphere and soil combined (Berner 1994). Changes in the long-term carbon cycle have most likely resulted in dramatic increases in the atmospheric CO_2 to more than 10 times the present amount, resulting in significant global warming (Crowley 2001). Volatile degassing from silicate melts plays a fundamental role in transporting carbon from the Earth's interior into the atmosphere. Besides H_2O, CO_2 is the second most abundant volatile in volcanic systems with a solubility in silicate melts roughly an order of magnitude lower (Holloway 1981).

The amount and species of volatiles dissolved in volcanic melts have a large effect on the melts physical properties that influence the intensity and style of volcanic erup-

tions. Several wt% of H_2O can be dissolved at temperatures and pressures typical for magma storage conditions. As a consequence of the dissolution of H_2O in melt, the melt viscosity decreases by orders of magnitude (Shaw 1963) and the liquidus temperature decreases significantly (e.g., Yoder & Tilley 1962). The solubility of H_2O hardly depends on temperature and melt composition but shows a strong positive correlation with pressure (e.g., Holtz et al. 1995).

During ascent and the corresponding decompression of hydrous volcanic melts, a volatile supersaturation builds up. As soon as this supersaturation is large enough to overcome the energy barrier to create new interfaces that is governed by surface tension, H_2O vesicles nucleate according to the classical nucleation theory. Subsequently, H_2O can diffuse into the previously formed bubbles to further lower the volatile supersaturation in the melt. Due to H_2O degassing, the magma density decreases, resulting in an increased buoyancy and an acceleration of magma ascent. This positive feedback effect of decompression, H_2O exsolution and density reduction is one of the main driving forces for explosive volcanic eruptions (e.g., Eichelberger et al. 1986, Woods & Koyaguchi 1994, Alidibirov & Dingwell 1996, Gonnermann & Manga 2007).

Even though CO_2 as the second most abundant volatile in volcanic systems is less soluble than H_2O by an order of magnitude, it might play an important role in the degassing mechanisms during a magma decompression. CO_2 might trigger bubble nucleation prior to the onset of H_2O degassing (Blundy et al. 2010). This can cause preexisting CO_2 bubbles that might facilitate the degassing of H_2O.

Volcanic precursor activity such as seismicity or gas flux measurements are to this point not able to forecast the style of an upcoming eruption in terms of explosivity. Métrich et al. (2010) stated that for example at Stromboli, the low-intensity activity of the open vent system is occasionally disrupted by high-intensity explosions that cannot be explained by precursor measurements and are possibly due to changes deep inside the plumbing system.

The Pozzolane Rosse Eruption (PR) of the Colli Albani Volcanic District 456 ka ago is a good example for an eruption with strikingly high explosivity in relation to its

composition. The magma chamber feeding this eruption is sitting in thick carbonate substrata that act as an unlimited source for CO_2 (Gaeta et al. 2006). This eruption, thus, provides a perfect case study to investigate the eruption dynamics of CO_2-rich melts. For obvious reasons, important processes occurring during magma storage and in volcanic conduits towards the Earth's surface cannot be studied in the field. Research on this field must be conducted on the basis of laboratory experiments in order to simulate the temperature and pressure conditions typical for magmatic systems. In order to interpret silicate melt degassing in terms of bubble nucleation and growth, a profound knowledge of the CO_2 solubility in dry and H_2O-bearing systems is required. On the basis of this, vesiculation processes can be interpreted and further studied.

There are several empirical models based on experimental results to predict the solubility of H_2O-CO_2 fluids in silicate melts (Dixon 1997, Papale 1999, Ghiorso & Gualda 2015). For a less common composition such as the PR, however, they fail to predict in particular the CO_2 solubility accurately. Thus, there is need to investigate the volatile solubility in this particular melt composition. The same holds for the understanding of CO_2 degassing from silicate melts. Numerous experimental studies investigated the decompression induced vesiculation of H_2O bearing silicate melts (e.g., Hurwitz & Navon 1994, Iacono Marziano et al. 2007, Allabar & Nowak 2018). However, only very few experimental studies exist that take CO_2 as the second most abundant volatile into account (Mourtada-Bonnefoi & Laporte 2002, Gardner & Webster 2016, Pichavant et al. 2013). Recently, Le Gall & Pichavant (2016a,b) performed step-decompression experiments on basaltic melts with decompression rates of 0.04 and 0.08 MPa/s. Buono et al. (2020) performed continuous decompression experiments on a K-trachytic melt. Their results show that bubble formation in evolved alkaline melts is primarily controlled by the initial H_2O-CO_2 volatile content at magma storage conditions. Additionally, an increased vesicle number density and continuous vesicle nucleation was found for CO_2-rich melts ($X^{fl}_{CO2} \geq 0.5$) at high decompression rates. These conditions typically lead to highly explosive eruptions.

This PhD thesis project aimed at identifying the role of CO_2 in the explosive Pozzolane Rosse eruption on the basis of high P high T experiments. As a first step, the CO_2-H_2O solubility (**study I**) of synthetic melt analogues to the Pozzolane Rosse eruption

as well as the Vesuvius 79 AD eruption are studied to close the data-gap that remains for the uncommon melt composition of the PR eruption. The Vesuvius composition was chosen to complement the PR composition since together these compositions represent the alkali-rich endmembers of Italian volcanism (Freda et al. 2008). Study I provides the basis for understanding the melt degassing during magma ascent followed in the next study. The second study focusses on degassing mechanisms (**study II**) of different H_2O-CO_2 volatile mixtures on a synthetic analogue to the material erupted during the Pozzolane Rosse eruption. Here we aim at new insights on the effect of CO_2 on the degassing of H_2O

The third study (**study III**) tackles a general analytical problem that arose during the aforementioned studies. CO_2 is bound as CO_3^{2-} exclusively in the SULm composition. The conventional transmission FTIR analysis is a great technique for measuring low CO_3^{2-} concentrations. With increasing CO_3^{2-} content however, detector saturation of the carbonate doublet is easily reached, making a quantification of the signal impossible. Since the absorbance in these measurements is dependent on the sample thickness, samples can be polished very thin to enable quantification of high CO_3^{2-} concentrations. Samples containing 5000 ppm and more CO_2 require sample thicknesses well below 100 µm making sample preparation and handling more and more difficult. A novel application of µATR FTIR spectroscopy was developed to account for this problem. It is independent of sample thickness and gives an analyzable CO_3^{2-} signal for CO_2 concentrations from as low as 0.17 wt% up to several wt%.

1.3 Geological setting

The central Italian volcanism forms a narrow NW - SE oriented chain of volcanoes following the Thyrrhenian Sea margin from Tuscany down to the Campanian volcanic district. The Colli Albani south of Rome and the Mt. Somma Vesuvius close to Naples are part of this volcano chain. It developed during the Quaternary as a result of two superimposing stress fields. A NE - SW extensional movement (Serri et al. 1993, Peccerillo 2005) and a N - S compression (Faccenna et al. 1994). These competing stress fields create the alternating transpressive and extensional tectonics in the area (Marra 1999). The Colli Albani is rooted in an 4 - 6 km thick carbonate succession (Chiarabba

et al. 1997, Bianchi et al. 2008). Volcanic activity of the Colli Albani shows a broad spectrum of eruptive styles and is divided in three main periods of activity (e.g., De Rita et al. 1995). The oldest phase is the Tuscolano-Artemisio (0.56 – 0.35 Ma) and was characterized by large explosive eruptions such as the Pozzolane Rosse eruption 456 ka ago. The younger eruptive phases Faete (0.31 – 0.25 Ma) and the Hydromagmatic phase (0.20. – 0.04 Ma) showed less explosive activity.

The magma chamber beneath Somma-Vesuvius is much younger (e.g., Brocchini et al. 2001), still active and is also sitting in thick carbonate substrata. The eruptive history of the volcano is characterized by long periods of rest that were interrupted by mildly over highly explosive to Plinian eruptions (e.g., Lirer et al. 2001) of which the 79 AD eruption that destroyed Pompeii, Herculaneum and Stabiae was the most famous.

References

Alidibirov, M. & Dingwell, D. B. (1996). Magma fragmentation by rapid decompression. *Nature*, 380(6570), 146–148.

Allabar, A. & Nowak, M. (2018). Message in a bottle: Spontaneous phase separation of hydrous Vesuvius melt even at low decompression rates. *Earth and Planetary Science Letters*, 501, 192–201.

Berner, R. A. (1994). GEOCARB II; a revised model of atmospheric CO_2 over Phanerozoic time. *American Journal of Science*, 294(1), 56–91.

Bianchi, I., Piana Agostinetti, N., De Gori, P., & Chiarabba, C. (2008). Deep structure of the Colli Albani volcanic district (central Italy) from receiver functions analysis. *Journal of Geophysical Research*, 113(B9), B09313.

Blundy, J., Cashman, K. V., Rust, A., & Witham, F. (2010). A case for CO_2-rich arc magmas. *Earth and Planetary Science Letters*, 290(3-4), 289–301.

Brocchini, D., Principe, C., Castradori, D., Laurenzi, M. A., & Gorla, L. (2001). Quaternary evolution of the southern sector of the Campanian Plain and early Somma-Vesuvius activity: insights from the Trecase 1 well. *Mineralogy and Petrology*, 73(1-3), 67–91.

Buono, G., Fanara, S., Macedonio, G., Palladino, D., Petrosino, P., Sottili, G., & Pappalardo, L. (2020). Dynamics of degassing in evolved alkaline magmas: Petrological, experimental and theoretical insights. *Earth Science Reviews*, 211, 103402.

Chiarabba, C., Amato, A., & Delaney, P. T. (1997). Crustal structure, evolution, and volcanic unrest of the Alban Hills, Central Italy. *Bulletin of Volcanology*, 59(3), 161–170.

Crowley, T. J. (2001). PALEOCLIMATE: Enhanced: CO_2 and Climate Change. *Science*, 292(5518), 870–872.

De Rita, D., Faccenna, C., Funiciello, R., & Rosa, C. (1995). Stratigraphy. In *The Volcano of the Alban Hills* (pp. 33–73). Tipografia SGS.

Dixon, J. E. (1997). Degassing of alkalic basalts. *American Mineralogist*, 82(3-4), 368–378.

Eichelberger, J. C., Carrigan, C. R., Westrich, H. R., & Price, R. H. (1986). Non-explosive silicic volcanism. *Nature*, 323(6089), 598–602.

Faccenna, C., Funiciello, R., & Mattei, M. (1994). Late Pleistocene N-S shear zones along the Latium Thyrrhenian margin : structural characters and volcanological implications. *Global and Planetary Change*, 36(141-44), 507–522.

Freda, C., Gaeta, M., Misiti, V., Mollo, S., Dolfi, D., & Scarlato, P. (2008). Magma–carbonate interaction: An experimental study on ultrapotassic rocks from Alban Hills (Central Italy). *Lithos*, 101(3-4), 397–415.

Gaeta, M., Freda, C., Christensen, J. N., Dallai, L., Marra, F., Karner, D. B., & Scarlato, P. (2006). Time-dependent geochemistry of clinopyroxene from the Alban Hills (Central Italy): Clues to the source and evolution of ultrapotassic magmas. *Lithos*, 86(3-4), 330–346.

Gardner, J. E. & Webster, J. D. (2016). The impact of dissolved CO_2 on bubble nucleation in water-poor rhyolite melts. *Chemical Geology*, 420, 180–185.

REFERENCES

Ghiorso, M. S. & Gualda, G. A. R. (2015). An H_2O–CO_2 mixed fluid saturation model compatible with rhyolite-MELTS. *Contributions to Mineralogy and Petrology*, 169(6), 53.

Gonnermann, H. M. & Manga, M. (2007). The Fluid Mechanics Inside a Volcano. *Annual Review of Fluid Mechanics*, 39(1), 321–356.

Holloway, J. R. (1981). Compositions and volumes of supercritical fluids in the earth's crust. In *Short course in fluid inclusions: Applications to petrology* (pp. 13–38). Mineral Assoc Canada Short Course Handb.

Holtz, F., Dingwell, D. B., & Johannes, W. (1995). H_2O solubility in haplogranitic melts: Compositional, pressure, and temperature dependence. *American Mineralogist*, 80, 94–108.

Hurwitz, S. & Navon, O. (1994). Bubble nucleation in rhyolitic melts: Experiments at high pressure, temperature, and water content. *Earth and Planetary Science Letters*, 122(3-4), 267–280.

Iacono Marziano, G., Schmidt, B. C., & Dolfi, D. (2007). Equilibrium and disequilibrium degassing of a phonolitic melt (Vesuvius AD 79 "white pumice") simulated by decompression experiments. *Journal of Volcanology and Geothermal Research*, 161(3), 151–164.

Le Gall, N. & Pichavant, M. (2016a). Experimental simulation of bubble nucleation and magma ascent in basaltic systems: Implications for Stromboli volcano. *American Mineralogist*, 101(9), 1967–1985.

Le Gall, N. & Pichavant, M. (2016b). Homogeneous bubble nucleation in H_2O- and H_2O-CO_2 -bearing basaltic melts: Results of high temperature decompression experiments. *Journal of Volcanology and Geothermal Research*, 327, 604–621.

Lirer, L., Petrosino, P., Alberico, I., & Postiglione, I. (2001). Long-term volcanic hazard forecasts based on Somma-Vesuvio past eruptive activity. *Bulletin of Volcanology*, 63(1), 45–60.

Marra, F. (1999). Low-magnitude earthquakes in Rome: structural interpretation and implications for the local stress field. *Geophysical Journal International*, 138(1), 231–243.

Mourtada-Bonnefoi, C. C. & Laporte, D. (2002). Homogeneous bubble nucleation in rhyolitic magmas: An experimental study of the effect of H_2O and CO_2: HOMOGENEOUS BUBBLE NUCLEATION. *Journal of Geophysical Research: Solid Earth*, 107(B4), ECV 2–1–ECV 2–19.

Métrich, N., Bertagnini, A., & Di Muro, A. (2010). Conditions of Magma Storage, Degassing and Ascent at Stromboli: New Insights into the Volcano Plumbing System with Inferences on the Eruptive Dynamics. *Journal of Petrology*, 51(3), 603–626.

Papale, P. (1999). Modeling of the solubility of a two-component H_2O+CO_2 fluid in silicate liquids. *American Mineralogist*, 84, 477–492.

Peccerillo, A. (2005). *Plio-Quaternary Volcanism in Italy: Petrology, Geochemistry, Geodynamics*. Springer.

Pichavant, M., Di Carlo, I., Rotolo, S. G., Scaillet, B., Burgisser, A., Le Gall, N., & Martel, C. (2013). Generation of CO_2-rich melts during basalt magma ascent and degassing. *Contributions to Mineralogy and Petrology*, 166(2), 545–561.

Serri, G., Innocenti, F., & Manetti, P. (1993). Geochemical and petrological evidence of the subduction of delaminated Adriatic continental lithosphere in the genesis of the Neogene-Quaternary magmatism of central Italy. *Tectonophysics*, 223(1-2), 117–147.

Shaw, H. R. (1963). Obsidian-H_2O viscosities at 1000 and 2000 bars in the temperature range 700 ° to 900 °C. *Journal of Geophysical Research*, 68(23), 6337–6343.

Woods, A. W. & Koyaguchi, T. (1994). Transitions between explosive and effusive eruptions of silicic magmas. *Nature*, 370(6491), 641–644.

Yoder, H. S. & Tilley, C. E. (1962). Origin of Basalt Magmas: An Experimental Study of Natural and Synthetic Rock Systems. *Journal of Petrology*, 3(3), 342–532.

2

CO_2–H_2O solubility in K-rich phonolitic and leucititic melts

Maximilian Schanofski[1], Sara Fanara[1], Burkhard C. Schmidt[1]

[1]Geowissenschaftliches Zentrum, Georg-August-Universität (GZG),
Goldschmidtstraße 1, 37077 Göttingen, Germany

2.1 Abstract

The solubility of CO_2 and H_2O in phonolitic and leucititic melts from Vesuvius and Colli Albani was investigated experimentally at 1250 °C and pressures between 50 and 300 MPa as a function of CO_2–H_2O fluid composition. Quenched glasses were analyzed for their volatile contents by thermogravimetry, carbon–sulfur analysis, and Fourier transform infrared (FTIR) spectroscopy, which enabled the determination of the absorption coefficients of the H_2O- and CO_2-related IR bands at 5200 cm^{-1} (H_2O molecules), 4500 cm^{-1} (OH groups), and the carbonate doublet at 1510 and 1430 cm^{-1}. No molecular CO_2 was detected in our phonolitic and leucititic glasses. Leucititic glasses with elevated CO_2 concentrations (approaching total absorption in transmission FTIR measurements) were also analyzed quantitatively by micro-ATR (attenuated total refection) IR spectroscopy. While the water solubility in both melts is quite similar for pure H_2O as well as for mixed CO_2–H_2O fluids (at given f_{H_2O}), the CO_2 solubility depends strongly on melt composition. In the range of 100 – 300 MPa, the solubility of

pure CO_2 increases from 580 to 1800 ppm in the phonolite melt and from 2950 to 8460 ppm in the leucitite melt. For the leucitite melt, we observe a single power law trend of CO_2 solubility as function of f_{CO_2}, regardless if the melt was equilibrated with pure CO_2 or mixed CO_2–H_2O fluids, indicating that water acts as diluent of the fluid phase. However, for the phonolite melt, we observe for mixed CO_2–H_2O samples a positive solubility deviation from the power law trend defined by the data for pure CO_2 solubility. This effect seems to increase with increasing water content and pressure. Our interpretation is that this enhanced CO_2 solubility is caused by melt depolymerization induced by water and is more apparent in the relatively polymerized phonolitic melt compared to the relatively depolymerized leucititic melt.

Keywords: H_2O-CO_2 solubility · Phonolite · Leucitite · FTIR-ATR · Mt. Somma-Vesuvius · Colli Albani · High-K silicate melts · Fugacity

2.2 Introduction

Some of the most dangerous active volcanoes in the world are characterized by elevated CO_2 contents, that result from magmatic plumbing systems being emplaced within thick carbonate substrata or from CO_2 flushing directly from the mantle or from the subducting slab: e.g., the Colli Albani volcanic district, Italy (Gaeta et al. 2006), Mt Somma–Vesuvius, Italy (Bruno et al. 1998), the Campi Flegrei volcanic district, Italy (D'Antonio 2011), Mt Etna, Italy (Lentini 1982), Popocatépetl volcano, Mexico (Goff et al. 2015), the Colima volcanic complex, Mexico (Norini et al. 2010), and Merapi, Indonesia (Troll et al. 2012). In most of the above mentioned areas, a significant amount of CO_2 is produced from magma–carbonate interaction during contact metamorphic reactions (i.e., carbonate break-down and assimilation) with significant effects on eruptive intensities and dynamics (Deegan et al. 2010, Freda et al. 1997, Goff et al. 2015, Jeffrey et al. 2013, Jolis et al. 2015). More recently, Caricchi et al. (2018) showed how CO_2 flushing, a widespread process in magma storage in the upper crust, may affect chemical and physical evolution processes of diverse magma compositions using rhyolite-MELTS. Therefore, even if H_2O is recognized as the most important volatile species present in magmas and as the main driving force of volcanic eruptions through magma vesiculation and expansion (Burnham 1979), the less soluble CO_2 component

may also contribute to bubble nucleation and growth, in particular at depth, where water is still soluble in the melts. In this perspective, the detailed knowledge of the solubility of H_2O and CO_2 in magma suites typical of volcanic systems emplaced in carbonate-rich crust such as peralkaline, K-rich, and ultrapotassic suites is fundamental to shed light on the onset of magma degassing and improving the forecasting of hazardous events related to explosive volcanism.

In the last decades, experimental studies on H_2O–CO_2 solubility were mostly performed at constant pressure, temperature, and melt composition but varying the CO_2/H_2O ratios. A recent, detailed review on H_2O–CO_2 solubility is presented by (Ni & Keppler 2013).

Focusing our attention on characteristic compositions of melts emplaced in carbonate substrata and on pressures relevant for magma storage conditions in the upper crust (up to 500 MPa), it was demonstrated by previous studies that water solubility as function of pressure shows little variations over a wide range of compositions, with alkali-rich melts being able to dissolve about 10 % relative more water than MORB melts (Behrens et al. 2009, Fanara et al. 2015, Lesne et al. 2011a,b, Schmidt & Behrens 2008, Vetere et al. 2014).

CO_2 solubility is shown to be enhanced by the presence of alkalis in a more dramatic way than water. In particular, the effect of alkalis on the solubility of H_2O and CO_2 in phonotephritic melts from Colli Albani was investigated at 500 MPa and 1250 °C in systems with fluid $H_2O/(H_2O + CO_2)$ ratios varying from 0 to 1 by Vetere et al. (2014). The highest CO_2 content (1.18 wt%) was found in Na-rich melts, suggesting that Na could promote carbonate incorporation stronger than K (Vetere et al. 2014). Recently, Fanara et al. (2015) investigated experimentally the solubility of H_2O- and CO_2-bearing fluids in trachytic and trachybasaltic melts from the Phlegrean Fields Volcanic District at 1100 and 1200 °C, respectively, and at 100 – 500 MPa, showing that the content of dissolved CO_2 in melts at 300 MPa varies from 1100 ppm in trachyte to 1800 ppm in trachybasalt. If we consider a wider range of compositions, the CO_2 solubility for a MORB will approach 1500 ppm at 300 MPa (Shishkina et al. 2010) and the one of a kimberlite will reach approximately 3 wt% at the same pressure conditions

(Moussallam et al. 2016). For melts in equilibrium with mixed H_2O–CO_2 fluids with varying fraction of H_2O ($X^{fl}_{H_2O}$), most studies reported a negative correlation between the solubility of CO_2 and H_2O under isobaric conditions.

Currently, H_2O–CO_2 solubility data are still missing for the end-member compositions of the high potassium suite of the volcanic districts in central Italy. To improve on this, we have conducted experiments on a K-rich, phonolitic melt from the 79 AD eruption of the Vesuvius and on an ultrapotassic, leucititic melt from the Pozzolane Rosse eruption of Colli Albani Volcanoes. The H_2O–CO_2 solubility experiments were performed at 1250 °C and pressures up to 300 MPa for up to 4 days in an IHPV at intrinsic oxygen fugacity conditions (f_{O_2}= NNO + 3 ± 1). Concentrations of volatiles in quenched glasses were measured by thermogravimetry (TGA), carbon–sulfur analyzer (CSA), and Fourier transform infrared (FTIR) spectroscopy. The experimental data will be useful to estimate the volatile content and the composition of the fluid phases coexisting with the investigated magmas at depth (i.e., in comparison with data obtained from melt inclusions). Furthermore, this study may provide key data to work out the volatile budget at the studied volcanoes, which is a fundamental knowledge to interpret and model degassing processes during magma ascent.

2.3 Experimental and analytical methods

2.3.1 Synthetic starting materials and capsule preparation for solubility experiments

The starting materials were a synthetic, phonolitic glass with a composition close to the "Vesuvius 79 AD white pumice" (Iacono-Marziano et al. 2007) of M. Somma–Vesuvius stratovolcano and a synthetic, leucititic glass with a composition close to the ultrapotassic leucitite "SULm" of the Pozzolane Rosse eruption from Colli Albani (Freda et al. 2011). These two compositions can be considered as magma-type endmembers of the whole high-K suite of central Italy and are therefore fundamental to understand magmatic evolution in this volcanic area. The phonolitic and leucititic glasses were synthesized by melting mixtures of oxides and carbonates in a Pt crucible at 1600 °C and ambient pressure for 1 h. The obtained melts were rapidly quenched by submerging the bottom of the crucible in water. The glasses were crushed, grounded, and re-melted

twice at the same conditions for 4 h to improve their homogeneity. The obtained glass batches were relaxed at 700 °C in a 1 atm oven for 30 min and finally left in air to cool down to room temperature. For both compositions, glasses free of crystals and bubbles were obtained. The compositions and homogeneity of the glasses were verified by a Bruker M4 Tornado micro-X-ray fluorescence (µ-XRF) spectrometer using polished glass pieces and are reported in Table 2.1.

Table 2.1: Phonolitic and leucititic melt composition measured by micro-XRF analysis

	VES79-SM	SULm-SM	[a]SULm	[b]VES79AD
SiO_2	55.82 (15)	44.45 (14)	44.52	57.15
TiO_2	0.31 (1)	0.97 (1)	0.95	0.30
Al_2O_3	21.75 (11)	16.29 (6)	16.17	21.34
[c]Fe_2O_3	2.91 (3)	10.82 (6)	10.56	3.00
MnO	0.15 (1)	0.26 (1)	0.23	0.14
MgO	0.43 (6)	4.14 (7)	3.93	0.39
CaO	3.19 (3)	10.97 (5)	10.78	3.26
Na_2O	5.45 (22)	2.86 (24)	3.02	5.16
K_2O	9.90 (4)	9.18 (3)	8.63	9.46
[d]Ce_2O_3	0.09 (0)	0.06 (0)		
total	100	100	98.79	100.2

Micro-XRF analyses are based on 20 measurements on 1 fragment of each glass. The initial concentrations obtained by the standardless µ-XRF analysis were corrected using a set of 50 natural and synthetic aluminosilicate glasses with known compositions. All values show content in wt% . [a]From Freda et al. (2011). [b]From Iacono-Marziano et al. (2007). 2σ (last decimals) is given in parentheses. [c]All iron is given as Fe_2O_3. [d]Ce_2O_3 is present in both starting materials as contamination of used SiO_2

$Au_{75}Pd_{25}$ capsules (4 mm diameter, 0.2 mm wall thickness, and 25 mm length) were used to conduct the solubility experiments. In case of the phonolitic melt, 5 mm-long cylinders were cored out of the starting glass. Since the leucititic glass was too brittle for coring, glass spheres were made from the starting material by remelting small pieces of glass in an acetylene–oxygen flame. The aim of using solid-glass blocks for the solubility experiments was to obtain bubble-free portions in the samples, suitable for FTIR transmission spectroscopy. A first layer of glass powder was compacted on the bottom of each capsule followed by a glass cylinder or 3 – 4 glass spheres. More glass powder was added until the capsule contained about 200 mg of sample. Finally, deionized water and $Ag_2C_2O_4$ were added as sources for H_2O and CO_2. The $Ag_2C_2O_4$

was prepared by dissolving 1 g of oxalic acid in 20 ml of deionized water. One gram of silver nitrate was then added to the oxalic acid solution, leading to the precipitation of the insoluble $Ag_2C_2O_4$ as a white mass. The obtained silver oxalate was then filtered and dried, and leftover reactants were washed away with absolute ethanol.

Water and silver oxalate were loaded into the capsules in different proportions to obtain a final $X_{H_2O}^{fl}$ of approximately 1, 0.8, 0.6, 0.4, 0.2, and 0 in the fluid phase. The necessary amounts were calculated by adding a total amount of 15 mg of volatiles to the estimated dissolved amounts in glass at equilibrium (Tables 2.2, 2.3). The weight of the capsules was determined before and after welding to check for volatile loss. Subsequently, the capsules were heated to 350 °C for 15 min at 100 MPa in a hydrothermal autoclave to dissociate the silver oxalate, achieving a homogeneous dispersal of CO_2 and simultaneously checking them for leakage.

2.3.2 Solubility experiments

Solubility experiments were run in an internally heated pressure vessel (IHPV) pressurized with Ar at 100, 200, and 300 MPa and at 1250 °C for 44 – 107 h at intrinsic oxygen fugacity conditions (f_{O_2}= NNO + 3 ± 1), and are listed in Tables 2.2, 2.3. The IHPV operates vertically and has a rapid quench device similar to that of Roux & Lefèvre (1992). Up to six capsules with different $X_{H_2O}^{fl}$ between 0 and 1 were placed in two platinum cups that were suspended from a quench wire ($Pt_{95}Rh_5$, 0.2 mm diameter) connected to two electrodes. During the experiment, the suspended samples were located in the hot spot zone of the furnace, where the thermal gradient could be minimized to less than 15 °C by controlling the energy supply of the two platinum windings of the furnace. Temperature was recorded by three S-type thermocouples and pressure was recorded by a transducer, calibrated against a Heise tube gauge (considered to be accurate to ± 5 MPa). At the end of the experiment, the quench electrodes were connected to an adjustable power supply and the voltage was rapidly raised, which led to electrical fusion of the quench wire, thus dropping the samples into the cold bottom part of the vessel (T < 50 °C). The cooling rate in similar experiments was determined to be 150 °C s^{-1} by Benne & Behrens (2003). The obtained glasses were mostly bubble-poor and free of crystals. At high pressures and high amounts of dissolved H_2O, up to ∼10 vol.% micro quench crystals were observed in the leucititic glasses.

Table 2.2: Experimental conditions and results of H_2O and CO_2 solubility experiments for phonolite

Sample	P (MPa)	t (h)	[a]H_2O (mg)	[a]CO_2 (mg)	[b]$X^{fl}_{H_2O}$	[c]a(H_2O)	[c]a(CO_2)	[c]f(H_2O) (MPa)	[c]f(CO_2) (MPa)	[d]H_2O(TGA) (wt%)	[d]CO_2(CS) (ppm)	[e]H_2O^m (wt%)	[e]OH (wt%)	[e]H_2O_{tot} (wt%)	[e]CO_2 (ppm)	[f]Notes
VES79_ 0.5_ 1	50	71	0.14	14.76	0.023	0.022	0.977	1.1	54.8		540 (440)	0.00 (0)	0.09 (14)	0.09 (14)	280 (60)	
VES79_ 0.5_ 6	50	72	4.25	0.06	0.994	0.994	0.005	49.6	0.3	2.11 (2)		1.13 (4)	0.94 (6)	2.07 (7)		
VES79_ 1_ 1	100	92	0.16	14.82	0.026	0.025	0.975	2.5	123.1		1130 (270)	0.00 (0)	0.31 (3)	0.31 (3)	520 (30)	
VES79_ 1_ 2	100	92	1.37	13.11	0.204	0.197	0.796	19.8	100.5			0.17 (4)	0.80 (5)	0.97 (7)	450 (30)	
VES79_ 1_ 3	100	92	3.18	10.99	0.414	0.404	0.584	40.5	73.7			0.55 (4)	1.19 (9)	1.74 (10)	410 (40)	
VES79_ 1_ 4	100	92	5.81	8.66	0.621	0.613	0.373	61.5	47.1			0.89 (3)	1.37 (8)	2.26 (9)	350 (70)	
VES79_ 1_ 5	100	92	9.76	2.32	0.911	0.910	0.084	91.3	10.6			1.64 (7)	1.54 (10)	3.18 (12)	220 (10)	
VES79_ 1_ 6	100	92	13.52	0.63	0.981	0.981	0.017	98.4	2.2	3.56 (13)		2.01 (8)	1.61 (10)	3.62 (13)		
VES79_ 1.5_ 1	150	65	0.13	14.86	0.021	0.022	0.979	3.3	209.8		910 (170)	0.00 (0)	0.24 (1)	0.24 (1)	770 (60)	
VES79_ 1.5_ 6	150	65	15.98	0.09	0.998	0.998	0.002	151.7	4.0	4.31 (14)		2.50 (12)	1.75 (14)	4.25 (18)		
VES79_ 2_ 1	200	90	1.08	13.77	0.161	0.171	0.842	35.2	272.9		1140 (340)	0.00 (0)	0.24 (2)	0.24 (2)	1160 (60)	F
VES79_ 2_ 2	200	90	1.81	12.37	0.263	0.274	0.743	56.4	240.9			0.37 (3)	0.96 (6)	1.33 (7)	1010 (80)	F
VES79_ 2_ 3	200	90	3.16	10.62	0.421	0.429	0.590	88.5	191.2			1.25 (6)	1.40 (9)	2.65 (11)	1050 (140)	N
VES79_ 2_ 4	200	90	5.40	8.24	0.615	0.620	0.397	127.7	128.8			1.88 (7)	1.55 (10)	3.43 (12)	900 (50)	
VES79_ 2_ 5	200	90	9.22	4.51	0.833	0.884	0.123	182.2	39.9			2.98 (13)	1.70 (11)	4.68 (17)	600 (80)	
VES79_ 2_ 6	200	107	11.09	1.23	0.957	0.957	0.046	197.3	14.8	5.75 (44)		3.99 (15)	1.88 (12)	5.87 (19)		
VES79_ 2.5_ 1	250	70	0.09	13.12	0.016	0.016	0.984	4.2	418.5		1540 (650)	0.00 (0)	0.23 (8)	0.23 (8)	1430 (100)	
VES79_ 2.5_ 6	250	70	12.01	0.09	0.997	0.997	0.003	254.1	1.4	6.51 (31)		4.61 (18)	1.79 (11)	6.40 (21)		
VES79_ 3_ 1	300	89	1.08	14.28	0.156	0.164	0.845	51.4	491.3		1790 (270)	0.00 (0)	0.39 (3)	0.39 (3)	1790 (90)	F
VES79_ 3_ 2	300	89	2.14	11.96	0.304	0.315	0.699	99.0	406.5			0.64 (3)	1.19 (8)	1.83 (8)	1690 (170)	F
VES79_ 3_ 3	300	89	3.56	10.33	0.457	0.469	0.549	147.2	319.3			1.40 (5)	1.55 (9)	2.95 (11)	1710 (90)	F
VES79_ 3_ 4	300	89	5.67	8.21	0.628	0.637	0.381	200.1	221.6			2.67 (11)	1.78 (12)	4.45 (16)	1510 (160)	F
VES79_ 3_ 5	300	89	9.08	4.11	0.844	0.847	0.165	266.0	95.9			3.88 (14)	1.84 (12)	5.72 (18)	770 (120)	F
VES79_ 3_ 6	300	89	11.39	0.63	0.978	0.978	0.024	307.2	14.0	7.34 (45)		5.56 (20)	1.81 (11)	7.37 (23)		F
VES79_ 3_ 1*	300	90	0.08	14.85	0.013	0.014	0.987	4.3	573.9			0.00 (0)	0.30 (2)	0.30 (2)	1780 (110)	N
VES79_ 3_ 2*	300	90	0.73	13.46	0.117	0.123	0.883	38.6	513.7		1710	0.52 (2)	1.08 (6)	1.60 (6)	1810 (170)	N
VES79_ 3_ 3*	300	90	2.23	11.94	0.313	0.324	0.690	101.9	401.2		1810	1.56 (6)	1.43 (8)	2.99 (10)	1740 (200)	N
VES79_ 3_ 4*	300	90	4.25	9.20	0.530	0.541	0.477	169.9	277.6		1580	2.83 (11)	1.56 (8)	4.39 (14)	1620 (120)	N
VES79_ 3_ 5*	300	90	7.63	5.50	0.772	0.777	0.238	244.1	138.3			4.09 (33)	1.59 (14)	5.68 (36)	1110 (70)	N
VES79_ 3_ 6*	300	90	11.89	0.00	1.000	1.000	0.000	314.1	0.0			5.74 (26)	1.62 (8)	7.36 (27)		N
VES79_ 80	300	90	3.47	2.61	0.765	0.765	0.249	240.4	145.4			3.89 (20)	1.67 (10)	5.56 (22)	1210 (330)	

[a]Uncertainty in the weight of H_2O and CO_2 in the fluid phase can reach 0,00010 g. [b]$X^{fl}_{H_2O}$ refers to the mole fractions of H_2O in the fluid phase present in the capsules after experiments. [c]The activity and fugacity of the volatiles were calculated following the model of Duan (2014). [d]Calculated errors are shown in brackets near values (2σ errors of repeated measurements). [e]Concentration of H_2O and CO_2 determined by FTIR. Errors of volatile contents were calculated by error propagation of density, thickness and absorbance errors. [f]N= normal quench, F= incorrect Fluid determination: data from sample set (*) was used for all relevant calculations and plots. See text for further information

Table 2.3: Experimental conditions and results of H_2O and CO_2 solubility experiments for leucitite

Sample	P (MPa)	t (h)	[a]H_2O (mg)	[a]CO_2 (mg)	[b]$X^{fl}_{H_2O}$	[c]a(H_2O)	[c]a(CO_2)	[c]f(H_2O) (MPa)	[c]f(CO_2) (MPa)	[d]H_2O(TGA) (wt%)	[d]CO_2(CS) (ppm)	[e]H_2O^m (wt%)	[e]OH (wt%)	[e]H_2O_{tot} (wt%)	[e]CO_2 (ppm)	[f]Notes
SULm_ 0.5_ 1	50	71	0.33	15.47	0.050	0.048	0.950	2.4	53.3		1540 (150)	0.00 (0)	0.35 (2)	0.35 (2)	1610 (60)	
SULm_ 0.5_ 6	50	72	3.14	0.03	0.996	0.996	0.004	49.7	0.2	2.57 (14)		0.84 (11)	1.77 (9)	2.61 (14)		
SULm_ 1_ 1	100	72	0.36	15.15	0.055	0.053	0.945	5.3	119.4		3040 (350)	0.00 (0)	0.47 (5)	0.47 (5)	2940 (100)	
SULm_ 1_ 2	100	72	0.87	13.57	0.135	0.131	0.865	13.1	109.3			0.27 (6)	1.09 (6)	1.36 (8)	2660 (90)	
SULm_ 1_ 3	100	72	1.95	11.45	0.294	0.285	0.705	28.6	89.1			0.42 (7)	1.60 (8)	2.02 (10)	2200 (80)	
SULm_ 1_ 4	100	72	4.00	9.01	0.520	0.510	0.476	51.2	60.1			0.80 (8)	1.94 (17)	2.74 (19)	1780 (60)	
SULm_ 1_ 5	100	72	7.28	5.66	0.759	0.754	0.234	75.6	29.5			1.19 (11)	2.29 (11)	3.48 (15)	1330 (50)	
SULm_ 1_ 6	100	72	12.89	0.00	1.000	1.000	0.000	100.3	0.0	3.84 (14)		1.49 (14)	2.26 (11)	3.75 (18)		
SULm_ 1.5_ 1	150	44	0.18	15.01	0.028	0.028	0.972	4.3	208.4		4040 (100)	0.00 (0)	0.36 (2)	0.36 (2)	3850 (140)	
SULm_ 1.5_ 6	150	65	11.45	0.97	0.966	0.966	0.033	146.9	7.1	4.66 (8)		2.56 (26)	2.08 (27)	4.65 (37)		F
SULm_ 2_ 1	200	47	0.13	15.12	0.021	0.023	0.979	4.7	317.4		5440 (250)	0.00 (0)	0.50 (3)	0.50 (3)	5680 (200)	
SULm_ 2_ 2	200	74	1.20	13.18	0.182	0.192	0.822	39.6	266.3			0.32 (6)	1.33 (15)	1.65 (16)	5450 (190)	
SULm_ 2_ 3	200	74	2.15	11.74	0.309	0.319	0.699	65.8	226.5			0.88 (8)	1.99 (10)	2.87 (13)	4650 (160)	
SULm_ 2_ 4	200	74	4.01	9.17	0.516	0.523	0.496	107.7	160.9			1.46 (13)	2.38 (11)	3.84 (17)	3730 (130)	
SULm_ 2_ 5	200	74	7.71	5.72	0.767	0.769	0.240	158.5	77.8			2.45 (24)	2.29 (34)	4.74 (41)	2460 (90)	Q
SULm_ 2_ 6	200	74	12.68	0.00	1.000	1.000	0.000	206.1	0.0	5.72 (9)		3.24 (31)	2.58 (13)	5.82 (33)		Q
SULm_ 2.5_ 1	250	17	0.11	15.31	0.017	0.018	0.983	4.5	418.2		6380 (530)	0.00 (0)	0.37 (12)	0.37 (12)	6320 (220)	
SULm_ 2.5_ 6	250	17	12.29	0.26	0.991	0.991	0.010	252.6	4.1	5.75 (130)		2.80 (27)	2.36 (26)	5.16 (37)		F, N, Q
SULm_ 3_ 1	300	76	0.18	15.23	0.028	0.030	0.972	9.3	565.2		8440 (570)	0.00 (0)	0.65 (3)	0.65 (3)	8460 (300)	
SULm_ 3_ 2	300	76	0.86	13.53	0.134	0.141	0.867	44.2	503.9			0.48 (10)	1.71 (23)	2.19 (25)	7700 (270)	
SULm_ 3_ 3	300	76	2.30	12.11	0.317	0.328	0.686	103.1	399.1			1.27 (12)	2.31 (11)	3.58 (16)	6590 (230)	
SULm_ 3_ 4	300	76	4.57	9.26	0.547	0.558	0.461	175.2	267.9			2.36 (31)	2.40 (24)	4.76 (40)	5740 (200)	Q
SULm_ 3_ 5	300	76	8.05	5.15	0.792	0.797	0.218	250.2	126.7			3.78 (38)	2.51 (24)	6.29 (45)	3700 (130)	Q
SULm_ 3_ 6	300	76	12.94	1.16	0.965	0.965	0.038	303.1	22.2	6.90 (7)		4.51 (42)	2.78 (25)	7.29 (49)		F, Q
SULm_ 0.5	100	75										0.00 (0)	0.71 (3)	0.71 (3)		U
SULm_ 1.0	100	75										0.07 (8)	1.03 (33)	1.10 (34)		U

[a]Uncertainty in the weight of H_2O and CO_2 in the fluid phase can reach 0.1 mg. [b]$X^{fl}_{H_2O}$ refers to the mole fractions of H_2O in the fluid phase present in the capsules after experiments. [c]The activity and fugacity of the volatiles were calculated following the model of Duan (2014). [d]Calculated errors are shown in brackets near values (2σ errors of repeated measurements). [e]Concentration of H_2O and CO_2 determined by FTIR. Errors of volatile contents were calculated by error propagation of density, thickness and absorbance errors. [f]F= water escape during fluid measurement, Q= quench crystallization, N= not equilibrated, U= undersaturated

2.3.3 Determination of fluid composition after experiments

The composition of H_2O–CO_2 fluids in the capsules was determined by a weight-loss method after each experiment. Each capsule was initially weighted on a Cahn C-31 microbalance, and then frozen in liquid nitrogen and pierced with a needle. After piercing, the capsules were emplaced in a nitrogen gas fux at about -20 °C (measured by a K-type thermocouple) for 1 min. At this temperature, the H_2O is still frozen, while CO_2 is able to degas from the capsule with minimal loss of H_2O. In the next step, the capsules were heated to room temperature and weighted again to measure the released CO_2. The capsules were then stored in a drying oven at 75 °C overnight and their weight was measured afterwards yielding the released H_2O. In a later stage of this study, the liquid H_2O was extracted overnight from the capsule in a desiccator at 35 °C. The $X^{fl}_{H_2O}$ in the fluid for all samples determined in this way is reported in Tables 2.2, 2.3. The main source of error for the determination of $X^{fl}_{H_2O}$ and $X^{fl}_{CO_2}$ is related to the cracking of fluid saturated bubbles during the heating step in the drying furnace, leading to an overestimation of the $X^{fl}_{H_2O}$. An additional potential error derives from the piercing procedure. For instance, some frozen water could be pushed out of the capsule by the stream of the released CO_2 and water can condense inside and/or outside the capsule due to the temperature difference between capsule and surrounding atmosphere.

2.3.4 Thermogravimetry and CS analyzer

The determination of dissolved H_2O in the glasses from experiments with nominally $X^{fl}_{H_2O}$= 1 was done by thermogravimetry using a Setaram™ TGA 92. Depending on the expected H_2O content of the sample, 15 - 30 mg of bubble-free glass per measurement were filled into a Pt crucible (4 mm diameter; 10 mm height) and covered with a Pt lid. During the measurement, a graphite tube furnace is heating the crucible, which is suspended from the balance. During a typical measurement, the sample is heated to 1200 °C at a rate of 10 °C min^{-1} and cooled at a rate of 30 °C min^{-1} after a 30 min dwell time, while the mass of the (dehydrating) sample is continuously recorded. Since the buoyancy of the suspended crucible and sample changes with changing temperature, a blank measurement was recorded once per day. Such blank measurement consists

of a second heating and cooling cycle directly after the first one, now with the previously degassed sample. Blank measurements were subtracted from the sample signal to eliminate the effect of buoyancy on crucible and sample. While the measurements for phonolitic samples (2.91 ± 0.03 wt% total Fe_2O_3) were done in air, leucititic samples (10.82 ± 0.06 wt% total Fe_2O_3) were measured in helium to avoid oxidation of Fe^{2+} to Fe^{3+} by reaction with the dissolved water. In this case, H_2 would be released from the sample instead of H_2O, leading to an underestimation of the true water concentrations. More details on the analytical procedure and accuracy of TGA measurements for water determination are given in (Schmidt & Behrens 2008). CO_2 in the glasses with nominally $X^{fl}_{H_2O}$= 0 was determined by CS analyzer (CSA) measurements using a Elementar™ Inductar CS Cube. During a typical measurement, 0.5 g Fe and 2 g W are inserted together with 35 – 50 mg of crushed sample material into a ceramic crucible. The mixture is burned in an induction furnace at roughly 2000 °C in an oxygen stream and the released CO_2 is measured by an IR cell. A typical day of analyses starts with a series of blank measurements without sample (0.5 g Fe + 2 g W only) followed by a series of measurements of steel standards with known CO_2 contents (66 ppm to 1.791 wt%). The blank and the standard measurements are needed to daily calibrate the CSA and correct the analyzed experimental samples accordingly.

2.3.5 Fourier transform infrared spectroscopy

Doubly polished thin sections of experimental glasses were prepared to analyze the H_2O and CO_2 contents using FTIR spectroscopy. The spectra were collected in transmission with an IR microscope (Bruker Hyperion 3000) connected to a FTIR spectrometer (Bruker Vertex 70). The samples were analyzed in the near-infrared (NIR) region (2000 - 6000 cm^{-1}) for water using the 5200 and 4500 cm^{-1} combination bands and in the mid-infrared (MIR) region 600 - 4000 cm^{-1} for CO_2 using the carbonate bands between 1300 and 1600 cm^{-1}. Operation conditions were liquid N_2 cooled MCT detector (range 600 - 12000 cm^{-1}), W lamp and CaF_2 beam splitter for NIR spectra and Globar light source and KBr beam splitter for MIR spectra. Typically, 100 scans were accumulated for each spectrum, with a spectral resolution of 4 cm^{-1} for both, NIR and MIR. To limit the analyzed volume of sample, a square focus area of 50 × 50 µm was defined by the rectangular aperture blades of the IR microscope. MIR-ATR (attenuated total refection) spectra were measured for leucititic glasses, using the ATR objective of the

Hyperion microscope. In this method, a Ge crystal with a truncated, circular tip (100 µm diameter) is pressed with a force of 8 N onto the polished glass surface. The MIR light passes in total refection through the Ge crystal and illuminates the sample on an area of 30 × 30 µm. Here, the IR light interacts with the sample by forming an evanescent wave that penetrates into the sample and gets partially absorbed (see Lowenstern & Pitcher (2013) for more details and application of this method for the determination of water in hydrous glasses). Typically, 32 scans were collected for each sample with a spectral resolution of 4 cm^{-1} in the range from 4000 to 650 cm^{-1}.

The Lambert-Beer law is the basis for a quantitative relationship between water concentration and the absorbance A (baseline-corrected height of the absorption peak):

$$c = \frac{MA}{d\varepsilon\rho}100, \tag{2.1}$$

where M is the molar mass of the component or species, d is the thickness of the sample in cm, ρ is the density in g l^{-1}, ε is the linear molar absorption coefficient in l mol^{-1} cm^{-1}, and c is the weight fraction in wt%. Absorption coefficients for the NIR and MIR bands were calibrated in this study. The thickness of the sections was determined by a Mitutoyo digital micrometer (3 µm accuracy). The thickness of the sections were typically around 500 µm for NIR and 100 µm for MIR measurements with a variation of up to 10 µm. The density of the phonolitic and leucititic glasses was determined using a METTLER TOLEDO Excellence XP/XS balance equipped with a density determination kit. The glasses were weighted in air and in ethanol, and densities were calculated using the equation:

$$C = \frac{A}{(A-B)}(\rho_0 - \rho_L) + \rho_L, \tag{2.2}$$

where A is the weight in air, B is the weight in ethanol, ρ_0 is the density of ethanol, and ρ_L is the density of air (0.0012 g cm^{-3}).

In the case of hydrous, bubble-rich glass pieces or small pieces for which an accurate density determination is not possible, the densities of hydrous glasses with known water contents can be correlated to the thickness normalized peak heights of 4500 cm^{-1} and 5200 cm^{-1} bands of the NIR spectra Schmidt et al. (2013).

2.4 Results

2.4.1 Experimental products and glass compositions

The experimental conditions and the analytical results are reported in Tables 2.2, 2.3. The experimental glasses were mostly crystal- and bubble-free and coexisted with a fluid phase as determined with the weight-loss technique. In water-rich glasses of leucititic composition, some needle shaped crystals and higher amounts of micro-crystals were observed (total amount of crystals up to 10 vol.%). These phases probably formed during quench as a consequence of enhanced crystallization kinetics in H_2O-rich melts. IR spectroscopic data show a homogeneous distribution of H_2O and CO_2 in the glasses, indicating that the run duration was long enough to achieve equilibrium between the fluid phase and the melt. Water was detected in all samples, even in those for which water was not loaded into the capsule. As pointed out in the previous papers (e.g. Behrens et al. 2009, Botcharnikov et al. 2006), this may be related to the reduction of iron in the glasses in the presence of a small amount of hydrogen in the pressure vessel, according to the reaction $Fe_2O_3 + H_2 = 2\ FeO + H_2O$. Another source of water is adsorbed water on the surface of the starting material (glass powders and blocks; silver oxalate).

2.4.2 Infrared spectroscopy

For each phonolitic and leucititic sample, at least three MIR and NIR spectra were collected in different parts of the sample to verify the homogeneity of the volatile distribution in the glasses.

In the NIR spectra, two water-related bands at approximately 4500 and 5200 cm^{-1} are visible for our hydrous glasses (Fig. 2.1). The peak at 4500 cm^{-1} is assigned to structurally bonded hydroxyl groups, while the absorption band at 5200 cm^{-1} is produced by a combination of stretching and bending modes of H_2O molecules (Scholze 1960). Since Moore et al. (1981) observed a significant loss of water in their experimental phonolitic glasses below 200 °C, we collected NIR spectra of the sample VES79_3_6* (7.36 wt% H_2O) before and after storage in a drying furnace at 75 °C over-night to exclude potential loss of water from the samples during the heating step of the fluid determination. NIR spectra showed no significant loss of H_2O. In waterrich, high-pressure

leucititic glasses, an unusual band at 4300 cm^{-1} was found (Fig. 2.1b). This band was also reported in previous studies of water in silicate melts (e.g., Aubaud et al. 2008, Behrens et al. 2009), suggesting that it was due to splitting of the OH band as a result of alteration during quench in iron bearing melts with high water contents. To shed light on the origin of this band, a fairly crystallized glass chip was compared to a crystal poor glass chip of a sample, showing the band at 4300 cm^{-1}. Both glass chips showed an identical intensity of the 4300 cm^{-1} band, suggesting that a micrometric crystal phase can be excluded as the band source. However, the presence of nanoscale crystals or even clusters of molecules may well be the origin of the band.

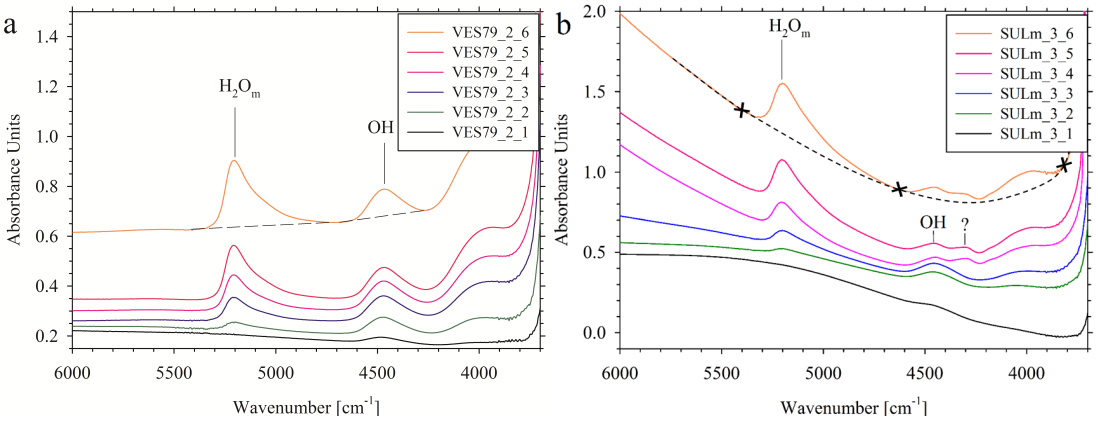

Figure 2.1: **a** NIR absorption spectra of dry and hydrous experimental phonolitic glasses (T= 1250 °C; P= 200 MPa). **b** NIR absorption spectra of dry and hydrous experimental leucititic glasses (T= 1250 °C; P= 300 MPa). Band assignments are: 5200 cm^{-1} combination mode of H_2O molecules; 4500 cm^{-1} combination mode of OH groups; 4300 cm^{-1} still undetermined (see text for further explanation). Dashed lines are the baselines used to calculate peak intensities. Spectra and legends are arranged in identical order

In the MIR region, our spectra show a doublet with maxima at 1430 and 1510 cm^{-1}, which is attributed to carbonate vibrations (Blank & Brooker 1994) (Fig. 2.2). There is no evidence of a peak at approx. 2350 cm^{-1}, which would indicate the presence of molecular CO_2 (as observed for instance in quenched glasses of andesitic, dacitic and rhyolitic composition, (e.g., Behrens et al. 2004, Botcharnikov et al. 2006, Tamic et al. 2001). The carbonate bands were used to quantify the concentrations of CO_2 in the glasses. In the transmission spectra of our phonolitic glasses, the band at 1510 cm^{-1} is partly overlapping with the bending mode of molecular H_2O at 1630 cm^{-1}.

Therefore, we used the peak height of the 1430 cm^{-1} band for CO_2 quantifcation. For the leucititic glasses, we used micro-ATR-FTIR for CO_2 quantification, since samples with high carbonate content, even at thicknesses below 100 µm, reached total absorption in regular transmission spectra. Since the intensities in MIR-ATR spectra are dependent on the contact between ATR-Crystal and the sample, the spectra were normalized to the integral of the 970 cm^{-1} TO-stretching vibration, which represents the tetrahedral units in the aluminosilicate network (Fig. 2.3).

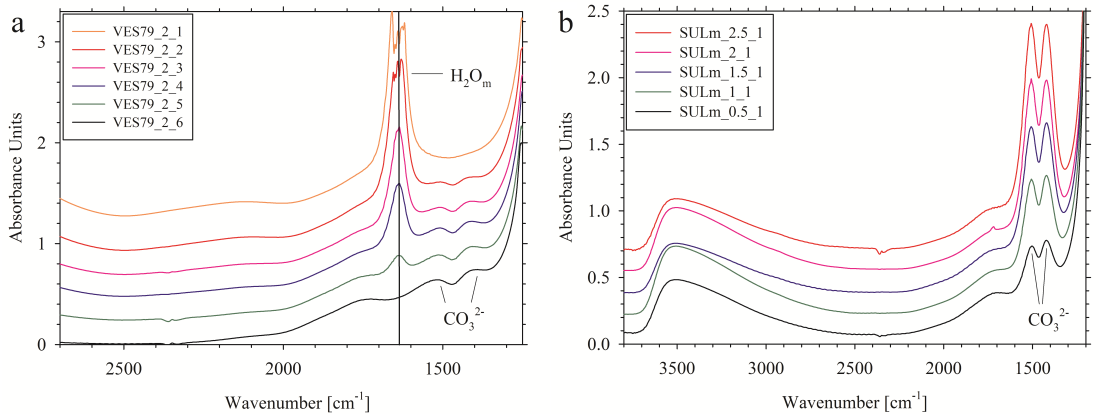

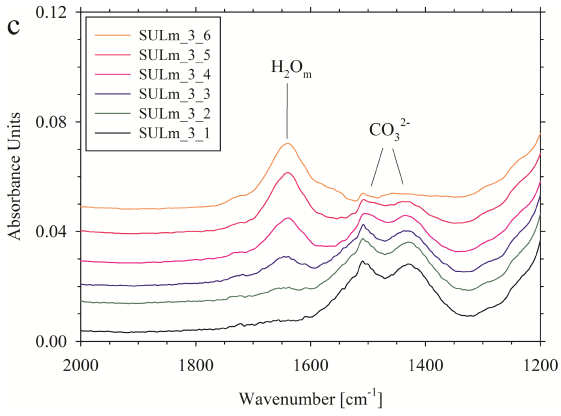

Figure 2.2: **a** MIR absorption spectra of dry and hydrous phonolitic glasses (T= 1250 °C; P= 200 MPa); **b** MIR absorption spectra of dry and hydrous leucititic glasses (T= 1250 °C; P= 50 – 250 MPa);
c MIR-ATR spectra of dry and hydrous leucititic glasses (T= 1250 °C; P= 300 MPa). The positions of 1640 cm^{-1} (H_2O_m), 1510 cm^{-1}, and 1430 cm^{-1} (CO_3^{2-}) bands are indicated. Spectra and legends are arranged in identical order

2.4.3 Baselines

For NIR spectra of the phonolitic composition, two (two-tangent) TT baselines were applied to the 4500 and 5200 cm^{-1} bands to define the peak heights (absorbances) (Fig. 2.1a). In the case of the leucititic spectra, the band at 5200 cm^{-1} was superimposed towards higher wavenumbers by the iron band at 5600 cm^{-1} and the doublet at 4500 - 4300 cm^{-1} was affected towards lower wavenumbers by the 4000 cm^{-1} vibration of

total water. These superimpositions were stronger in more H_2O-rich samples (Fig. 2.1b). Therefore, a polynomial baseline was fitted through three minimum points of the spectra, as shown in Fig. 2.1b. In the MIR range (Fig. 2.3), the phonolite spectra were evaluated by subtracting a CO_3^{2-}-free spectrum of the same composition and lower water content, as shown in Fig. 2.3a. Except for the H_2O^m- and CO_3^{2-}-related bands, the shapes of the two spectra are nearly identical allowing a reliable spectrum subtraction with the difference spectrum only displaying signals from the dissolved volatiles. As the subtracted CO_2-free glass is not H_2O free, the intensity of the H_2O^m bending vibration in the difference spectrum is reduced and can no longer be used to determine the H_2O^m concentration. A TT baseline was applied below the carbonate peak of the subtracted spectra. ATR-MIR spectra of the leucitite were also corrected with a TT baseline (Fig. 2.3b).

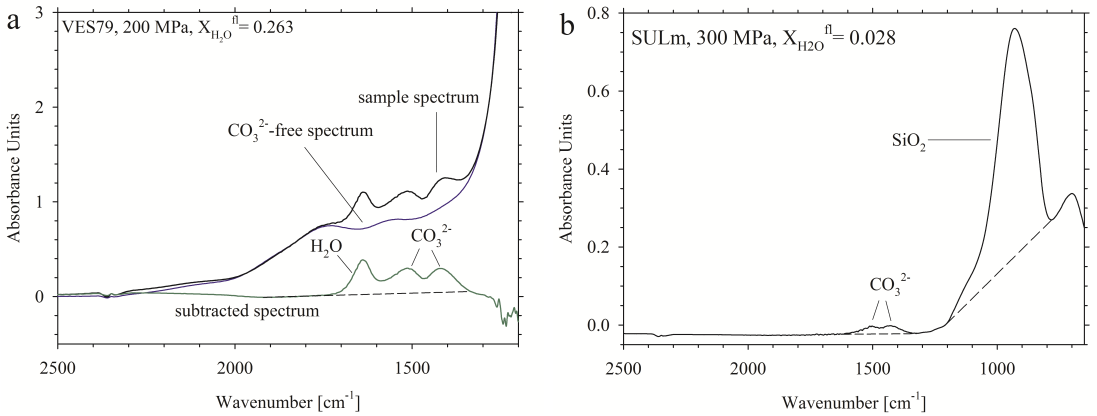

Figure 2.3: **a** MIR absorption spectra of a CO_2-bearing phonolitic glass (VES79_2_2, 1.33 wt% water, 1010 ppm CO_2) and a CO_2-free glass containing about 1 wt% H_2O used for subtraction. Both spectra are scaled to the same thickness. The baseline correction of the difference spectra to calculate peak intensities is a simple straight line connecting the relative minima of the H_2O_m and CO_3^{2-} triplet. **b** MIR-ATR spectrum of CO_2-rich (8460 ppm CO_2, 0.39 wt% H_2O) leucititic glass (T= 1250 °C; P= 300 MPa). Dashed lines are baselines used to calculate the peak intensities

2.4.4 Calibration of the absorption coefficients

In the NIR range, assuming that no other hydrous species are present in the glass besides OH^- and H_2O ($c_{H_2O_t} = c_{H_2O} + c_{OH}$) and that the absorption coefficients ε do

not vary with water content, the ε values can be determined using plots of absorbances normalized by density, thickness and water content (Behrens et al. 1996):

$$c = \left[\frac{1802 * A_{5200}}{d * \rho * c_{H_2O_t}}\right] = \varepsilon_{H_2O} - \frac{\varepsilon_{H_2O}}{\varepsilon_{OH}} * \left[\frac{1802 * A_{4500}}{d * \rho * c_{H_2O_t}}\right]. \quad (2.3)$$

The terms in brackets refer to the normalized absorbances for the peak at 5200 cm^{-1} and 4500 cm^{-1}. The molar absorption coefficients were determined in both compositions by linear regression as the intercepts of the straight line with both axes (Fig. 2.4a); errors are reported as the standard error for the variables in the fit. Molar absorption coefficients are ε_{4500} = 1.00 ± 0.06 l/(mol cm) and ε_{5200} = 1.17 ± 0.04 l/(mol cm) for phonolite and ε_{4500}= 0.42 ± 0.02 l/(mol cm) and ε_{5200}= 1.00 ± 0.09 l/(mol cm) for leucitite and are listed in Table 2.4. As mentioned above, the cH_2O_{tot} in the calibration samples was determined using the TGA, which is unable to separate individual components (i.e. H_2O and CO_2) in the volatile phase. Thus, only samples with nominally $X^{fl}_{H_2O}$= 1 were considered for calibration.

Table 2.4: Molar extinction coefficients for FTIR-Measurements for VES79 and SULm

Composition	ε_{5200} (l/(mol*cm))	ε_{4500} (l/(mol*cm))	ε_{1430} (l/(mol*cm))	ε_{1510} (l/(mol*cm))	k_{1430}
VES79-SM	1.17 (4)	1.00 (6)	245 (17)	220 (20)	-
SULm-SM	1.00 (9)	0.42 (2)	336 (16)	347 (5)	2.38 (6)

k_{1430} is the correlation coefficient for ATR measurements for the CO_2 determination of the leucititic composition. Errors of the calculated coefficients of H_2O are 2σ errors of the intercepts between regression line and coordinate axes. Errors of the calculated coefficients of CO_2 are 2σ errors of the slope of the regressions

Absorption coefficients for the 4500 cm^{-1} and 5200 cm^{-1} bands of the phonolite (ε_{4500}= 1.00 ± 0.06 l/(mol cm) and ε_{5200}= 1.17 ± 0.04 l/(mol cm)) are in good agreement with the previous data from Iacono-Marziano (2004) (ε_{4500}= 0.94 l/(mol cm) and ε_{5200}= 1.21 l/(mol cm)) obtained for the same melt composition with the same background subtraction.

The data presented here are also consistent with the data for Na-rich, peralkaline, and peraluminous phonolitic glasses from Montana Blanca (Tenerife, Spain) (ε_{4500}= 1.12 ±

0.05 l/(mol cm) and ε_{5200}= 1.28 ± 0.02 l/(mol cm)) and the lower Laacher See tephra from Eifel, Germany (ε_{4500}= 0.92 ± 0.09 l/(mol cm) and ε_{5200}= 1.32 ± 0.05 l/(mol cm), Schmidt et al. (2013)) as well as the K-richer upper Laacher See tephra (ε_{4500}= 0.94 ± 0.05 l/(mol cm) and ε_{5200}= 1.18 ± 0.03 l/(mol cm)), (Fanara et al. 2013). Absorption coefficients for the leucitite glass (ε_{4500}= 1.00 ± 0.06 l/(mol cm) and ε_{5200}= 1.17 ± 0.04 l/(mol cm)) are in good agreement with those reported from Behrens et al. (2009) (ε_{4500}= 0.62 ± 0.02 l/(mol cm) and ε_{5200}= 1.02 ± 0.06 l/(mol cm)) on a K-rich phono-tephrite from the Colli Albani volcano.

In the MIR range, the absorbance of the 1430 cm^{-1} band of CO_2-saturated phonolitic and leucititic glass spectra normalized by thickness and density is plotted vs. the bulk content of dissolved carbon analyzed by CS in Fig. 2.4b. Absorption coefficients for the carbonate peak of ε_{1430}= 245 ± 17 l/(mol cm) and ε_{1430}= 336 ± 16 l/(mol cm) were derived for phonolitic and leucititic glasses, respectively. For the leucititic samples showing total absorption for the carbonate bands, a correlation coefficient of 2.38 ± 0.06 was determined for ATR-MIR measurements. Absorption was in this case normalized by the integral of the 970 cm^{-1} SiO_2 band (Int_{970} in Fig. 2.4c). Errors of the coefficients for the carbonate peaks are determined as the standard deviation of the slope of the fits in Fig. 2.4b, c.

The 1430 cm^{-1} absorption coefficient for the VES79 glass(ε_{1430}= 245 ± 17 l/(mol cm)) is consistent with the value determined by Behrens et al. (2009) for a phono-tephritic glass (ε_{1430}= 308 ± 110 l/(mol cm)). Taking into account the relative symmetric shape of the carbonate doublet, the absorption coefficient of the 1430 cm^{-1} band in our leucititic SULm glasses (ε_{1430}= 336 ± 16 l/(mol cm)) is in good agreement with the value of 355 l/(mol cm) obtained for the 1515 cm^{-1} carbonate band for a Ca-rich leucititic glass by Thibault & Holloway (1994).

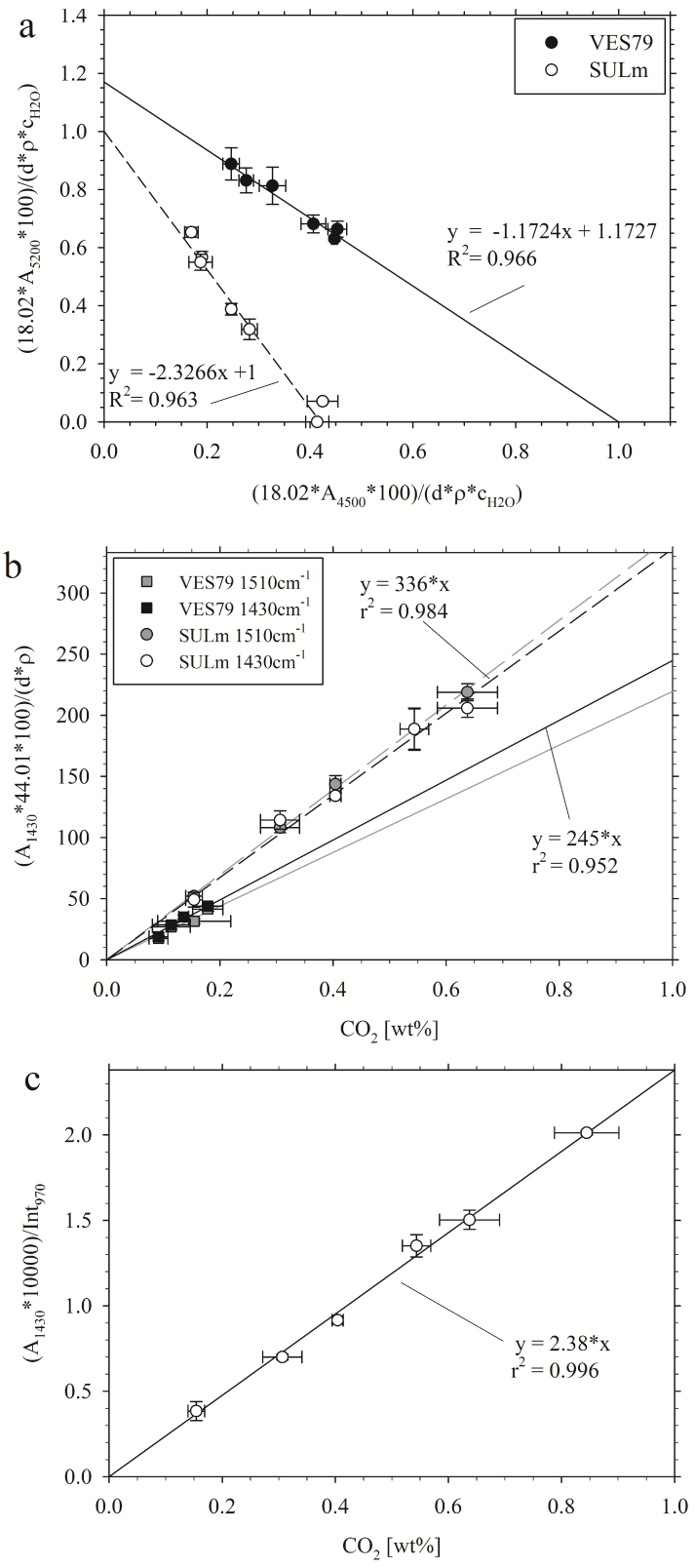

Figure 2.4: **a** Calibration plot for determination of molar absorption coefficients for the OH combination band at 4500 cm^{-1} and H_2O combination band at 5200 cm^{-1}. Solid and dashed lines were obtained by the linear regression of the corresponding data in plot for phonolite and leucitite, respectively. Intercepts of the lines with the axes define the molar absorption coefficients for the 4500 cm^{-1} band (x-axis) and the 5200 cm^{-1} band (y-axis). A TT baseline was used to extract absorbances for phonolite, whereas for leucitite a polynomial baseline was fitted through three minima of the spectra.

b Calibration plot for the determination of the absorption coefficient for the carbonate bands at 1430 cm^{-1} and 1510 cm^{-1}. Normalized absorbances are plotted vs. total carbon content determined by CS analyses.

c Calibration plot for the correlation coefficient of the carbonate band for leucitite ATR-MIR measurements. The absorbance (height) of the peak at 1430 cm^{-1} was normalized to the integral of the 970 cm^{-1} band and plotted vs. total carbon content determined by CS analyses. A factor of 10,000 was applied to obtain reasonable numbers. TT baselines were used to measure A_{1430} and Int_{970}

2.4.5 Volatile concentrations in experimental glasses

Figure 2.5a, b show the water concentration in the glasses as function of the fluid composition. In a first experiment at 300 MPa, the fluid phase composition of the phonolite samples was wrongly measured and therefore, the experiment was repeated (here noted as 300 MPa*). The total amount of H_2O dissolved in the glasses in equilibrium with pure H_2O fluid increases with pressure from 2.07 ± 0.07 wt% at 50 MPa to 7.37 ± 0.23 wt% at 300 MPa in the phonolite melt and from 2.61 ± 0.14 wt% at 50 MPa to 7.29 ± 0.49 wt% at 300 MPa in the leucitite melt (Table 2.2, 2.3). At constant pressure, the H_2O solubility in the phonolitic and leucititic melts shows a non-linear dependence on the $X^{fl}_{H_2O}$, which can be generally fitted by a power law function ($y = ax^b$). Deviations from the described trends for the samples VES79_2_1, VES79_2_2, and VES79_3_1 - VES79_3_6 can be ascribed to an incomplete separation of the CO_2 and H_2O fluid phase during the fluid determination procedure.

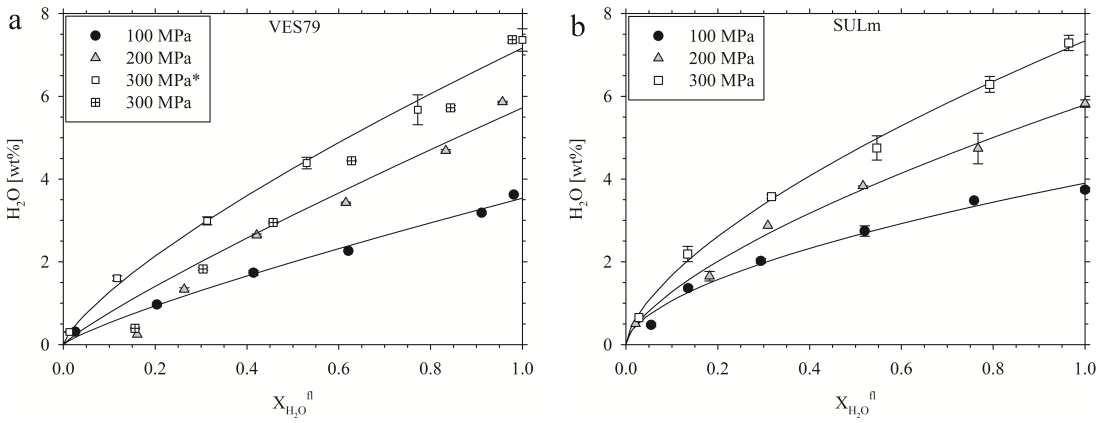

Figure 2.5: Plot of the water solubility in the melt vs. H_2O mole fraction in the fluid phase **a** in phonolitic composition with data for the first 300 MPa series with erroneous fluid determination and data for the new 300 MPa* series with improved fluid determination technique and **b** leucititic composition. Total water in the melt was determined by FTIR spectroscopy. Solid lines show trends empirically fitted as power law functions at isobaric conditions

In Fig. 2.6a, b, the concentration of CO_2 is plotted as a function of the fluid composition. The CO_2 solubility for a pure CO_2 fluid increases from 280 ± 60 ppm at 50 MPa to 1790 ± 90 ppm at 300 MPa in the phonolite melt and from 1610 ± 60

ppm at 50 MPa to 8460 ± 300 ppm at 300 MPa in the leucitite melt (Table 2.2, 2.3). CO_2 concentrations increase non linearly with increasing $X^{fl}_{CO_2}$ in the coexisting fluid in both compositions.

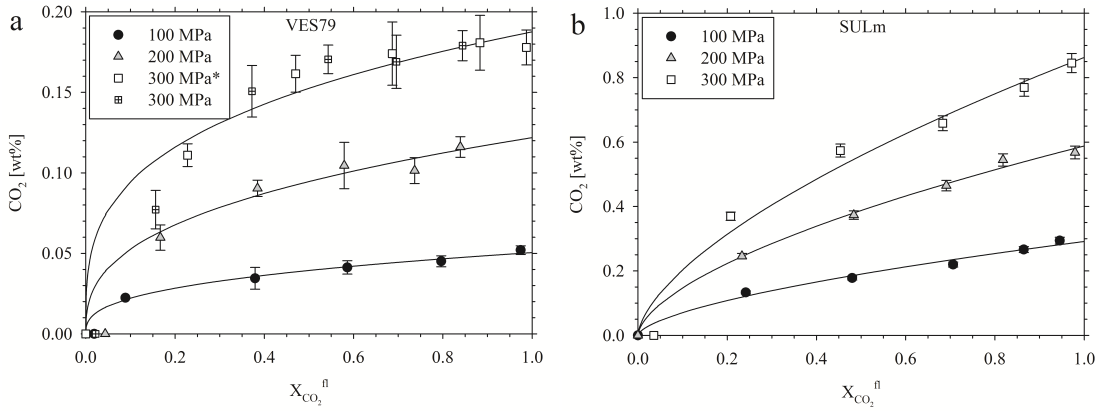

Figure 2.6: Plot of the CO_2 solubility in the melt vs. CO_2 mol fraction in the fluid phase **a** in phonolitic composition with data for the first 300 MPa series with erroneous fluid determination and data for the new 300 MPa* series with improved fluid determination technique and **b** leucititic composition. Total CO_2 content in the melts was determined by FTIR. Solid lines show trends empirically fitted as power law functions at isobaric conditions

2.5 Discussion

2.5.1 Determination of the fluid composition

The determination of the fluid composition that was in equilibrium with the silicate melt is an important analytical step in mixed volatile solubility studies, especially for defining the relation between solubility and partial fluid pressure or fugacity. The gravimetrical procedure which we applied is a common method that was used in numerous previous studies, (see Tamic et al. 2001 for an accurate description of the original procedure) and has the advantage that it requires little equipment. The downside of the method is that repeated measurements are not possible and one has only one attempt per sample. In an early stage of our study, we realized that the $X^{fl}_{H_2O}$ determined by our procedure were sometimes much too high. Good examples for such cases are samples VES_2_1 and VES_3_1 in Fig. 2.5a, which were prepared at 200 and 300 MPa with nominally pure CO_2 fluid. However, the gravimetric fluid determination yielded $X^{fl}_{H_2O}$

of 0.161 and 0.156, respectively (Table 2.2), but the water contents of these samples are only 0.24 and 0.39 wt% , suggesting a much lower $X_{H_2O}^{fl}$ of less than 0.05 (derived from Fig. 2.5a). A likely cause for an elevated $X_{H_2O}^{fl}$ in the gravimetric fluid determination is the bursting of bubbles during the heating step in the drying oven. Although we set the temperature to 75 °C, bubbles with thinner walls may have still cracked open and consequently released CO_2 and H_2O, which then accounts for additional apparent H_2O in the fluid phase. This problem seems to be more evident for samples quenched from higher pressures, as those bubbles have higher internal pressures. Indeed, we observed by optical microscopy bubbles with small cracks propagating into the surrounding glass and Raman spectroscopy confirmed that these bubbles were empty. Based on this experience, we repeated the 300 MPa experiments for the phonolite glass (series VES_3_1* – VES_3_6*, open squares in Fig. 2.5a), as the first series (crossed squares in Fig. 2.5a) contained numerous bubbles. The fluid determination procedure was modified by extracting the water from the capsules at 35 °C and at 20% of humidity in a desiccator for about 24 h to prevent fragile bubbles from bursting. Experimental glasses showed comparable amounts of bubbles, but very few of those were finally cracked, leading to an improved estimate of fluid composition.

Based on our experience, we can give the following recommendations for successful gravimetric determinations of CO_2-H_2O fluid compositions after high-pressure solubility experiments. (1) Avoid bubbles in the quenched glass using solid, bubble-free glass blocks and as little powder as possible as starting material, even if this will require longer experimental times. (2) Add sufficient H_2O and CO_2, so that after the experiment, 10 - 15 mg of free fluid phase remain in the capsules. More residual fluid results in higher accuracy of the fluid composition as weighing errors and bubbles ruptured during the gravimetrical procedure have less effect. On the contrary, depending on the investigated composition and on its amount of silicate, the presence of a water-rich fluid phase may lead to the loss of some melt components (i.e., alkalis) into the fluid phase. (3) Use a high precision balance (5 digits, 0.01 mg) for improved analytical precision.(4) Extract H_2O at about 30 °C in a desiccator with drying agent.

2.5.2 CO_2-H_2O solubility curves for leucititic and phonolitic melts

The CO_2 vs. H_2O solubility plots for phonolitic and leucititic melts at temperature of 1250 °C and pressures of 100, 200 and 300 MPa are shown in Fig. 2.7a, b, respectively. As pointed out by Behrens et al. (2009), this data representation has the advantage that an accurate determination of the fluid composition is not per se required and even samples where the fluid composition is unknown (e.g., due to failed fluid determination) can be used to construct the saturation curves. These isobars (solid lines in Fig. 2.7) represent the equilibrium concentrations of H_2O and CO_2 in the investigated melts at the experimental conditions. They are plotted as an empirical fit of the experimental data with the $X^{fl}_{H_2O}$= 1 data point as a fix point, since this sample is in equilibrium with a fluid phase with the least uncertainty. Dashed lines are isopleths of constant fluid composition in mole fraction of water. The isopleths with given $X^{fl}_{H_2O}$ were plotted by calculating the c_{H_2O} from the trend line in the c_{H_2O} vs. $X^{fl}_{H_2O}$ plot (Fig. 2.5a, b). The corresponding c_{CO_2} values were determined using the isobars in Fig. 2.7a, b, respectively. Isopleths were then fitted as exponential functions, constrained to pass through the zero intercept.

Our data show that the solubility of pure water in phonolitic and leucititic melts is quite similar up to 300 MPa at 1250 °C. However, it must be noted that this high temperature is unlikely for a silica-rich magma such as a phonolite. At constant pressure, the water solubility increases as temperature decreases. Therefore, at a temperature more realistic for natural, silicic magmas, a higher water content is expected as shown by Schmidt & Behrens (2008) measuring approx. 8 wt% H_2O at 850 – 900 °C and 300 MPa. On the contrary, the CO_2 solubility at $X^{fl}_{CO_2}$= 1 is higher in the leucititic than in the phonolitic melt (8460 vs. 1790 ppm at 300 MPa). The solubility of H_2O-CO_2-bearing fluids in our melts agree well with the previous studies on alkali-rich and alkali-poor mafic melts (Fanara et al. 2015, Shishkina et al. 2010, 2014) and on alkali-rich shoshonitic, phonotephritic, and trachytic melts (Iacono-Marziano et al. 2007, 2012, Behrens et al. 2009, Fanara et al. 2015, Vetere et al. 2012, 2014). The water content in the above-mentioned melts in equilibrium with pure H_2O fluids does not significantly differ, although there may be some variations due to melt composition

in more evolved melts, as discussed in Schmidt & Behrens (2008).

The CO_2 solubility up to 500 MPa was investigated in the previous studies only for alkali-rich series. For instance, at 300 MPa the CO_2 content in the alkaline trend decreases from about 3000 ppm in alkalibasaltic and shoshonitic melts (Shishkina et al. 2014, Vetere et al. 2012) to approx. 1200 ppm in latitic and trachytic melts. The CO_2 content in the high alkaline series varies from approx. 7500 ppm in Ca-rich leucitite to approx. 5000 ppm in phonotephritic melts to approx. 2500 ppm in phonolite (Brooker et al. 1999a). Our new data for CO_2 solubility at 300 MPa and 1250 °C in the K-rich suite decrease from 8500 ppm in a leucititic melt to 1800 ppm in a phonolitic melt. In general, it can be stated that the maximum CO_2 solubility increases from subalkaline to alkaline to ultrapotassic compositions for the mafic endmembers, while the evolution of a magma within any of the suites leads progressively to decreased CO_2 solubility.

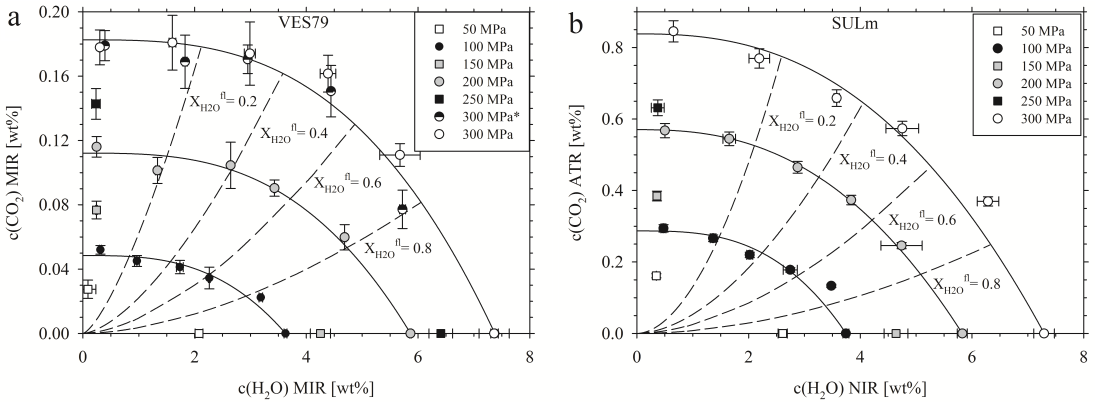

Figure 2.7: Plot of the concentrations of CO_2 vs. H_2O in the melt for phonolitic (**a**) and leucititic (**b**) compositions. Solid lines are empirically fitted isobars. The fluid isopleths (dashed lines) with given $X^{fl}_{H_2O}$ were plotted by calculating the cH_2O from the trend lines in the cH_2O vs. $X^{fl}_{H_2O}$ plot (Fig. 2.5a, b). The corresponding cCO_2 values were determined using the isobars in **a**, **b**. Isopleths were then fitted as exponential functions. Plot (**a**) shows old 300 MPa (white dots) and repeated 300 MPa* (half black dots) data set. Both data sets were used for fitting the isobar, while only new 300 MPa* data set with improved fluid determination technique was used for fitting the isopleths

This study reports the first data on solubility of CO_2 and H_2O-CO_2 mixed fluids for phonolitic and leucititic melts. Furthermore, the investigated compositions are charac-

terized by a higher K content in respect to the previous solubility studies. Our data show the large effect of the melt composition on the solubility of CO_2. In fact, the leucititic SULm composition can dissolve up to five times more CO_2 than the phonolitic VES79 composition under the same temperature and pressure conditions. Although it can be stated that the melt composition is affecting the CO_2 solubility greatly, its control on the CO_2 content and on the CO_2 incorporation mechanisms is complicated and still poorly known. The previous studies showed that CO_2 solubility is controlled by a complicated interplay between elements. In general, increasing the content of modifier cations increases the melt depolymerization, consequently enhancing the CO_2 solubility. However, the type of the added modifier cation strongly affects the intensity of the increase in CO_2 solubility. For instance, the addition of Mg and Fe has less effect on CO_2 solubility than the increase in the alkali content (Iacono-Marziano et al. 2012, Vetere et al. 2014).

The experimental H_2O-CO_2 solubility data presented in this study may be used by modelers to improve H_2O-CO_2 solubility predictions in SiO_2-poor, ultrapotassic melts. A precise knowledge of H_2O-CO_2 solubility is fundamental, for instance, to interpret melt inclusion data. Although, for the investigated volcanic areas, comprehensive studies on volatiles in melt inclusions are still missing in particular with respect to the CO_2 component, we can compare our experimental data to few melt inclusions in leucite and sanidine crystals from the 79AD eruption of Vesuvius published by Cioni (2000). It must be noted that melt inclusions in leucite are probably degassed. However, in case of melt inclusions preserving their original fluid phase, the H_2O-CO_2 content will allow an estimation of the minimum pressure of entrapment. In this case, comparing our experimental values with the above-mentioned melt inclusion data, a minimum pressure of entrapment of approximately 100 MPa could be estimated. The melt inclusions in sanidine show a CO_2 content below the detection limit of the FTIR. Nevertheless, in this case comparing the water content (approx. 6 wt%) to our solubility curve, a minimum pressure of approx. 250 MPa can be estimated.

Eventually, H_2O-CO_2 solubility data are also of key importance in working out the volatile budget for natural degassing processes as well as for experimental decompression studies.

2.5.3 Comparison with numerical models

Several numerical models are available to predict the solubility of H_2O-CO_2 mixed fluids in silicate melts with key compositions (i.e., basalt-to-rhyolite). After the first two attempts of Papale (1999) and Newman & Lowenstern (2002), Papale et al. (2006) presented a model taking into account the compositional variations from basalts to rhyolites and doubling the previous data set of solubility of C-O-H in silicate liquids, that was at that time, however, still limited if compared to the wide compositional range of natural melts. A more recent semi-empirical H_2O-CO_2 solubility model by Iacono-Marziano et al. (2012) highlighted the effect of melt structure and composition on CO_2 solubility. This model predicts the solubility in alkali-rich basaltic melts based on simplified concepts of gas-melt thermodynamics, coupled with a parametrization of both chemical composition and structure of the silicate melt. Lately, Ghiorso & Gualda (2015) published a thermodynamic model to predict the saturation conditions of H_2O-CO_2 mixed fluids in silicate melts. Their model is calibrated by published experimental data on water and carbon dioxide solubility, and mixed fluid saturation in silicate liquids. The water is expected to dissolve forming hydroxyl melt species, and carbon dioxide is considered as molecular species and carbonate ions complexed with calcium.

We compare our experimental data with the above-mentioned models in Fig. 2.8a, b. In general, all three models predict pure H_2O solubility fairly well, while showing varying deviations from experimental solubility for mixed H_2O-CO_2 and pure CO_2 fluids. The MELTS-Rhyolite model from Ghiorso & Gualda (2015) fits closest to our experimental data for both compositions. In particular, the phonolitic experimental data set is well predicted, whilst the CO_2 solubility predictions for the leucititic composition show an underestimation of up to 1160 ppm at 300 MPa. It must be noted that the model predictions at 300 MPa show a maximum in CO_2 solubility at $X^{fl}_{H_2O} > 0$, which is in disagreement with our experimental findings not showing any CO_2 decrease towards pure CO_2 fluid compositions.

The model of Papale et al. (2006) fits the data set for phonolite relatively well, underestimating the CO_2 content up to approx. 600 ppm and the H_2O content up to

approx. 1 wt%. The measured solubility for leucititic melts is instead better predicted by the model of Iacono-Marziano et al. (2012), showing good agreement for the data set at 100 MPa but increasingly overestimating the CO_2 content (up to 4000 ppm at 300 MPa) and the H_2O content (up to approx. 1 wt% at 300 MPa) with increasing pressure (Table A2.2).

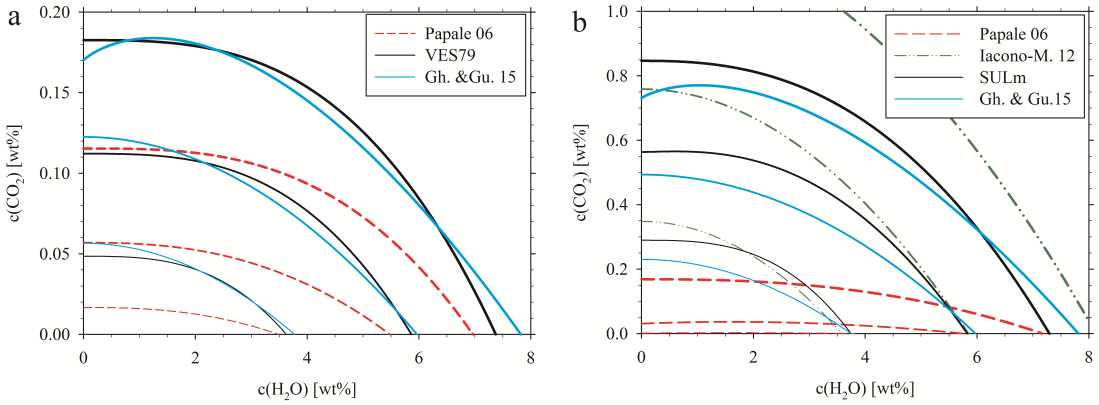

Figure 2.8: Plot of the concentrations of CO_2 vs. H_2O in the melt for phonolitic (**a**) and leucititic (**b**) compositions in comparison to numerical models by Papale et al. (2006), Iacono-Marziano et al. (2012) and Ghiorso & Gualda (2015). Note that the Iacono-Marziano et al. (2012) model is only applicable to mafic compositions and, therefore, is not used for the phonolitic melt. Thickness of the lines corresponds to the equilibrium pressure. Thin lines represent 100 MPa, medium lines represent 200 MPa, and thick lines represent 300 MPa

2.5.4 Fugacity

The obtained H_2O-CO_2 solubility in a melt is most meaningful when the composition of the coexisting fluids can be fully characterized. In general, the solubility of H_2O and CO_2 in silicate melts increases with increasing H_2O and CO_2 fugacity, respectively, and therefore with increasing pressure. In a first approximation, the H_2O or CO_2 solubility in a rhyolitic as well as in a basaltic melt is proportional to pressure for relatively low pressures, despite the different speciation in the diverse quenched glasses. This resembles a Henrian behavior (e.g., Mattey 1991, Pan et al. 1991, Blank et al. 1993, Brooker et al. 1999b). Therefore, in the pressure and temperature range considered in this study, the H_2O-CO_2 solubilities should be proportional to their fugacities and to the respective fractions in the fluid phase. If this is true, the modeling of solubility or

degassing of systems containing both H_2O and CO_2 could be significantly simplified, since only the behavior of the end-member systems (i.e. silicate-CO_2 and silicate-H_2O) and the equation of state of a mixed H_2O-CO_2 vapour needs to be determined (Blank et al. 1993). However, Fig. 2.5 and 2.6 show non-linear correlations between H_2O or CO_2 solubility and their respective fractions in the fluid, suggesting an evident non-Henrian behavior in which the deviation from linearity is increasing with increasing pressure. All the recent empirical models are taking a compositional dependence into account to predict the solubility of mixed fluids.

In Fig. 2.9, the solubility of H_2O and CO_2 is plotted as function of fugacity in phonolitic and leucititic melts. Fugacities of H_2O and CO_2 were calculated with the equation of state (EOS) of Duan & Zhang (2006) that is also integrated in the H_2O-CO_2 solubility model for silicate melts of Duan (2014). This EOS is based on empirical data, assumes non-ideal mixing of non-ideal gases and is valid from 673 to 2573 K and up to 10 GPa. The fugacity values are in good agreement (within 10%) with those calculated using a previous model by Aranovich & Newton (1999). The regressions in Fig. 2.9 were exclusively interpolated from data points of glasses equilibrated with pure H_2O or CO_2 ($X^{fl}_{H_2O}$= 1 or $X^{fl}_{CO_2}$= 1), since the fluid determination of these samples is considered to have the smallest error. In the H_2O and CO_2 fugacity plots for leucitite (Fig. 2.9a, b), all data points, regardless of experimental pressure and fluid composition, follow the regression of the data for pure H_2O or CO_2. In the case of the phonolitic composition, the water solubility for mixed H_2O-CO_2 and pure H_2O fluids follow the same trend as function of f_{H_2O} (Fig. 9c), except for two data points for 200 MPa (f_{H_2O}= 35.2 and 56.4 MPa), which are outliers due to incorrect determination of the fluid phase. Our data for the water solubility are in good agreement with those of Iacono-Marziano et al. (2007) for the same melt composition, indicating the reliability of the applied experimental and analytical methods. However, when plotting the CO_2 solubility as function of f_{CO_2}, we observe a clear mismatch between data for pure CO_2 and mixed H_2O-CO_2 fluids at 200 and 300 MPa and a smaller mismatch for the 100 MPa series (Fig. 2.9d). At similar f_{CO_2}, water-bearing samples possess enhanced CO_2 solubility. This effect seems to increase with increasing water content and pressure. We think that this behavior is not an experimental or analytical artefact, but is the real behavior of

the phonolite melt for the following reasons:

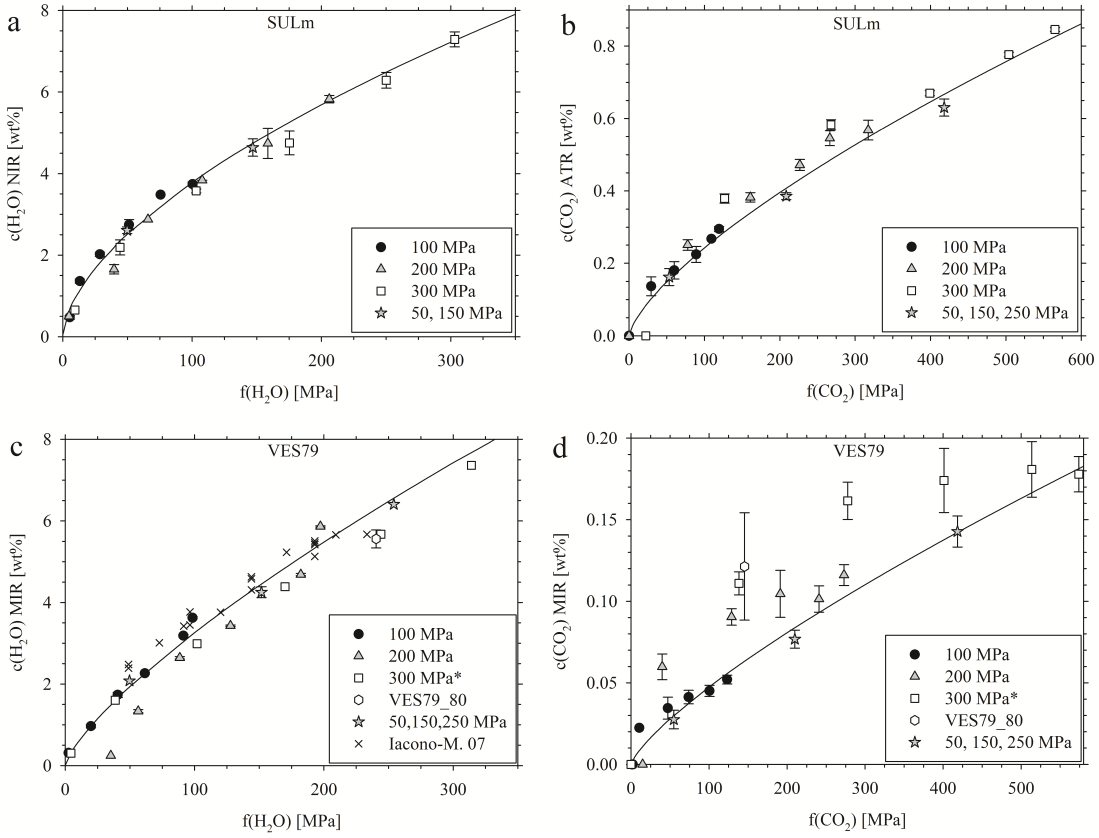

Figure 2.9: Plot of the volatile concentrations in experimental glasses vs. fugacity in the fluid phase. Solid lines are regressions, plotted by fitting power law functions to data points for pure fluid phases only. **a**,**b** Show data for the leucititic composition, and **c**, **d** show data for phonolitic composition. The two outliers in the 200 MPa sample set in plot **c** are samples with erroneous fluid determination. Data points from Iacono-Marziano et al. (2007) are experimental samples of the identical phonolite composition with $X^{fl}_{H_2O}$= 1 at various pressures. The misfit of the samples in equilibrium with mixed H_2O-CO_2 fluids in plot **d** shows the depolymerizing effect of water on highly polymerized melts leading to an enhancement of CO_2 solubility

(1) if the mismatch between pure CO_2 and mixed H_2O-CO_2 data was caused by a problem with our fluid determination, we would expect an opposing trend in the c_{H_2O} vs. f_{H_2O} plot. Furthermore, there is only a weak increase in c_{CO_2} of 200 ppm for the 300 MPa sample with $X^{fl}_{CO_2}$= 0.47 (f_{CO_2}= 277.6 MPa, VES79_3_4*) to $X^{fl}_{CO_2}$= 0.99

(f_{CO_2}= 573.9 MPa, VES79_3_1*). The shift of c_{CO_2} for the intermediate mixed H_2O-CO_2 samples at 300 MPa onto the solubility curve for pure CO_2 fluids would require an increase in $X^{fl}_{CO_2}$ by 0.3 - 0.4, which is clearly above the worst case error of the gravimetric fluid determination.

(2) Another possible reason for the mismatch in Fig. 2.9d could be a problem with the calculation of f_{CO_2} in mixed H_2O-CO_2 fluids (i.e. incorrect non-ideal mixing model). However, we applied two different models of Duan (2014) and Aranovich & Newton (1999) with agreeing results. Furthermore, the solubility data (mixed and pure CO_2) for the leucitite melt can be represented by the same regression, indicating that there is no problem with the f_{CO_2} calculation.

(3) A third reason for the mismatch in Fig. 2.9d could be erroneous CO_2 analyses for the 300 MPa samples by FTIR spectroscopy. To verify the CO_2 concentrations in VES_3_2*, VES_3_3*, and VES_3_4*, we also performed CS analyses on these samples. The results are within error similar to the FTIR data, demonstrating the validity of our analytical methods for c_{CO_2}. On the base of these arguments, we suggest that the positive deviation of the mixed fluid data in CO_2-H_2O-bearing phonolitic melts from the expected fugacity trend may be due to the depolymerization of the melt structure due to water as already suggested in the previous studies (i.e., Behrens et al. 2004, 2009, King & Holloway 2002, Mysen et al. 1975, 1976). In fact, the phonolitic composition is more polymerized (NBO/T= 0.10) than the leucititic melt (NBO/T= 0.63), and therefore, the enhancing CO_2 solubility due to the depolymerization effect of water may be more apparent in the relatively polymerized phonolite melt compared to the quite depolymerized leucitite melt.

2.6 Conclusions

H_2O-CO_2 solubility experiments were performed at 1250 °C and up to 300 MPa on K-rich phonolitic and ultrapotassic leucititic melts from central Italy. Molar extinction coefficients of molecular water, hydroxyl groups, and carbonate groups were determined for both melts. In addition, micro-ATR-FTIR analysis was used for the quantification of the CO_2 content in leucititic glasses, which showed total adsorption for carbonate

bands in MIR transmission spectra. The fluid phase compositions in equilibrium with the silicate melts were quantified using a modified gravimetric procedure.

At pressures up to 300 MPa, H_2O solubility in phonolitic and leucititic melts does not differ strongly and fits well within the frame of water solubilities in diverse silicate melts from the previous studies. However, CO_2 solubility varies strongly from leucititic (8500 ppm) to phonolitic (1700 ppm) melts. Comparing our data sets with previous data for different melt compositions, it is evident that, while keeping the SiO_2 content constant, the CO_2 solubility increases from subalkaline over alkaline to alkali-rich compositions.

The obtained experimental data show that recent empirical solubility models based on more abundant, less exotic melt compositions are successful in predicting the H_2O solubility, but do not accurately predict the solubility of CO_2 and of mixed H_2O-CO_2 fluids in our K-rich melts. The deviation from these numerical models increases with increasing pressure. Therefore, our new experimental data can be used to improve the existing numerical models on H_2O-CO_2 solubility in alkali-rich compositions.

H_2O-CO_2 fugacities in our experiments were calculated using the model of Duan (2014). When plotting the CO_2 solubility as function of f_{CO_2} for phonolitic melts, a mismatch between data for pure CO_2 and mixed H_2O-CO_2 fluids was observed. This mismatch is due to enhanced CO_2 solubility by the presence of water. This effect increases as water content and pressure increase. As suggested by other authors, the positive effect of water on CO_2 solubility in CO_2-H_2O-bearing phonolitic melts may be due to the depolymerizing effect of water in relatively polymerized melts. The obtained experimental data in comparison with natural melt inclusions may be useful to accurately constrain pressure conditions of magma storage and degassing processes during ascent.

References

Aranovich, L. Y. & Newton, R. C. (1999). Experimental determination of CO_2–H_2O activity-composition relations at 600 - 1000 °C and 6 – 14 kbar by reversed decarbonation and dehydration reactions. *American Mineralogist*, 84, 1319–1332.

Aubaud, C., Hirschmann, M. M., Withers, A. C., & Hervig, R. L. (2008). Hydrogen partitioning between melt, clinopyroxene, and garnet at 3 GPa in a hydrous MORB with 6 wt% H_2O. *Contributions to Mineralogy and Petrology*, 156, 607–625.

Behrens, H., Misiti, V., Freda, C., Vetere, F., Botcharnikov, R. E., & Scarlato, P. (2009). Solubility of H_2O and CO_2 in ultrapotassic melts at 1200 and 1250 °C and pressure from 50 to 500 MPa. *American Mineralogist*, 94, 105–120.

Behrens, H., Ohlhorst, S., Holz, F., & Champenois, M. (2004). CO_2 solubility in dacitic melts equilibrated with H_2O–CO_2 fuids: implications for modeling the solubility of CO_2 in silicic melts. *Geochimica et Cosmochimica Acta*, 68, 4687–4703.

Behrens, H., Romano, C., Nowak, M., Holz, F., & Dingwell, D. B. (1996). Near-infrared spectroscopic determination of water species in glasses of the system $MAlSi_3O_8$ (M= Li, Na, K): an interlaboratory study. *Chemical Geology*, 128, 41–63.

Benne, D. & Behrens, H. (2003). Water solubility in haplobasaltic melts. *European Journal of Mineralogy*, 15, 803–814.

Blank, J. G. & Brooker, R. A. (1994). Experimental studies of carbon dioxide in silicate melts: solubility, speciation, and stable carbon isotope behavior. *Reviews in Mineralogy and Petrology*, 30, 157–186.

Blank, J. G., Stolper, E. M., & Carroll, M. R. (1993). Solubilities of carbon dioxide and water in rhyolitic melt at 850 °C and 750 bars. *Earth and Planetary Science Letters*, 119, 27–36.

Botcharnikov, R. E., Behrens, H., & Holz, F. (2006). Solubility and speciation of C–O–H fluids in andesitic melt at T= 1100 – 1300 °C and P= 200 and 500 MPa. *Chemical Geology*, 229, 125–143.

Brooker, R. A., Kohn, S. C., Holloway, J. R., & McMillan, P. F. (1999a). Structural controls on the solubility of CO_2 in silicate melts. *Chemical Geology*, 174, 225–239.

Brooker, R. A., Kohn, S. C., Holloway, J. R., McMillan, P. F., & Carroll, M. R. (1999b). Solubility, speciation and dissolution mechanisms for CO_2 in melts on the $NaAlO_2$–SiO_2 join. *Geochimica et Cosmochimica Acta*, 63, 3549–3565.

Bruno, P. P. G., Cippitelli, G., & Rapolla, A. (1998). Seismic study of the Mesozoic carbonate basement around Mt. Somma–Vesuvius, Italy. *Journal of Volcanology and Geothermal Research*, 84, 311–322.

Burnham, C. W. (1979). *The evolution of the igneous rocks: ffteenth anniversary perspectives*, chapter The importance of volatile constituents, (pp. 439–482). Princeton University Press.

Caricchi, L., Sheldrake, T. E., & Blundy, J. (2018). Modulation of magmatic processes by

REFERENCES

CO_2 flushing. *Earth and Planetary Science Letters*, 491, 160–171.

Cioni, R. (2000). Volatile content and degassing processes in the AD 79 magma chamber at Vesuvius (Italy). *Contributions to Mineralogy and Petrology*, 140, 40–54.

D'Antonio, M. (2011). Lithology of the basement underlying the Campi Flegrei caldera: volcanological and petrological constraints. *Journal of Volcanology and Geothermal Research*, 200, 91–98.

Deegan, F. M., Troll, V. R., Freda, C., Misiti, V., Chadwick, J. P., McLeod, C. L., & Davidson, J. P. (2010). Magma–carbonate interaction processes and associated CO_2 release at Merapi Volcano, Indonesia: insights from experimental petrology. *Journal of Petrology*, 51, 1027–1051.

Duan, X. (2014). A general model for predicting the solubility behavior of H_2O–CO_2 fluids in silicate melts over a wide range of pressure, temperature and compositions. *Geochimica et Cosmochimica Acta*, 125, 582–609.

Duan, Z. & Zhang, Z. (2006). Equation of state of the H_2O, CO_2, and H_2O–CO_2 systems up to 10 GPa and 2573.15 K: molecular dynamics simulations with ab initio potential surface. *Geochimica et Cosmochimica Acta*, 70, 2311–2324.

Fanara, S., Behrens, H., & Zhang, Y. (2013). Water diffusion in potassiumrich phonolitic and trachytic melts. *Chemical Geology*, 346, 149–161.

Fanara, S., Botcharnikov, R. E., Palladino, D. M., Adams, F., Buddensieck, J., Mulch, A., & Behrens, H. (2015). Volatiles in magmas related to the Campanian Ignimbrite eruption: experiments vs. natural fndings. *American Mineralogist*, 100, 2284–2297.

Freda, C., Gaeta, M., Giaccio, B., Marra, F., Palladino, D. M., Scarlato, P., & Scottili, G. (2011). CO_2-driven large mafic explosive eruptions: the Pozzolane Rosse case study from the Colli Albani Volcanic District (Italy). *Bulletin of Volcanology*, 73, 241–256.

Freda, C., Gaeta, M., Palladino, D. M., & Trigila, R. (1997). The Villa Senni Eruption (Alban Hills, central Italy): the role of H_2O and CO_2 on the magma chamber evolution and on the eruptive scenario. *Journal of Volcanology and Geothermal Research*, 78, 103–120.

Gaeta, M., Freda, C., Christensen, J. N., Dallai, L., Marra, F., Karner, D. B., & Scarlato, P. (2006). Time-dependent geochemistry of clinopyroxene from the Alban Hills (Central Italy): clues to the source and evolution of ultrapotassic magmas. *Lithos*, 86, 330–346.

Ghiorso, M. S. & Gualda, G. A. R. (2015). An H_2O–CO_2 mixed fluid saturation model compatible with rhyolite-MELTS. *Contributions to Mineralogy and Petrology*, 169, 1245.

Goff, F., Love, S. P., Warren, R. G., Counce, D., Obenholzner, J., Siebe, C., & Schmidt, S. C. (2015). Passive infrared remote sensing evidence for large, intermittent CO_2 emissions at Popocatépetl volcano,Mexico. *Chemical Geology*, 177, 133–156.

Iacono-Marziano, G. (2004). *Equilibrium and disequilibrium degassing of a phonolitic melt simulated by decompression experiments*. PhD thesis, University of Palermo.

Iacono-Marziano, G., Morizet, Y., Le Trong, E., & Gilliard, F. (2012). New experimental data and semi-empirical parameterization of H_2O–CO_2 solubility in mafic melts. *Geochimica et Cosmochimica Acta*, 97, 1–23.

Iacono-Marziano, G., Schmidt, B. C., & Dolfi, D. (2007). Equilibrium and disequilibrium degassing of a phonolitic melt (Vesuvius AD

79 “white pumice”) simulated by decompression experiments. *Journal of Volcanology and Geothermal Research*, 161, 151–164.

Jeffrey, A. J., Gertisser, R., Troll, V. R., Jolis, E. M., Dahren, B., Harris, C., Tindle, A. G., Preece, K., O'Driscoll, B., Humaida, H., & Chadwick, J. P. (2013). The pre-eruptive magma plumbing system of the 2007–2008 dome-forming eruption of Kelut volcano, East Java, Indonesia. *Contributions to Mineralogy and Petrology*, 166, 275–308.

Jolis, E. M., Troll, V. R., Harris, C., Freda, C., Gaeta, M., Orsi, G., & Siebe, C. (2015). Skarn xenolith record crustal CO_2 liberation during Pompeii and Pollena eruptions, Vesuvius volcanic system, central Italy. *Chemical Geology*, 415, 17–36.

King, P. L. & Holloway, J. R. (2002). CO_2 solubility and speciation in intermediate (andesitic) melts: the role of H_2O and composition. *Geochimica et Cosmochimica Acta*, 66, 1627–1640.

Lentini, F. (1982). The geology of the Mt. Etna basement. *Memorie della Società Geologica Italiana*, 23, 7–25.

Lesne, P., Scaillet, B., Pichavant, M., & Beny, J.-M. (2011a). The carbon dioxide solubility in alkali basalts: an experimental study. *Contributions to Mineralogy and Petrology*, 162, 153–168.

Lesne, P., Scaillet, B., Pichavant, M., Iacono-Marziano, G., & Beny, J.-M. (2011b). The H_2O solubility of alkali basaltic melts: an experimental study. *Contributions to Mineralogy and Petrology*, 162, 133–151.

Lowenstern, J. B. & Pitcher, B. W. (2013). Analysis of H_2O in silicate glass using attenuated total reflectance (ATR) micro-FTIR spectroscopy. *American Mineralogist*, 98, 1660–1668.

Mattey, D. P. (1991). Carbon dioxide solubility and carbon isotope fractionation in basaltic melt. *Geochimica et Cosmochimica Acta*, 55, 3467–3473.

Moore, G., Vennemann, T., & Carmichael, I. S. E. (1981). An empirical model for the solubility of H_2O in magmas to 3 kilobars. *American Mineralogist*, 83, 36–42.

Moussallam, Y., Morizet, Y., & Gaillard, F. (2016). H_2O–CO_2 solubility in low SiO_2-melts and the unique model of kimberlite degassing and emplacement. *Earth and Planettary Science Letters*, 447, 151–160.

Mysen, B. O., Arculus, R. J., & Eggler, D. H. (1975). Solubility of carbon dioxide in melts of andesite, tholeiite, and olivine nephelinite composition to 30 kbar pressure. *Contributions to Mineralogy and Petrology*, 53, 227–239.

Mysen, B. O., Eggler, D. H., Seitz, M. G., & Holloway, J. R. (1976). Carbon dioxide in silicate melts and crystals; part I, solubility measurements. *American Journal of Science*, 276, 455–479.

Newman, S. & Lowenstern, J. B. (2002). VolatileCalc: a silicate melt-H_2O–CO_2 solution model written in Visual Basic for excel. *Computers & Geosciences*, 28, 597–604.

Ni, H. & Keppler, H. (2013). Carbon in silicate melts. *Reviews in Mineralogy and Geochemistry*, 75, 251–287.

Norini, G., Capra, L., Groppelli, G., Agliardi, F., Pola, A., & Cortes, A. (2010). Structural architecture of the Colima Volcanic Complex. *Journal of Geophysical Research*, 115, 1808.

Pan, V., Holloway, J. R., & Hervig, R. L. (1991). The pressure and temperature dependence of carbon dioxide solubility in tholeiitic basalt melts. *Geochimica et Cosmochimica Acta*, 55, 1587–1595.

REFERENCES

Papale, P. (1999). Modeling of the solubility of a two-component H_2O+CO_2 fluid in silicate liquids. *American Mineralogist*, 84, 477–492.

Papale, P., Moretti, R., & Barbato, D. (2006). The compositional dependence of the saturation surface of H_2O + CO_2 fluids in silicate melts. *Chemical Geology*, 229, 78–95.

Roux, J. & Lefèvre, A. (1992). A fast-quench device for internally heated pressure vessels. *European Journal of Mineralogy*, 4, 279–282.

Schmidt, B. C. & Behrens, H. (2008). Water solubility in phonolite melts: influence of melt composition and temperature. *Chemical Geology*, 256, 259–268.

Schmidt, B. C., Blum-Oeste, N., & Flagmeier, J. (2013). Water diffusion in phonolite melts. *Geochimica et Cosmochimica Acta*, 107, 220–230.

Scholze, H. (1960). Zur Frage der Unterscheidung zwischen H_2O-Molekeln und OH-Gruppen in Gläsern und Mineralen. *Naturwissenschaften*, 10, 226–227.

Shishkina, T. A., Botcharnikov, R. E., Holz, F., Almeev, R. R., Jazwa, A. M., & Jakubiak, A. A. (2014). Compositional and pressure effects on the solubility of H_2O and CO_2 in mafic melts. *Chemical Geology*, 388, 112–129.

Shishkina, T. A., Botcharnikov, R. E., Holz, F., Almeev, R. R., & Portnyagin, M. V. (2010). Solubility of H_2O- and CO_2-bearing fluids in tholeiitic basalts at pressures up to 500 MPa. *Chemical Geology*, 277, 115–125.

Tamic, N., Behrens, H., & Holz, F. (2001). The solubility of H_2O and CO_2 in rhyolitic melts in equilibrium with a mixed CO_2–H_2O fluid phase. *Chemical Geology*, 174, 333–347.

Thibault, Y. & Holloway, J. R. (1994). Solubility of CO_2 in a Ca-rich leucitite: effects of pressure, temperature, and oxygen fugacity. *Contributions to Mineralogy and Petrology*, 116, 216–224.

Troll, V. R., Hilton, D. R., Jolis, E. M., Chadwick, J. P., Blythe, L. S., Deegan, F. M., Schwarzkopf, L. M., & Zimmer, M. (2012). Crustal CO_2 liberation during the 2006 eruption and earthquake events at Merapi volcano, Indonesia. *Geophysical Research Letters*, 39, 11.

Vetere, F., Botcharnovik, R. E., Holtz, F., Behrens, H., & de Rosa, R. (2012). Solubility of H_2O and CO_2 in shoshonitic melts at 1250 °C and pressures from 50 to 400 MPa: implications for Campi Flegrei magmatic systems. *Journal of Volcanology and Geothermal Research*, 202, 251–261.

Vetere, F., Holtz, F., Behrens, H., Botcharnikov, R. E., & Fanara, S. (2014). The effect of alkalis and polymerization on the solubility of H_2O and CO_2 in alkali-rich silicate melts. *Contributions to Mineralogy and Petrology*, 167, 298.

3

Bubble nucleation and growth in H_2O-CO_2 bearing, leucititic melts from decompression experiments

Maximilian Schanofski[1], Sara Fanara[1], Burkhard C. Schmidt[1]

[1]Geowissenschaftliches Zentrum, Georg-August-Universität (GZG),
Goldschmidtstraße 1, 37077 Göttingen, Germany

3.1 Abstract

Continuous rapid decompression experiments have been performed with a leucititic melt, corresponding to a synthetic analogue of the Pozzolane Rosse eruption of the Colli Albani 456 ka ago. Three sample series with different H_2O-CO_2 fluid phases with $X^{fl}_{CO_2} \approx 0$, 0.5 and 1 have been studied at a constant experimental temperature of 1250 °C and an initial pressure of 200 MPa. Final pressures between 150 and 33 MPa were reached after decompression with constant rate $\Delta P/\Delta t$ of about 1 MPa/s. Even though CO_2 is roughly an order of magnitude less soluble in volcanic melts than H_2O, our experiments demonstrate the major influence of CO_2 on the degassing behavior. A pure H_2O fluid shows a nucleation event of heterogeneous bubbles at a ΔP (Pressure at which the volatile bearing starting material is saturated in volatiles minus pressure after the decompression) below 50 MPa corresponding to a supersaturation pressure of

up to 65 MPa. Measured porosities reach a maximum of 32 % at a ΔP of 159 MPa. A pure CO_2 fluid nucleates bubbles homogeneously and continuously in samples with a ΔP of 94 and higher. A maximum in supersaturation pressure of 81 MPa is reached at a ΔP of 142 MPa. The samples show a lower porosity than their H_2O counterpart (up to approx. 7 % at a ΔP of 163 MPa) due to lower CO_2 solubility. H_2O-CO_2 bearing melts exsolve volatiles heterogeneously and continuously whilst building up a supersaturation pressure of up to 96 MPa at a ΔP of 124 MPa. The experimental degassing path reveals a degassing of CO_2 exclusively at low ΔP (up to 124 MPa) before degassing of H_2O kicks in at higher ΔP values, dramatically increasing the porosity and lowering the volatile supersaturation. Measured porosities reach the highest overall porosity of 44 % at ΔP of 159 MPa. All measured porosities match the modelled porosity well, showing that the technique used for porosity measurements gives trustworthy results. We propose that CO_2 dissolved in the melt is responsible for a continuous nucleation during magma ascent in contrast to distinct nucleation events in a pure H_2O fluid. At high decompression rates, H_2O is withheld in the melt up to shallow conduit depths before exsolving rapidly by degassing into the pre-existing CO_2 bubbles. CO_2 can therefore increase the magma ascent speed at shallow depths and lead to a more explosive eruption.

Keywords: Decompression experiments · H_2O · CO_2 · supersaturation · magma ascent dynamics · Pozzolane Rosse · bubble nucleation

3.2 Introduction

Modern monitoring techniques enable us to predict most volcanic eruption some time in advance. However, we are not yet able to determine how catastrophic it will be. It is known that the intensity of an eruption and therefore its destructive power depend on several factors including the size of the volcanic conduit, the type of the erupted magma as well as the amount and nature of the gasses dissolved in the deep magma (e.g., Cashman & Mangan 1994, Sparks et al. 1994, Gonnermann et al. 2013). The amount of gas that is released from the magma during its migration to the surface is one of the main factors determining the style of the eruption and its ability to form high eruptive columns and potentially destructive pyroclastic flows. Basaltic volcanoes,

which typically show effusive to low intensity hawaiian and strombolian explosive eruptions, but occasionally show high intensity subplinian to plinian explosive eruptions (Simkin & Siebert 1994, Lesher & Spera 2015) are a good example that the process of magma degassing is not fully understood up to this point.

The exsolution of volatiles dissolved in the melt such as H_2O and CO_2 (but also Cl, F and S) act as a driving force for magma ascent as they result in nucleation and growth of volatile bubbles, acting as the propulsion of eruptions (e.g., Sparks 1978). Natural magma ascent velocities show a large spectrum from 0.001 ms^{-1} in siliceous andesite compositions (Rutherford 2003) to over 200 ms^{-1} in kimberlitic conduits (Sparks et al. 2006).

Vesiculation and degassing of magmas due to decompression was widely studied through experimental and textural analyses (Shea 2017 and references therein) as well as numerical modelling (Toramaru 1995, Huber et al. 2014, Coumans et al. 2020). Even though H_2O exsolution during decompression is fairly well understood for various magma compositions due to numerous studies (e.g., Hurwitz & Navon 1994, Gardner et al. 1999, Cluzel et al. 2008, Iacono Marziano et al. 2007, Allabar & Nowak 2018) only a small amount of experimental decompression studies takes CO_2 into account.

Carbon dioxide is the second most abundant volatile component in natural magmas and can reach very high values in alkali-rich compositions (e.g., Fanara et al. 2015, Schanofski et al. 2019). It is considered the first volatile to degas at depth, potentially controlling the onset of magma degassing and having a strong impact on volcanic explosivity (e.g., Freda et al. 2011, Wallace et al. 2015, Pappalardo et al. 2018, Buono et al. 2020b). Nevertheless, few decompression experiments on rhyolitic and basaltic melts with mixed H_2O-CO_2 fluids were performed by Mourtada-Bonnefoi & Laporte (2002), Gardner & Webster (2016) and Le Gall & Pichavant (2016). Lately, isothermal decompression experiments were performed on alkaline trachytic melts at 1200 °C variable decompression rates (from 0.01 to 1 MPa/s) and H_2O-CO_2 volatile content, in order to attain homogeneous bubble nucleation (Buono et al. 2020a).

The 456 ka sub-plinian Pozzolane Rosse (PR) eruption of the Colli Albani has shown to be highly explosive in relation to its SiO_2 content (Freda et al. 2011). Previous studies have shown that the material erupted during the Pozzolane Rosse eruption was saturated with CO_2 prior to the magma ascent by assimilation of limestone (Freda et al. 2008). In particular, geochemical data, mass balance calculations and experimental data (Dallai et al. 2004, Gaeta et al. 2006, Freda et al. 2008) show that the K-foiditic magma feeding the PR eruption derived from a phono-tephritic parental magma, after crystallisation of clinopyroxene and leucite together with the assimilation of 7 wt.% of calcite from carbonate wall rocks, which would actually result into a significant amount of free CO_2 in the system. Furthermore, evidence of high f_{CO2} in the magma of the PR at the eruption onset is provided by the occurrence of magmatic calcite in the groundmass of the lava flow (Freda et al. 2008).

It has been proposed for some time that CO_2 starts degassing from a melt at greater depths than H_2O (Blundy et al. 2010) leading to a different degassing behavior of the melt in terms of nucleation and growth of bubbles. In an earlier study Schanofski et al. (2019) investigated the solubility of mixed H_2O-CO_2 fluids in the SULm composition of Freda et al. (2011) as a synthetic analogue to the leucitite magma of the Pozzolane Rosse, showing that this composition is capable of dissolving large amounts of CO_2 even at relatively low pressures (e.g. $\sim$5500 ppm at 200 MPa and 1250 °C) making it the ideal composition for studying the nucleation and growth of H_2O, CO_2 and H_2O-CO_2 vesicles. In this study we performed isothermal rapid decompression experiments with a decompression rate ($\Delta P/\Delta t$) of 1 MPa/s corresponding to an ascent rate of 35 m/s showing the effect of CO_2 on nucleation and growth of volatile bubbles.

3.3 Experimental and analytical methods

3.3.1 Synthetic starting material

A synthetic, crystal free glass with a composition close to the ultrapotassic leucitite "SULm" of Freda et al. (2011) was synthesized. Therefore oxides and carbonates were melted at ambient pressure in a Pt crucible at 1600 °C. The resulting melt was rapidly quenched by submerging the bottom of the Pt crucible in cold water. The obtained glass was crushed, grounded into a powder and remelted twice in order to produce a

crystal and bubble free, homogeneous glass. The composition and the homogeneity of the glass were checked on a polished fragment by 20 point measurements (Table 3.1) with an energy dispersive Bruker M4 Tornado micro-X-ray fluorescence (µ-XRF) spectrometer equipped with a Rhodium anode, polycapillary X-ray optics and two silicon drift detectors detector using 50 kV, 200 µA tube voltage and current, 20 µm beam diameter on the sample surface and 2 minutes acquisition time.

Table 3.1: Composition of SULm glass measured by micro-XRF analysis.

Composition	SiO_2	TiO_2	Al_2O_3	[b]Fe_2O_3	MnO	MgO	CaO	Na_2O	K_2O	total
SULm-SM	44.75 (15)	0.97 (1)	16.63 (13)	10.77 (7)	0.27 (1)	4.03 (12)	10.97 (5)	2.50 (21)	9.11 (4)	100
[a]SULm	45.55	0.97	16.55	9.72	0.23	4.02	11.03	3.09	8.83	99.99

Micro-XRF analyses are based on 20 measurements on 1 fragment of each glass.
Element concentrations obtained by the standardless µ-XRF analysis were corrected using a set of 50 natural and synthetic aluminosilicate glasses with known compositions.
All values show content in wt%. 2σ (last decimals) is given in parentheses.
[a]From Freda et al. (2011).
[b]All iron is given as Fe_2O_3.

The factory established fundamental parameter analysis of the M4 Tornado was improved by a type calibration based on about 50 aluminosilicate glasses melted from synthetic oxide powders, natural magmatic rocks or certified reference materials for which composition is known from (multiple) electron microprobe analysis.

3.3.2 Capsule preparation and experimental strategy for volatilization experiments

$Au_{75}Pd_{25}$-capsules of 4 mm outer diameter, 0.2 mm wall thickness and a length of 30 mm were used to conduct the volatilization experiments. The bottom of the capsules was crimped into a three-sided star and welded with a Lampert U3 PUK arc welder. 400 mg glass powder were filled into the capsules and compacted with a steel die of 3.5 mm diameter and a hammer. H_2O and $Ag_2C_2O_4$ as a source of CO_2 were added to the capsule before the top of the capsule was crimped flat and welded. Volatile amounts were chosen on the basis of solubility data from Schanofski et al. (2019) to obtain slightly undersaturated glasses of $X^{fl}_{H_2O}$= 0, 0.5 and 1 for experimental conditions of

200 MPa and 1250 °C. Water bearing capsules were re-weighted after storing them in a drying oven at 100 °C over night to detect possible leakage.

The volatilization experiments were conducted over 4 days in a vertically operating internally heated pressure vessel (IHPV). The vessel itself has a double end design that consists of 2 outer shells of BÖHLER W300 ESU steel and an inner shell made of BÖHLER L334 steel shrunk fit to each other. On both ends the vessel is closed by closure heads (D22S steel) and a set of Bridgeman seals, consisting of alternating layers of polyurethane and polyethylene. The closure heads are held in place by closure nuts consisting of BÖHLER W300 ESU. The bottom closure head has seven conical drillings of which 2 are used for current feedthroughs for the furnace and a rapid quench electrode and the remaining five drillings act as thermocouple feedthroughs. Electrical insulation as well as pressure seal of the feedthrough steel cones (D22S) is achieved by KYNAR®-PVDF shrinking tubes. The top closure head has two drillings for electrical feedthrough for the furnace as well as a bore for connection to the pressure line.

The double-wire-element furnace designed after Holloway et al. (1992) is built around a threaded ceramic tube (Friatec Degussit AL23) with 15 mm inner diameter, 21 mm outer diameter and 182 mm length. The two heating loops (0.8 mm $Pt_{90}Rh_{10}$ wire) are wrapped around the ceramic tube. The bottom loop consists of 44 windings over 67.5 mm. After a gap of 6.5 mm the top loop consisting of 33 windings over 50.5 mm starts. Both loops share the bottom electric connection but have separate electrical connections on the top end. Thermal insulation of the furnace is achieved by six layers of RATH KP 1600 fabric that are held in place by a Ni foil mantle. The furnace is sitting in a stainless-steel hull, that can be fixed on the sample holder.

The ceramic sample holder with 185 mm length and an inner diameter of 8.5 mm is fixed on the bottom mushroom head and has vertical carvings to guide the three S-Type thermocouples and two 0.6 mm diameter Molybdenum rapid quench electrodes. The S-Type thermocouples are distributed over a length of 30 mm with the bottom thermocouple being placed at the top winding of the bottom heating loop. The bottom and top thermocouples are used to control the temperature of the furnace using the two heating loops. Allowing for an isothermal sample storage region of 30 mm with a

thermal gradient of max. ± 20 °C depending on the experimental pressure.

Prior to the experiment the vessel is filled twice with 10 MPa of Argon in order to flush out the atmosphere, of which the first flushing is done at room temperature whereas the second flushing is performed at 100 °C. Pressure is build up in two steps. Up to ∼170 MPa a compressor (Maximator DLE 75-2-UU) is used whereas for higher pressures up to 500 MPa a pressure intensifier (Sitec 753.7016-45) takes over.

Table 3.2: Experimental conditions and results of H_2O and CO_2 volatilization experiments

Sample	Glaspowder [mg]	H_2O [mg]	$Ag_2C_2O_4$ [mg]	Duration [h]	Pressure [Mpa]	[a]H_2O_{tot} [wt%]	[a]CO_2 [ppm]	[b]Remarks
A9	400	23.4	0.0	70	271	5.14 (31)	n.d.	
A10	400	23.3	0.0	70	271	5.24 (26)	n.d.	
A11	401	23.3	0.0	94	205	5.55 (41)	n.d.	
B6	400	0	7.8	44	250	0.16 (1)	5356 (188)	
B16	200	0.3	4.2	94	249	0.12 (1)	4803 (414)	b
B18	300	0	6.2	94	205	0.49 (4)	4973 (386)	
C10	400	14.9	5.2	44	250	3.86 (26)	3402 (120)	
C17	400	15.9	17.5	94	200	3.72 (21)	3163 (198)	b
C18	400	16.7	18.3	94	200	3.66 (18)	3137 (164)	b

All experiments were run at 1250 °C.
[a]Measured by FTIR spectroscopy using ϵ values from Schanofski et al. (2019)
[b]b= minor amount of volatile bubbles present after the experiment

For this study, experiments were carried out at 1250 °C and pressures ≥ 200 MPa with Argon as pressure medium at an intrinsic oxygen fugacity (f_{O2}= NNO + 3 ± 1). The IHPV is equipped with a rapid quench device similar to that of Roux & Lefèvre (1992), in which the capsules are placed in a Pt cup that is suspended from a $Pt_{90}Rh_{10}$ quench wire. Quenching is accomplished by electrically melting the quench wire and the drop of the samples from the hot, isothermal zone into the cold, bottom part of the furnace. The quench rate for similar experiments was determined by Benne & Behrens (2003) to be about 150 K/s. The obtained volatilized glass cylinders were crystal-free and

in some CO_2 bearing cases showed a minor amount of bubbles. The H_2O and CO_2 content of every volatilized starting material was checked on doubly polished sections from the center of the experimental glass cylinders via FTIR spectroscopy using the extinction coefficients from Schanofski et al. (2019). The experimental conditions and volatile content of the volatilized glasses are listed in Table 3.2.

3.3.3 Capsule preparation and experimental strategy for decompression experiments

$Au_{75}Pd_{25}$-capsules of 4 mm outer diameter, 0.2 mm wall thickness and 20 mm length were prepared for the decompression experiments. The bottom of the capsules was crimped into a tree sided star and welded shut. Cylindrical pieces of the volatile bearing starting materials were inserted prior to evacuating the capsule to a vacuum of 10^{-2} mbar to minimize the amount of trapped air. The capsule was placed in a vice of a gas loading apparatus (Boettcher & Buo 1989) and was closed vacuum tight before welding. In a later stage of the study, we discovered that in particular for decompression experiments with a high final pressure above 100 MPa, this method was not sufficient enough for evacuating the capsule. Therefore, we decided to weld the capsules without applying a vacuum and put them under 200 MPa of pressure in a CSPV afterwards. As a result the capsule walls were tightly pressed against the glass cylinders. We then cut a part of the flat crimped capsule, which allowed the trapped and now compressed air to escape before we rewelded the capsules for the decompression experiments.

Prior to the decompression step, the samples were rehomogenized for another 4 days in the IHPV at identical conditions as used for the volatilization. Subsequently the samples were isothermally decompressed with a rate of about 1 MPa/s to final pressures (P_f) of 200, 150, 100, 50 or 30 MPa using the decompression unit attached to the IHPV. Since the automatic decompression unit consisting of a combination of an electric spindle press (Sitec 750.1701-50H2) and a motor driven micro metering valve that allow for a stepwise decompression, is not capable of achieving decompression speeds as high as 1 MPa/s, only the motor driven micro metering valve was used to decompress manually and continuously. After the final pressure was reached, the samples were rapidly quenched without delay at a rate of 150 K/s. The experimental conditions and volatile content of the decompressed glasses are listed in Table 3.3.

Table 3.3: Experimental conditions and results of decompression experiments

Sample	Glass [mg]	Duration [h]	Pressure [MPa]	P_{sv} [MPa]	P_f [MPa]	ΔP [MPa]	$\Delta P/\Delta t$ [MPa/s]	$^{c}H_2O_{tot}$ [wt%]	$^{c}CO_2$ [ppm]	X^{fl}_{H2O}	P_{sd} [MPa]	P_{ss} [MPa]	VND_n [mm-3]	Φ_m [%]	Φ_{equ} [%]	$\Phi_{Tg}{}^{12}$ [%]	^{d}Remarks
A11_D200	176	108	204	198	204	-6	0	5.48 (30)	-	-	193	-11	6	0.2 (5)	0.6	0.3	NL
A_D150	136	94	199	^{b}199	150	49	0.98	5.52 (38)	-	0.99	196	46	443	0.6 (2)	3.3	1.2	
A10_D100	108	92	201	179	101	78	1.01	5.02 (28)	-	-	166	65	1548	1.0 (3)	3.4	1.0	
A9_D50	115	90	200	173	57	116	0.95	3.32 (16)	-	1.00	79	22	36	12(3)	34.8	12.0	
A_D30	119	91	199	^{b}199	40	159	0.94	2.92 (17)	-	0.99	62	22	69	32 (3)	55.1	29.8	
B18_D200	169	108	204	182	204	-22	0	0.62 (10)	4874 (528)	-	179	-25	99	0.1 (1)	0.1	0.0	
B16_D150	99	94	199	^{a}200	150	50	0.98	0.87 (7)	4978 (342)	-	182	32	73	0.1 (1)	0.0	0.0	
B6_D100	88	48	201	196	102	94	0.99	0.16 (5)	3439 (330)	-	126	24	170	0.4 (3)	1.7	1.3	n.v.
B6_D50	81	46	204	196	54	142	0.94	0.18 (3)	3696 (288)	^{e}0.79	135	81	1574	3 (1)	2.5	1.7	NQ
B6_D30	87	72	204	196	33	163	0.95	0.23 (9)	1822 (125)	0.11	67	34	1991	29 (4)	7.8	5.4	NQ
C18_D200	108	94	205	^{a}200	205	-5	0	3.83 (23)	3510 (214)	-	195	-10	44	0.1 (2)	0.6	0.26	
C17_D150	99	94	199	^{a}200	150	50	0.98	3.89 (39)	3573 (227)	-	199	49	298	0.1 (1)	0.0	0.01	
C10_D100	92	48	201	192	102	90	0.99	3.73 (25)	2807 (237)	-	168	66	813	1.3 (9)	2.6	0.92	
C17_D75	68	88	204	^{a}200	76	124	0.96	3.91 (22)	2704 (166)	-	172	96	1286	0.8 (3)	0.9	0.56	
C10_D50	85	46	204	192	54	138	0.94	2.33 (25)	824 (109)	0.90	66	12	149	16 (2)	34.3	13.95	NQ, NL
C10_D30	97	72	204	192	33	159	0.95	1.83 (11)	682 (244)	0.92	52	19	38	44 (4)	52.9	33.92	NQ, NL

All experiments were carried out at 1250 °C

P_{sv}= volatile solubility pressure of the starting glass; P_f= final pressure; P_{sd}= volatile solubility pressure of decompressed glass; P_{ss}= supersaturation pressure; Φ_m= measured porosity; Φ_{equ}= calculated porosity at 1250 °C; $\Phi_{Tg}{}^{12}$= calculated porosity at Tg^{12}

[a]200 Mpa was used as P_{sv} due to bubbly starting material

[b]Experimental pressure was used as P_{sv} due to single capsule experiment

[c]Measured by FTIR spectroscopy using ϵ values from Schanofski et al. (2019)

[d]N.v. = no vaccum in the capsule; NQ= normal quenched. NL= iron phase nanolites detected by Raman analysis

[e]large error due to low ammount of released fluid during fluid determination

3.3.4 Sample names

In order to be able to quickly identify samples, this paragraph is meant to explain the systematics behind the sample names. The first letter resembles the dissolved volatile species (A) for H_2O, (B) for CO_2 and (C) for H_2O-CO_2 samples. The following number is unique to each starting material and is carried on to the decompression samples that use this starting material. Thereafter an underscore D200, D150, D100, D75, D50 or D30 resemble the final pressure after the decompression and can therefore only be found in decompression samples.

3.3.5 Fluid determination

The composition of a potential free fluid phase was determined after the decompression experiments by a weight-loss method. All capsules were initially weighted on a Cahn C-31 microbalance before freezing them in liquid nitrogen. The frozen capsules were pierced with a needle and kept in a nitrogen gas flux at -20 °C for 5 min (measured with a K-Type thermocouple) to release gaseous CO_2, while water remained in the frozen state. After letting the capsules heat to room temperature, they were re-weighted to measure the released CO_2. The capsules were stored in a desiccator at 35 °C overnight to evaporate the water prior to weighing them again to detect released H_2O. This rather low temperature treatment to release water was necessary to prevent bursting of fluid filled bubbles, which would result in erroneous fluid composition. This phenomenon was already observed and discussed by Schanofski et al. (2019) $X^{fl}_{H_2O}$ and amount of released fluid for all experimental decompression samples with a free fluid phase is reported in Table 3.3.

3.3.6 Infrared spectroscopy

H_2O and CO_2 contents in all experimental glasses were determined via FTIR spectroscopy using doubly polished thin sections. Transmission spectra were collected with a Bruker Hyperion 3000 IR microscope attached to a Bruker Vertex 70 FTIR spectrometer. Near-infrared (NIR) spectra in the range of 2000 - 6000 cm^{-1} were used to quantify the water content of the glasses using the peak at 4500 cm^{-1}, which is due to the vibration of structurally bonded hydroxyl groups and the peak at 5200 cm^{-1} resulting from a combination of stretching and bending modes of H_2O molecules (Scholze

1960). Mid-infrared (MIR) spectra ranging between 600 and 4000 cm^{-1} were collected to quantify CO_2 contents of the glasses using the carbonate bands between 1300 and 1600 cm^{-1}. A tungsten lamp was used in combination with a CaF_2 beam splitter for NIR spectra, while MIR spectra were collected with a Globar light source and a KBr beam splitter. For both techniques a liquid N_2 cooled MCT detector (range 600 - 12000 cm^{-1}) was used and each spectrum consisted of 32 accumulated scans with a spectral resolution of 4 cm^{-1}. A rectangular focus area of about 50 x 20 µm defined by rectangular aperture blades was used for both NIR and MIR spectra. The Lambert-Beer law was used as a basis to quantify the volatile concentration (c_i) by relating them to the baseline-corrected absorbance (A_i):

$$c_\mathrm{i} = \frac{M_\mathrm{i} A_\mathrm{i}}{d \epsilon_\mathrm{i} \rho}, \tag{3.1}$$

where c_i is the weight fraction of the volatile in %, Mi is the molar mass of the volatile molecule, d is the thickness of the doubly polished sample in cm, ϵ_i is the linear molar absorption coefficient in l mol^{-1} cm^{-1} and ρ is the density of the glass in g l^{-1} Sample thickness was determined using a Mitutoyo digital micrometer (3 µm accuracy) and was typically between 90 and 170 µm. The applied linear molar absorption coefficients were taken from Schanofski et al. (2019). Since the experimental glasses contain bubbles in most cases, the density of the glasses could not be measured. Instead the density was calculated using the method of Schmidt et al. (2013), correlating the density of hydrous samples from Schanofski et al. (2019) to the thickness normalized, baseline corrected peak heights of the 4500 cm^{-1} and 5200 cm^{-1} bands of the NIR spectra (see electronic Annex Fig A3.1 and A3.2).

3.3.7 Image analysis

All decompressed experimental samples were cut parallel to the longest axis of the capsule twice using a Well 3242 precision diamond wire saw with a 0.13 µm thick wire. This saw was used to minimize the loss of sample material during cutting and most importantly to ensure that fragile glass structures (e.g. melt films between bubbles) stay intact. The obtained sample slice was doubly polished for FTIR analysis while half of the remaining capsule was embedded in Crystalbond thermoplast and polished for taking high resolution pictures. In an early stage of this study we took secondary

electron (SE) pictures using a scanning electron microscope (SEM) and stitched the picture tiles together manually. This technique requires a time intensive preparation. Furthermore the resulting pictures suffered from distortion due to the small magnification used, complicating the stitching process. To overcome this problem, we took pictures in reflected light with a Zeiss Axio Image M2M microscope with a 20x magnification objective with NA of 0.4 and a Zeiss AxioCam MRc5 microscope camera. After the first image the samples were polished down by 100 µm and a second picture was taken. Since this pictures showed very similar results in the majority of samples, we decided to polish down the samples by further 300 µm before taking the third and last picture of each sample. We decided to take pictures from three sample intersections to improve the statistics of porosity and vesicle number density (VND) measurements. The picture tiles were stitched together automatically resulting in sample pictures of 1 – 2 µm/pixel average resolution. To obtain a perfect contrast between bubbles and the glass matrix, the entire capsule was redrawn on a separate layer using a drawing app Sketchbook. Figure 3.1 shows an example of a stitched microscope picture and the manually drawn sketch of the sample.

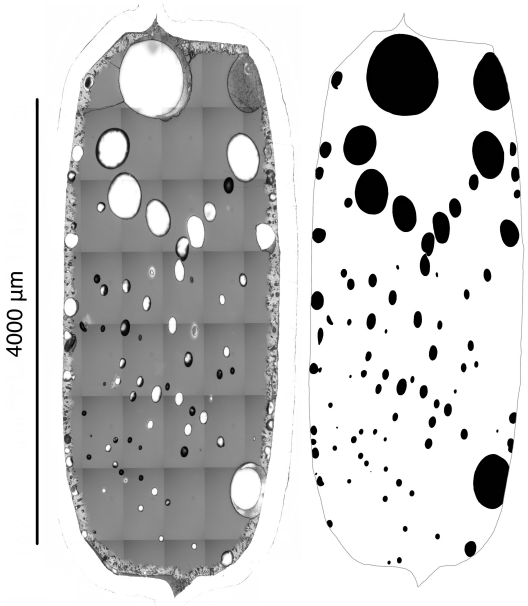

Figure 3.1: Automatically stitched reflection microscope picture of the sample C10_D50 on the left and manually repainted image of the same sample using SketchBook on the right. The glass in this particular case shows a slim crystallized rim in the contact with the capsule wall.

The program ImageJ (Higgins 2000) was used to quantitatively analyze the images. Three pictures were analyzed from different slices of the sample. Marxer et al. (2015) demonstrated that a minimum of 200 vesicle intersections are required to measure porosities with a sufficient reproducibility. In some cases (A11_D200, A9_D50, B18_D200,

B16_D150, C18_D200, C17_D150, C10_D30) this was not possible due to a lack of bubbles being present. Average values for porosity and vesicle number density (VND) were calculated to minimize the error of cutting effects and bubble shapes.

3.4 Results

3.4.1 Starting materials

The volatilized starting materials were mostly bubble- and crystal free. Samples equilibrated with a pure CO_2 fluid or a mixture of H_2O and CO_2 showed a minor amount of bubbles even after $\sim$ 90 h of experimental duration. Due to long diffusion times of the volatiles, in particular for CO_2, the use of bubble free, dry glass cylinders as starting material for the volatilization experiments was not an option. To tackle this problem, we used a combination of glass particles of $\sim$ 2 mm diameter and powder of multiple grain sizes in order to minimize pore space. Despite this careful preparation a minor amount of bubbles was present in some volatilized starting materials of the pure CO_2 and mixed H_2O and CO_2 series (see Table 3.2).

3.4.2 Volatile contents

Tables 3.2 and 3.3 show the volatile contents of the experimental starting materials and the decompressed samples, respectively. All starting materials are slightly undersaturated in volatile content compared to the 200 MPa equilibrium solubility data of Schanofski et al. (2019). After decompression the H_2O and/or CO_2 content is decreasing with increasing ΔP in all sample series, but never reaching the solubility. Figure 3.2 shows the CO_2 vs. H_2O concentration in the decompressed sample glasses, illustrating the degassing path for glasses with different volatile compositions. The degassing path of the H_2O-CO_2 sample series shows that CO_2 degasses at $P_f < 150$ MPa, whereas H_2O exsolution starts at $P_f < 76$ MPa.

3.4.3 Textural results

Repainted images of one representative intersection per sample are provided in Fig. 3.3. Each row shows one sample set. The final pressure decreases from left to right in each sample set.

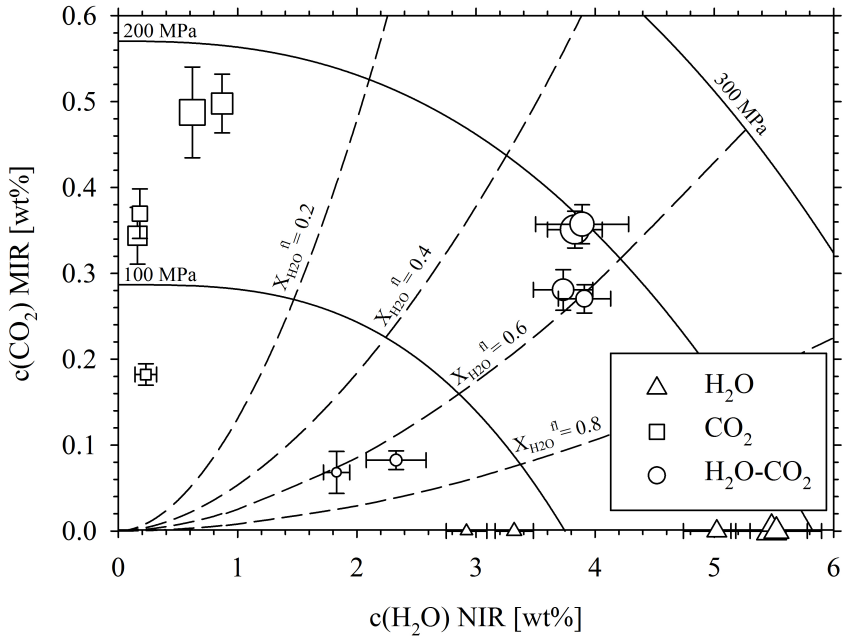

Figure 3.2: Concentration of CO_2 versus H_2O concentration in the decompression sample glasses for the H_2O, CO_2 and H_2O-CO_2 sample series. Solid lines show isobars from Schanofski et al. (2019) and represent the maximum solubility at a constant pressure with a varying fluid phase. Dashed lines are Isopleths from Schanofski et al. (2019) representing the solubility of a fixed H_2O-CO_2 fluid mixture at a range of pressure. Symbol size decreases with decreasing P_f of about 200, 150, 100, 50, 30 MPa. Note that for the mixed H_2O-CO_2Seies an extra experiment was performed with P_f= 76 MPa

In the pure H_2O sample series (first row capsules in Fig. 3.3), hardly any bubbles can be detected in the sample A11_D200 with a P_f= 204 MPa. In contrast, the sample A_D150 (P_f= 150 MPa) shows heterogeneous nucleation of bubbles close to the the capsule wall. A significant amount of bubbles is present in samples with $P_f \leq 100$ MPa. The sample A10_D100 with a P_f of 101 MPa shows nucleation of heterogeneous, spherical shaped bubbles along the capsule wall. The center of the sample is bubble free. A9_D50 with a P_f= 57 MPa shows fewer but larger bubbles that increase in size towards the top of the capsule and become more complex in shape, while A_D30 with P_f= 40 MPa shows even bigger bubbles all over the sample with a complex bubble network being formed that is close to an open porosity.

In the pure CO_2 sample series (second row capsules in Fig. 3.3) the sample B18_D200 with a P_f of 204 MPa is bubble free, except for few bubbles at the contact with the capsule wall that might either be nucleated during decompression or are pre-existing bubbles filled mostly with atmosphere due to insufficient vacuum in the capsule prior to the experiment. In contrast to the H_2O series, the sample B16_D150 (P_f= 150 MPa) shows no vesicle nucleation and just like B18_D200 a negligible amount of heterogeneously formed bubbles. In the sample B6_D100 (P_f= 102 MPa) homogeneous nucleation of bubbles takes place. In contrast to the water-bearing counterpart of this sample CO_2 bubbles show less heterogeneous nucleation at the capsule wall and predominantly nucleate homogeneously. Sample B6_D50 (P_f= 54 MPa) shows few bigger bubbles at the capsule walls as well as numerous smaller bubbles that concentrate towards the top of the sample. This evolution is carried on in sample B6_D30 with a P_f of 33 MPa, showing small bubbles only in the top half of the capsule and few large bubbles located at the contact with the capsule wall.

The sample series containing H_2O as well as CO_2 (third row capsules in Fig. 3.3) shows hardly any bubbles in the sample C18_D200 (P_f= 205 MPa). It has to be mentioned that a larger part in the top left corner of this sample was interpreted as a broke off piece of glass, which could also be interpreted as a large heterogeneous bubble due to its shape. C17_D150 with a P_f of 150 MPa shows hardly any bubbles as well. First bubble formation can be observed in the sample C10_D100 with a P_f of 102 MPa close to the capsule wall whilst showing a bubble free sample core. C17_D75 (P_f= 76 MPa) shows a very similar picture with a bubble free central portion and some bubbles at the capsule wall (pictures of this sample can only be found in Fig A3.3 in the electronic Annex). The sample C10_D50 (P_f= 54 MPa) shows a homogeneous distribution of bubbles across the entire capsule that increase in size towards the top of the capsule. This evolution is continued in sample C10_D30 (P_f= 33 MPa) that shows only few but big bubbles located at the capsule walls towards the top and few smaller bubbles in the lower portion of the sample. Due to the failed rapid quench the samples C10_D50 and C10_D30 show quench crystallization at the contact with the capsule wall. Images and repainted sketches of all decompressed sample sections can be found in the electronic Annex (Fig A3.3).

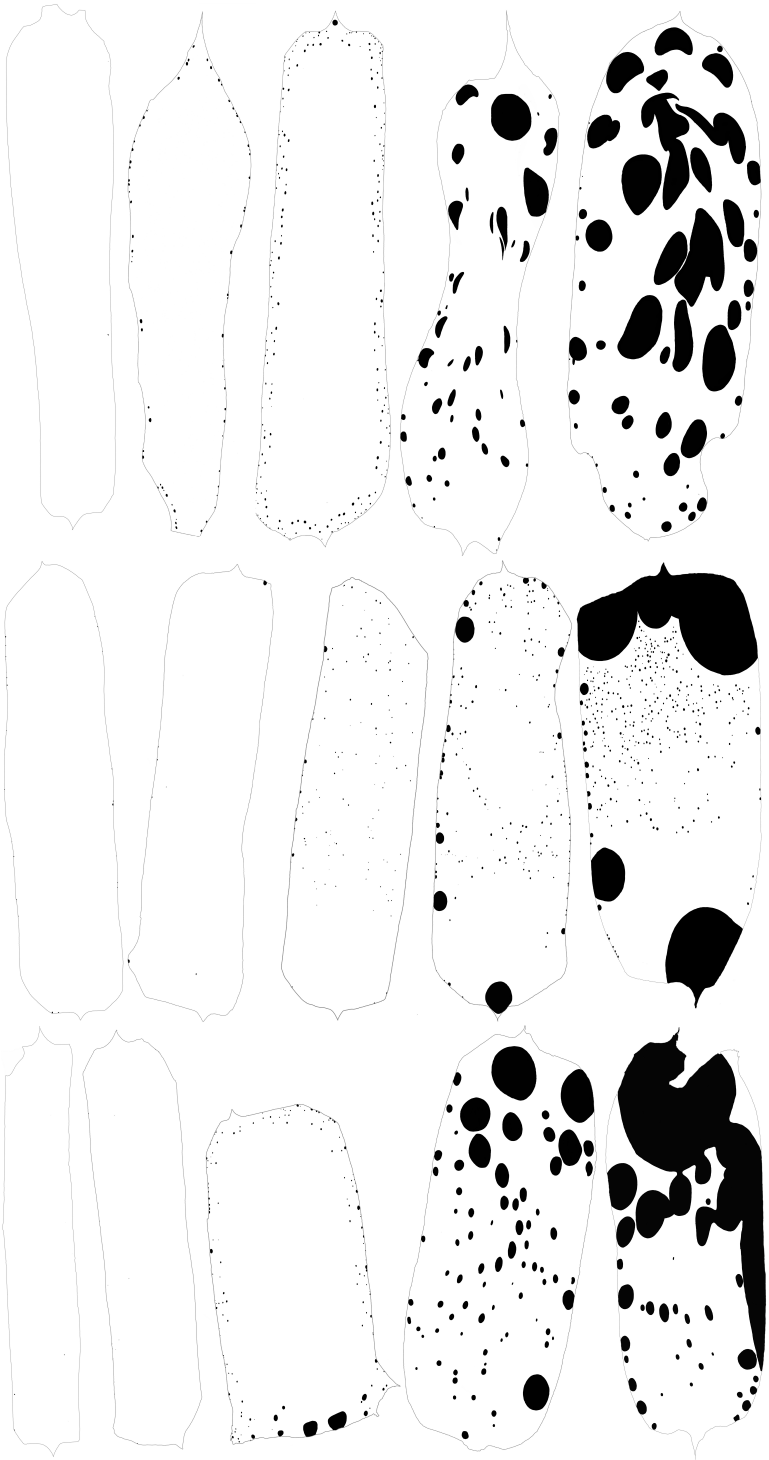

Figure 3.3: Repainted images of one representative section for each decompression sample. First row shows H_2O sample series, second row shows CO_2 sample series and third row shows H_2O-CO_2 sample series. Final Pressure (P_f) is decreasing from left to right in each row from about 200 over 150, 100 and 50 to 30 MPa.

3.5 Discussion

3.5.1 Measured and theoretical porosity

Values for measured (Φ_m) and modeled porosities (Φ_{equ} and $\Phi_{\mathrm{Tg}}{}^{12}$) of all sample series can be found in Table 3.3. Φ_m was calculated as a mean value of 2D porosities from three polished sample sections and the error propagation of their 2σ error. The experimental data sets are compared to modeled porosities at different temperatures using the equation of Gardner et al. (1999) (Eq. 3.2)

$$\Phi = \frac{(\Sigma[\frac{\rho_{melt}}{m_i} V_m^i (c_i^{ini} - c_i^d)])}{(1 + \Sigma[\frac{\rho_{melt}}{m_i} V_m^i (c_i^{ini} - c_i^d)])}, \tag{3.2}$$

where m_i is the molar mass of the volatile species, V_m^i is the molar volume of the volatile species at the corresponding temperature, c_i^{ini} is the volatile content in the glass prior to decompression (volatile content of the starting material), c_i^d is the volatile content of the glass after the decompression and ρ_{melt} is the melt density at P_f. V_m^i was calculated with the EOS from Sterner & K. (1994). ρ_{melt} was calculated after Ochs & Lange (1999) (Eq. 3.3)

$$\rho_{melt} = \frac{m}{\Sigma x_i (V_{i,Tref} + \frac{\partial V_i}{\partial T}(T - T_{ref}) + \frac{\partial V_i}{\partial P}(P - P_{ref}))}, \tag{3.3}$$

where x_i is the mole fraction of each component, $V_{i,Tref}$ is the partial molar volume of each component at a reference temperature , $\frac{\partial V_i}{\partial T}$ is the thermal expansivity of each component, Tref is a reference temperature and we used 1673 K for melt density calculations at experimental temperature and 1023 K for calculations at Tg^{12}, $\frac{\partial V_i}{\partial P}$ is the partial molar compressibility and P_{ref} is 1 bar. Values for partial molar volumes, thermal expansivity and partial molar compressibility are taken from Ochs & Lange (1997).

The porosity was calculated for the experimental temperature of 1250 °C. Even though it is known for some time that the volatile bubbles are shrinking during quench (Hurwitz & Navon 1994) this represents the maximum porosity to be expected in the experimental glasses. EOS-bubble shrinkage stops as soon as the melt is unable flow as a reaction to the volume decrease of the volatiles. Here we assume that the melt is able to compensate for the bubble shrinkage until the glass transition temperature (Tg^{12}). Tg^{12} is related to a fixed viscosity calculated for each sample with respect to its glass H_2O

content on basis of the model of Giordano et al. (2008). Kleest et al. (2020) measured the viscosity of the Pozzolane Rosse composition showing that it is one order of magnitude higher than predicted by Giordano et al. (2008). We corrected for these findings by calculating melt density at Tg^{11} using the model of Giordano et al. (2008) and using them as Tg^{12} values. These are 440 - 490 °C, 590 - 640 °C and 470 - 520 °C for the H_2O, CO_2 and H_2O-CO_2 sample series respectively.

Viscosity of the melt at constant temperature is lowered by H_2O and this effect is increasing with decreasing temperature (e.g., Shaw 1963). Melts with higher water contents can therefore react to the volume change of a gas phase more quickly and up to lower temperatures.

In Fig. 3.4 P_f is plotted against Φ_m for all decompression samples. The solid line in each plot resembles the regression of the modeled porosity for each sample at experimental temperature of 1250 °C (Φ_{equ}). The dashed line is the regression of the modeled porosity for each sample at Tg^{12} ($\Phi_{Tg}{}^{12}$) with respect to the H_2O contents of the decompressed melts. $\Phi_{Tg}{}^{12}$ represents the minimum porosity that one can expect in the samples, whereas Φ_{equ} represents the highest plausible porosity. The porosity calculated from the sample section pictures fit the theoretical porosity range very well. This is proof for a working porosity measurement technique, capable of detecting all bubbles from the core of the sample to the contact of the glass with the capsule material.

Recently Marxer et al. (2015) and Allabar et al. (2020) investigated the phenomenon of vesicle shrinkage during quench in decompression experiments of hydrous phonolitic melts. The shrinking of H_2O bubbles is a result of the decreasing molar volume of H_2O (V_{mH2O}) and H_2O resorption into the melt, due to an increase in water solubility, with decreasing temperature. If no bubble shrinkage occurred in our sample series, all measured porosities should be in line with the modeled porosities for 1250 °C. We find significantly lower porosities in all hydrous samples. If vesicle shrinkage due to a decrease in V_{mH2O} works until Tg^{12} with respect to the water content of the sample, $\Phi_{Tg}{}^{12}$ should be the porosity we measure in our experimental glasses. While Φ_m matches $\Phi_{Tg}{}^{12}$ much better than Φ_{equ} for both datasets, the samples C10_D50 and

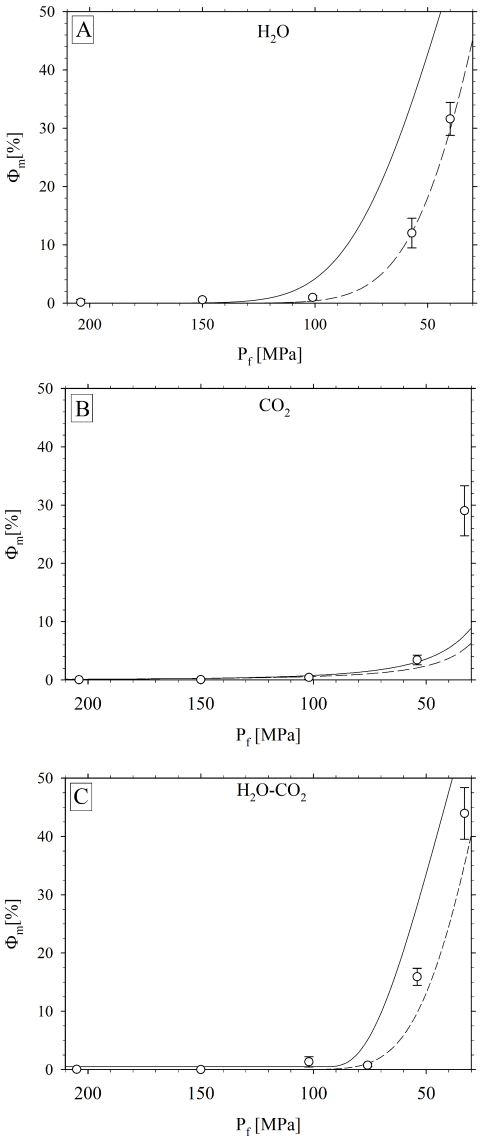

Figure 3.4: Measured porosity was plotted against final pressure for the H_2O (**A**), CO_2 (**B**) and H_2O-CO_2 (**C**) sample series. Error bars represent 2σ errors of porosity measurements of three sample intersections. Solid lines show regressions of modeled porosity data at 1250 °C (Φ_{equ}). Dashed lines represent regressions of modeled porosities at Tg^{12} ($\Phi_{Tg}{}^{12}$). Theoretical porosities were modeled with the method of Gardner et al. (1999).

C10_D30 show higher porosities than expected. We suggest that elevated porosities with respect to $\Phi_{Tg}{}^{12}$ in the CO_2 series and the samples C10_D50 and C10_D30 are due to an increased viscosity of the melt and can be explained by the following reasons.

[1] The samples mentioned above degassed substantially (2.33 and 1.83 wt% compared to 3.86 wt% prior to decompression). Melts poor in H_2O have a significantly higher viscosity at similar temperatures. Therefore, melts with a low H_2O content are not able to respond to volume changes of the gas phase as quick as water rich melts during a rapid quench of 150 K/s.

[2] The presence of iron phase nanolites was verified in the samples C10_D50 and C10_D30 that show the larges deviation of $\Phi_m > \Phi_{Tg}{}^{12}$ (up to 10 vol%) by a 670 cm^{-1} Raman band. Even though the raman spectra do not allow for any quantification Di Genova et al. (2020) have shown that even small vol% of nanolites in silicate melts are capable of increasing the viscosity, leading to a viscosity of Tg^{12} at higher temperatures than predicted by the model of Giordano et al. (2008).

There is one outlier that ought to be mentioned. The porosity of the sample B6_D30 (29 %) is almost three times higher than expected (Fig. 3.4b). However the amount of released fluid phase after piercing of the capsule is unusually high (0.85 mg). Calculating the porosity on the basis of the amount of released CO_2 fluid results in a Φ_{equ} of 19.17 % already showing a much higher value than the 7.8 % calculated from glass volatile contents. Taking the samples closed porosity into account (Fig 3.3 and Annex Fig A3.3), at least some of the fluid did not escape during piercing which also points into the direction of a much higher porosity due to high CO_2 contents. Since the volatilized starting material for this experiment did not have a sufficient volatile content to explain this, the most reasonable explanation would be contamination with some organic matter (e.g. skin particles, fiber of paper tissue) during preparation of the B6_D30 capsule as the vesicles are indeed filled with CO_2, measured by Raman spectroscopy.

3.5.2 Supersaturation pressure and ΔP

In order to calculate the supersaturation pressure (P_{ss}) we fitted the pure H_2O/CO_2 solubility data from Schanofski et al. (2019) (see Fig. 3.5).

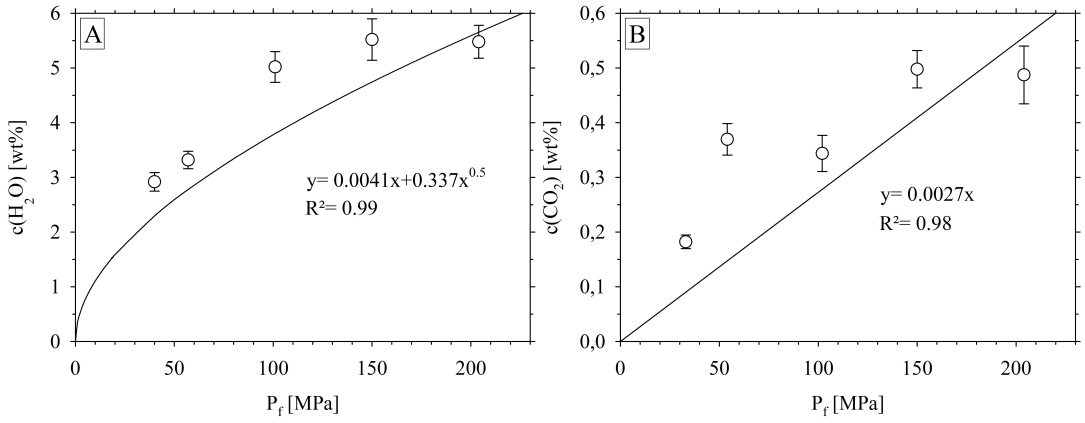

Figure 3.5: Volatile content of the decompressed glasses of H_2O (**A**) and CO_2 (**B**) sample series respectively is plotted against P_f (final pressure). Regressions represent the maximum solubility at given pressure and was calculated using data from Schanofski et al. (2019). Regressions were used for the calculation of P_{sv} (volatile saturation pressure of starting glasses) and P_{sd} (volatile saturation pressure of decompressed glasses).

Resulting regressions gave values for the volatile saturation pressure for a single volatile

species in volatile bearing starting materials (P_{sv}) and decompressed glasses (P_{sd}). Using the equation

$$P_{ss} = P_{sd} - P_f, \tag{3.4}$$

supersaturation pressure (P_{ss}) was calculated. For samples with a mixed H_2O-CO_2 fluid we fitted a paraboloidic regression surface shown in Fig. 3.6 to all the solubility data from Schanofski et al. (2019). Using the regression equation

$$P = 24 - 5.83 * c_{H2O} + 245 * c_{CO2} + 6.3 * (c_{H2O})^2 + 116 * (c_{CO2})^2, \tag{3.5}$$

with c_{H2O} and c_{CO2} given in wt%, values for P_{sv} and P_{sd} could be derived for melts in equilibrium with a mixed H_2O-CO_2 fluid.

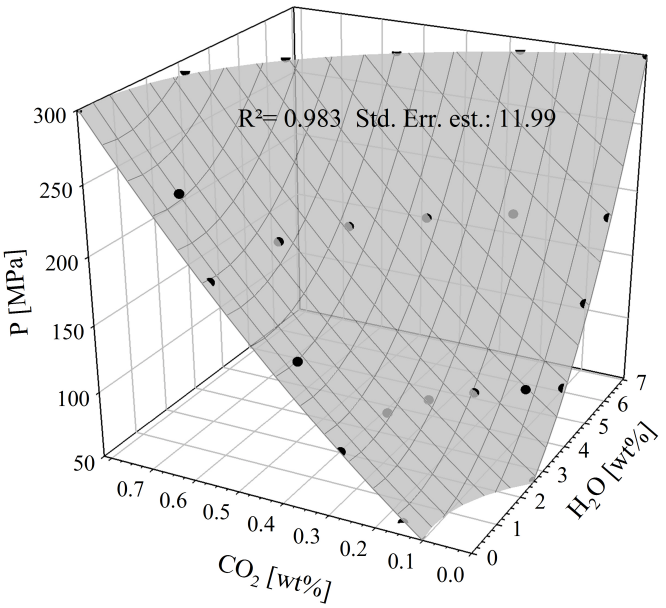

Figure 3.6: Solubility of H_2O and CO_2 at a pressure between 50 and 300 MPa using the solubility data of Schanofski et al. (2019). Grey surface shows paraboloidic regression following Equation 3.5. Regression was used for calculating P_{sv} (volatile saturation pressure of starting glasses) and P_{sd} (volatile saturation pressure of decompressed glasses) for the H_2O-CO_2 sample series.

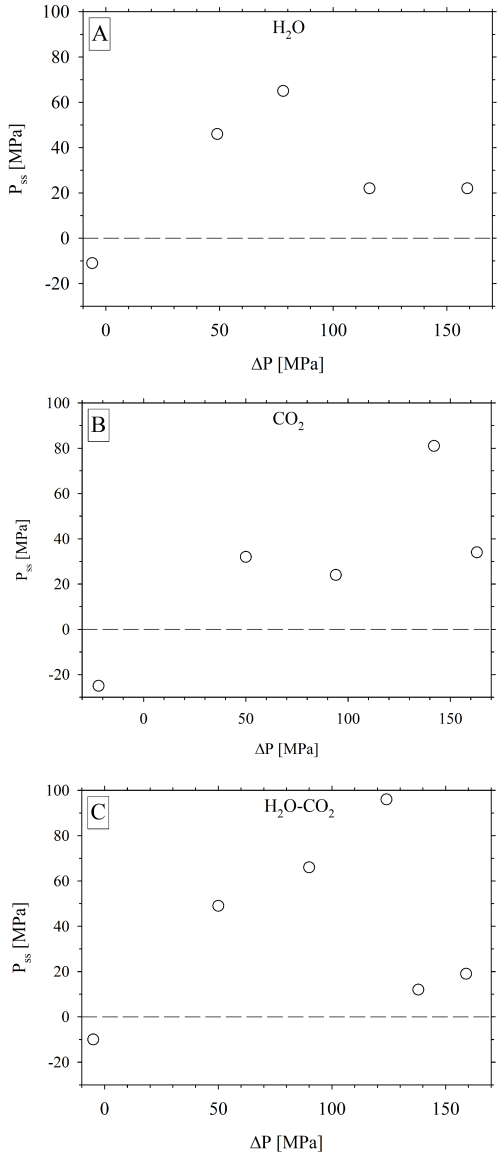

Figure 3.7: Supersaturation Pressure for the H_2O (**A**) CO_2 (**B**) and H_2O-CO_2 (**C**) sample series was plotted against ΔP. The dashed line in each plot resembles the saturation pressure (P_{sd}) for each decompression experiment. ΔP is the difference between P_f and P_{sv}.

P_{sv} values were used to calculate ΔP for each decompression experiment following the equation:

$$\Delta P = P_{sv} - P_f, \tag{3.6}$$

Note that samples A_D150 and A_D30 were synthesized and decompressed in one single experiment. Therefore, no P_{sv} could be calculated and the equilibration pressure prior to the decompression (199 MPa) was used instead. Samples B16_D150, C18_D200 and C17_D150 were prepared from a vesiculated starting material. The measured volatile content in the starting glass was therefore lower than the total volatile budget in the decompression experiment. Volatiles contained in these bubbles were dissolved in the equilibration time of the decompression experiments at 200 MPa over 4 days. As a result the volatile content of the decompressed samples is higher than in the volatilized starting materials. To calculate ΔP, 200 MPa of the four day equilibration step prior to decompression was used as replacement for P_{sv}.

P_{ss} vs. ΔP for all sample series is illustrated in Fig. 3.7. Reference samples for each volatile series (leftmost data point in each plot) show a negative P_{ss} due to the fact that the volatile content of their starting material is lower than the solubility at the

experimental pressure of 200 MPa. The H_2O series (Fig. 3.7a) shows an increasing supersaturation pressure with increasing ΔP and reaches its maximum P_{ss} of 65 MPa at a ΔP of 78 MPa before rapidly decreasing to 22 MPa for experiments with a higher ΔP.

The increase in P_{ss} with ΔP in the CO_2 series (Fig. 3.7b) is interrupted by a minor decline from 32 to 24 MPa going from a ΔP of 50 to 94 MPa before reaching its maximum of 81 MPa at a ΔP of 142 MPa. At a ΔP of 163 the P_{ss} decreases significantly to a value of 34 MPa. Apparently P_{ss} was lowered by the first bubbles that nucleated homogeneously in the sample B6_D100.

P_{ss} in the H_2O-CO_2 series (Fig. 3.7c) increases monotonously to the highest P_{ss} of 96 MPa at a ΔP of 124 MPa. At ΔP of 138 MPa the P_{ss} decreases to 12 MPa before increasing to 19 MPa at a ΔP of 159 MPa. The P_{ss} trend for the H_2O-CO_2 sample series is mainly controlled by H_2O. Glass H_2O contents show that the original H_2O content of the melt is preserved up to a ΔP of 124 MPa, constantly increasing P_{ss}. At higher ΔP exsolution of H_2O takes place resulting in a strong decrease in P_{ss}.

3.5.3 Vesicle number density

Vesicle number density (VND) is the average number of vesicles per cubic millimeter and sheds light on the onset of nucleation (by increasing VND) and coalescence (by decreasing VND). The value of VND is calculated on the basis of the textural information of the entire sample. The program ImageJ 1.52a records the size and total amount of bubbles in the sample as well as the total area of the sample. This information is used by the program CSDCorrections 1.6 (Higgins 2000) to calculate VND values for each sample section. Average VND values for each sample were normalized to a vesicle free glass volume after Marxer et al. (2015) (equation 2) in order to obtain values independent of bubble growth using the equation

$$VND_n = \frac{VND}{1 - \Phi_m}, \tag{3.7}$$

where VND_n is the normalized number of bubbles in mm^{-3}, VND is the average vesicle number density of 3 measurements from different sections in mm^{-3} and Φ_m is the

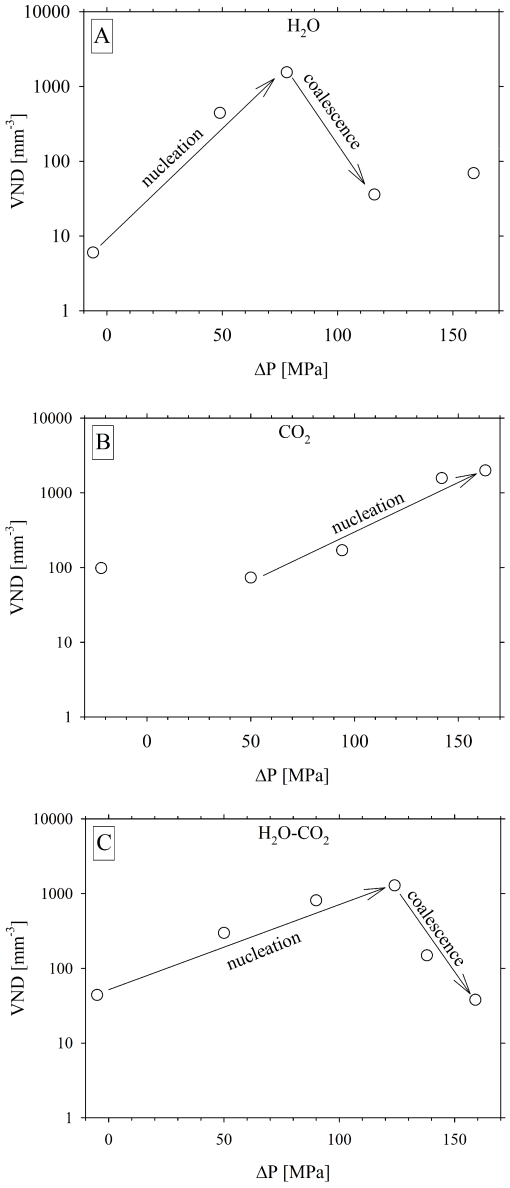

Figure 3.8: Plot of the VND_n (normalized vesicle number density) for the H_2O (**A**) CO_2 (**B**) and H_2O-CO_2 (**C**) sample series at given ΔP. ΔP is the difference between P_f and P_{sv}.

measured porosity. In Fig. 3.8 the normalized average VND_n is plotted against ΔP for all sample series.

The VND_n in the H_2O sample series (Fig. 3.8a) increases from 6 mm^{-3} in the reference sample to its peak at 1548 mm^{-3} in the sample A10_D100 with a ΔP of 78 MPa indicating a nucleation event. At higher ΔP values coalescence is taking place as VND_n values decrease to 36 mm^{-3}.

In the CO_2 series (Fig. 3.8b) nucleation of bubbles starts at a ΔP of 94 MPa. In contrast to the H_2O series the nucleation of CO_2 bubbles is a continuous process as indicated by an increase in VND_n up to 1991 mm^{-3} in the sample B6_D30 with a ΔP of 163 MPa. Additionally, growth and coalescence of bubbles can be observed in the samples B6_D50 and B6_D30. We propose that the observation of continuous nucleation is due to the slow diffusion speed of CO_2 which is not allowing for migration into bubbles further away at the given decompression speed of 1 MPa/s to decrease CO_2 supersaturation.

Similar to the H_2O series, nucleation begins at ΔP values below 50 MPa in the H_2O-CO_2 sample series (Fig. 3.8c). The formation of new bubbles is carried on up to a

ΔP value of 124 MPa reaching a maximum of 1286 mm^{-3}. At higher ΔP the VND$_n$ decreases monotonously to 38 mm^{-3} indicating a coalescence dominated system.

3.5.4 Homogeneous bubble nucleation

Homogeneous bubble nucleation occurs between the last sample that does not show a volume filling bubble population and the first sample that does. Since this describes a pressure interval, the ΔP at which homogeneous nucleation takes place (ΔP_{HON}) can only be given as a pressure range. From visual observation, homogeneous bubble nucleation occurs at ΔP_{HON} values of 78 -116 MPa, 50 - 94 MPa and 124 - 138 MPa in the H_2O, CO_2 and H_2O-CO_2 samples series respectively. It has to be stated at this point, that it may seem as if higher ΔP values were required for homogeneous bubble nucleation in the H_2O-CO_2 series then in the H_2O series. This is no valid observation since the H_2O-CO_2 sample series has an extra experiment with P_f of 76 MPa narrowing down the ΔP range. the samples we consider showing first homogeneous nucleation from visual examination, already show fairly large bubbles in the H_2O and H_2O-CO_2 sample series. We therefore suspect, that the real ΔP_{HON} is towards the lower end of the given pressure ranges.

Mourtada-Bonnefoi & Laporte (2002) found that rhyolitic melts show a larger ΔP_{HON} when containing high amounts of CO_2 (above 800 ppm). As pointed out by Shea (2017): *"it is unknown up to this point whether the changes in vesicle nucleation behavior in H_2O-CO_2 bearing melts are driven by CO_2 itself or by the undersaturated nature of the melt with respect to H_2O."*

To tackle this point, we evaluated the effect of CO_2 on H_2O exsolution by calculating the volatile supersaturation (c_{ss}^{H2O}). Commonly a supersaturation pressure (P_{ss}) is calculated to express the volatile supersaturation. The advantage of expressing the supersaturation as a pressure is that one can easily compare data for H_2O, CO_2 and H_2O-CO_2 volatile systems. On the other hand, in mixed H_2O-CO_2 systems P_{ss} does not show the contribution of each volatile phase to the supersaturation pressure and might even be misleading due to the fact that H_2O solubility as a function of pressure describes a non-linear behavior in contrast to CO_2. C_{ss}^{H2O} was calculated using the equation

$$c_{ss}^{H2O} = c_d^{H2O} - c_s^{H2O}, \tag{3.8}$$

where c_{ss}^{H2O} is the volatile supersaturation in wt%, c_d^{H2O} is the H_2O content of the decompression samples in wt% and c_s^{H2O} is the H_2O solubility at P_f in wt% from Schanofski et al. (2019).

This calculation is quite complex since c_s^{H2O} depends on X_{H2O}^{fl} at P_f. In contrast to the H_2O sample series (where X_{H2O}^{fl}= 1 for all samples) X_{H2O}^{fl} of the H_2O-CO_2 sample series is constantly changing during degassing from about 0.5 towards 1 assuming a closed system equilibrium degassing. We used the VolatileCalc model of Newman & Lowenstern (2002) to calculate X_{H2O}^{fl} at P_f using the following parameters: SiO_2= 44 wt%; c_{H2O}=3.85 wt%; c_{CO2}= 3500 ppm; T= 1250 °C; exsolved vapor= 0%; steps= 100.

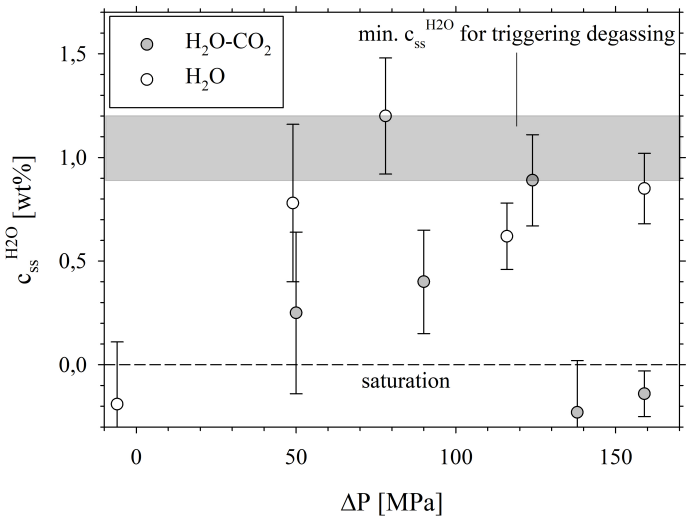

Figure 3.9: H_2O supersaturation in wt% is plotted against ΔP for the H_2O sample series (open symbols) and the H_2O-CO_2 sample series (grey symbols). Error bars are errors of c_d^{H2O} (water content of the glass after decompression experiments). Grey bar shows the c_{ss}^{H2O} required for homogeneous nucleation of H_2O bearing bubbles. Dashed line represents c_d^{H2O} (solubility of H_2O at P_f).

With X_{H2O}^{fl}, we could calculate c_{ss}^{H2O} for each decompression sample using the data from Schanofski et al. (2019). ΔP vs. c_{ss}^{H2O} is plotted in Fig. 3.9 for the H_2O and H_2O-CO_2 sample series. In the H_2O sample series, the volatile supersaturation is increasing with

ΔP until the minimum c_{ss}^{H2O} for triggering H_2O degassing is reached (1.2 wt%) in the sample A10_D100. In the H_2O-CO_2 sample series c_{ss}^{H2O} prior to degassing is significantly lower at comparable ΔP values. The minimum c_{ss}^{H2O} for triggering H_2O degassing is reached (0.9 wt%) in the sample C17_D75. Even though the errors are overlapping, it can be seen, that in the presence of CO_2, the minimum H_2O supersaturation required for homogeneous bubble nucleation may be lower than in a pure H_2O system. We suspect that this decrease in supersaturation required for H_2O degassing is due to CO_2 degassing prior to H_2O in the H_2O-CO_2 samples as indicated by the volatile content of the glass after decompression experiment (see Table 3.3). The CO_2 vesicle population decreases surface tension and therefore the energy barrier that needs to be overcome for H_2O to degas.

3.6 Conclusions

We performed a wide range of continuous rapid decompression experiments for different fluid compositions showing the transition of bubble free over homogeneously nucleated to coalescence and migration dominated samples. From these experiments the following conclusions can be derived:

[1] The nucleation of H_2O volatile bubbles from a mafic (here leucititic) melt in our experiments is strongly different from CO_2 bubble nucleation. The H_2O fluid shows a single nucleation event pared with lower vesicle number densities (up to 1548 mm^{-3} vs 1991 mm^{-3}) and higher overall porosities. CO_2 can create much higher supersaturation pressures of at least 81 MPa compared to 65 MPa for H_2O and continuously nucleates new bubbles due to the slow diffusion speed of CO_2 requiring for more bubbles in close proximation to degas. These findings overlap with experiments of Le Gall & Pichavant (2016) showing a single nucleation event for H_2O bearing basaltic melts, while CO_2 bearing basaltic melts show multiple nucleation pulses over a large range of P_f.

[2] H_2O-CO_2 bearing melts degas CO_2 exclusively below ΔP of 139 MPa resulting in the highest P_{ss} of 96 MPa. At higher ΔP H_2O exsolution starts, resulting in a dramatic increase in porosity and decrease in supersaturation. This is in line with observations of Blundy et al. (2010) and classical degassing models (e.g., Dixon & Stolper 1995).

Additionally, mixed H_2O-CO_2 fluid results in the highest porosity of 44% measured at a ΔP of 159.

[3] Modelled porosities for 1250 °C and Tg^{12} show a good fit to the experimental data supporting the technique used for measuring porosity. While H_2O bearing glasses tend to freeze in a situation close to Tg^{12}, pure CO_2 bearing melts show porosities better fitting to modelled values for experimental temperature of 1250 °C.

[4] At slower cooling rates, iron phase nanolites were detected in the H_2O-CO_2 bearing glasses C10_D50 and C10_D30. Experiments of Di Genova et al. (2020) demonstrated the effect of $\leq$ 3 vol% nanoparticles on silicate melts by increasing the viscosity by orders of magnitude. These findings might explain the relatively high porosities preserved in the nanolite bearing samples.

[5] Due to the low viscosity of the SULm composition samples of higher ΔP values show migration and coalescence of bubbles to different degrees regardless of the fast decompression speed of 1 MPa/s and the rapid quench with $\sim$ 150 °C/s.

[6] Future experimental decompression studies should also take CO_2 as the second most abundant volatile species in volcanic degassing systems into account as it can have a large effect on the degassing behavior.

References

Allabar, A., Dobson, K. J., Bauer, C. C., & Nowak, M. (2020). Vesicle shrinkage in hydrous phonolitic melt during cooling. *Contributions to Mineralogy and Petrology*, 175(21).

Allabar, A. & Nowak, M. (2018). Message in a bottle: Spontaneous phase separation of hydrous Vesuvius melt even at low decompression rates. *Earth and Planetary Science Letters*, 501, 192–201.

Benne, D. & Behrens, H. (2003). Water solubility in haplobasaltic melts. *European Journal of Mineralogy*, 15(5), 803–814.

Blundy, J., Cashman, K. V., Rust, A., & Witham, F. (2010). A case for CO_2-rich arc magmas. *Earth and Planetary Science Letters*, 290(3-4), 289–301.

Boettcher, S. & Buo, Q. (1989). A simple device for loading gases in high-pressure experiments. *American Mineralogist*, (pp. 1383–1384).

Buono, G., Fanara, S., Macedonio, G., Palladino, D., Petrosino, P., Sottili, G., & Pappalardo, L. (2020a). Dynamics of degassing in evolved alkaline magmas: Petrological, experimental and theoretical insights. *Earth Science Reviews*, 211, 103402.

Buono, G., Pappalardo, L., Harris, C., Edwards, B. R., & Petrosino, P. (2020b). Magmatic stoping during the caldera-forming Pomici di Base eruption (Somma-Vesuvius, Italy) as a fuel of eruption explosivity. *Lithos*, 370-371, 105628.

Cashman, K. V. & Mangan, M. T. (1994). Chapter 11b. PHYSICAL ASPECTS OF MAGMATIC DEGASSING II. Constraints on vesiculation processes from textural studies of eruptive products. In M. R. Carroll, J. R. Holloway, M. R. Carroll, & J. R. Holloway (Eds.), *Volatiles in Magmas* (pp. 447–478). Berlin, Boston: De Gruyter.

Cluzel, N., Laporte, D., Provost, A., & Kannewischer, I. (2008). Kinetics of heterogeneous bubble nucleation in rhyolitic melts: implications for the number density of bubbles in volcanic conduits and for pumice textures. *Contributions to Mineralogy and Petrology*, 156(6), 745–763.

Coumans, J. P., Llewellin, E. W., Wadsworth, F. B., Humphreys, M., Mathias, S. A., Yelverton, B. M., & Gardner, J. E. (2020). An experimentally validated numerical model for bubble growth in magma. *Journal of Volcanology and Geothermal Research*, 402, 107002.

Dallai, L., Freda, C., & Gaeta, M. (2004). Oxygen isotope geochemistry of pyroclastic clinopyroxene monitors carbonate contributions to Roman-type ultrapotassic magmas. *Contributions to Mineralogy and Petrology*, 148(2), 247–263.

Di Genova, D., Brooker, R. A., Mader, H. M., Drewitt, J. W. E., Longo, A., Deubener, J., Neuville, D. R., Fanara, S., Shebanova, O., Anzellini, S., Arzilli, F., Bamber, E. C., Hennet, L., La Spina, G., & Miyajima, N. (2020). In situ observation of nanolite growth in volcanic melt: A driving force for explosive eruptions. *Science advances*, 6(39).

Dixon, J. E. & Stolper, E. M. (1995). An Experimental Study of Water and Carbon Dioxide Solubilities in Mid-Ocean Ridge Basaltic Liquids. Part II: Applications to Degassing. *Journal of Petrology*, 36, 1633–1646.

REFERENCES

Fanara, S., Botcharnikov, R. E., Palladino, D. M., Adams, F., Buddensieck, J., Mulch, A., & Behrens, H. (2015). Volatiles in magmas related to the Campanian Ignimbrite eruption: Experiments vs. natural findings. *American Mineralogist*, 100(10), 2284–2297.

Freda, C., Gaeta, M., Giaccio, B., Marra, F., Palladino, D. M., Scarlato, P., & Sottili, G. (2011). CO_2-driven large mafic explosive eruptions: the Pozzolane Rosse case study from the Colli Albani Volcanic District (Italy). *Bulletin of Volcanology*, 73(3), 241–256.

Freda, C., Gaeta, M., Misiti, V., Mollo, S., Dolfi, D., & Scarlato, P. (2008). Magma–carbonate interaction: An experimental study on ultrapotassic rocks from Alban Hills (Central Italy). *Lithos*, 101(3-4), 397–415.

Gaeta, M., Freda, C., Christensen, J. N., Dallai, L., Marra, F., Karner, D. B., & Scarlato, P. (2006). Time-dependent geochemistry of clinopyroxene from the Alban Hills (Central Italy): Clues to the source and evolution of ultrapotassic magmas. *Lithos*, 86(3-4), 330–346.

Gardner, J. E., Hilton, M., & Carroll, M. R. (1999). Experimental constraints on degassing of magma: isothermal bubble growth during continuous decompression from high pressure. *Earth and Planetary Science Letters*, 168(1-2), 201–218.

Gardner, J. E. & Webster, J. D. (2016). The impact of dissolved CO_2 on bubble nucleation in water-poor rhyolite melts. *Chemical Geology*, 420, 180–185.

Giordano, D., Russell, J. K., & Dingwell, D. B. (2008). Viscosity of magmatic liquids: A model. *Earth and Planetary Science Letters*, 271(1-4), 123–134.

Gonnermann, H. M., Manga, M., & Fagents, S. A. (2013). *Dynamics of magma ascent in the volcanic conduit*, (pp. 55–84). Cambridge University Press: Cambridge.

Higgins, M. D. (2000). Measurement of crystal size distributions. *American Mineralogist*, 85(9), 1105–1116.

Holloway, Dixon, J. E., & Pawley, A. R. (1992). An internally heated, rapid-quench, high-pressure vessel. *American Mineralogist*, 77, 643–646.

Huber, C., Su, Y., Nguyen, C. T., Parmigiani, A., Gonnermann, H. M., & Dufek, J. (2014). A new bubble dynamics model to study bubble growth, deformation, and coalescence. *Journal of Geophysical Research: Solid Earth*, 119(1), 216–239.

Hurwitz, S. & Navon, O. (1994). Bubble nucleation in rhyolitic melts: Experiments at high pressure, temperature, and water content. *Earth and Planetary Science Letters*, 122(3-4), 267–280.

Iacono Marziano, G., Gaillard, F., & Pichavant, M. (2007). Limestone assimilation and the origin of CO_2 emissions at the Alban Hills (Central Italy): Constraints from experimental petrology. *Journal of Volcanology and Geothermal Research*, 166(2), 91–105.

Kleest, C., Webb, S. L., & Fanara, S. (2020). Rheology of melts from the colli albani volcanic district (Italy): a case study. *Contributions to Mineralogy and Petrology*, 175(9).

Le Gall, N. & Pichavant, M. (2016). Homogeneous bubble nucleation in H_2O- and H_2O-CO_2 -bearing basaltic melts: Results of high temperature decompression experiments. *Journal of Volcanology and Geothermal Research*, 327, 604–621.

Lesher, C. E. & Spera, F. J. (2015). *Thermodynamic and Transport Properties of Silicate Melts and Magma*, (pp. 113–141). Elsevier.

Marxer, H., Bellucci, P., & Nowak, M. (2015). Degassing of H_2O in a phonolitic melt: A closer look at decompression experiments. *Journal of Volcanology and Geothermal Research*, 297, 109–124.

Mourtada-Bonnefoi, C. C. & Laporte, D. (2002). Homogeneous bubble nucleation in rhyolitic magmas: An experimental study of the effect of H_2O and CO_2. *Journal of Geophysical Research: Solid Earth*, 107(B4), ECV 2–1–ECV 2–19.

Newman, S. & Lowenstern, J. B. (2002). VolatileCalc: a silicate melt–H_2O–CO_2 solution model written in Visual Basic for excel. *Computers & Geosciences*, 28(5), 597–604.

Ochs, F. & Lange, R. (1997). The partial molar volume, thermal expansivity, and compressibility of H_2O in $NaAlSi_3O_8$ liquid: new measurements and an internally consistent model. *Contributions to Mineralogy and Petrology*, (pp. 155–165).

Ochs, F. & Lange, R. (1999). The Density of Hydrous Magmatic Liquids. *Science (New York, N.Y.)*, 283(5406), 1314–1317.

Pappalardo, L., Buono, G., Fanara, S., & Petrosino, P. (2018). Combining textural and geochemical investigations to explore the dynamics of magma ascent during Plinian eruptions: a Somma–Vesuvius volcano (Italy) case study. *Contributions to Mineralogy and Petrology*, 173(7).

Roux, J. & Lefèvre, A. (1992). A fast-quench device for internally heated pressure vessels. *European Journal of Mineralogy*, 4(2), 279–282.

Rutherford, M. J. (2003). Magmatic Conditions and Magma Ascent as Indicated by Hornblende Phase Equilibria and Reactions in the 1995-2002 Soufriere Hills Magma. *Journal of Petrology*, 44(8), 1433–1453.

Schanofski, M., Fanara, S., & Schmidt, B. C. (2019). CO_2–H_2O solubility in K-rich phonolitic and leucititic melts. *Contributions to Mineralogy and Petrology*, 174(6).

Schmidt, B. C., Blum-Oeste, N., & Flagmeier, J. (2013). Water diffusion in phonolite melts. *Geochimica et Cosmochimica Acta*, 107, 220–230.

Shaw, H. R. (1963). Obsidian-H_2O viscosities at 1000 and 2000 bars in the temperature range 700 °C to 900 °C. *Journal of Geophysical Research: Solid Earth*, 68(23), 6337–6343.

Shea, T. (2017). Bubble nucleation in magmas: A dominantly heterogeneous process? *Journal of Volcanology and Geothermal Research*, 343, 155–170.

Simkin, T. & Siebert, L. (1994). *Volcanoes of the World*. Tucson AZ: Geoscience Press in association with the Smithsonian Institution Global.

Sparks, R. (1978). The dynamics of bubble formation and growth in magmas: A review and analysis. *Journal of Volcanology and Geothermal Research*, 3(1-2), 1–37.

Sparks, R., Baker, L., Brown, R. J., Field, M., Schumacher, J., Stripp, G., & Walters, A. (2006). Dynamical constraints on kimberlite volcanism. *Journal of Volcanology and Geothermal Research*, 155(1-2), 18–48.

Sparks, R., Barclay, J., Jaupart, C., Mader, H. M., & Philips, J. C. (1994). Physical aspects of magma degassing. *Rev. Mineral*, 30, 413–445.

Sterner, S. & K., P. S. (1994). An equation of state for carbon dioxide valid from zero to extreme pressures. *Contributions to Mineralogy and Petrology*, (pp. 362–374).

Toramaru, A. (1995). Numerical study of nucleation and growth of bubbles in viscous magmas. *Journal of Geophysical Research: Solid Earth*, 100(B2), 1913–1931.

REFERENCES

Wallace, P., Plank, T., Edmonds, M., & Hauri, E. (2015). *Volatiles in Magmas*, (pp. 163–183). Academic Press, London.

4

CO_2 quantification in silicate glasses using µ-ATR FTIR spectroscopy

Maximilian Schanofski[1], Burkhard C. Schmidt[1]

[1]Geowissenschaftliches Zentrum, Georg-August-Universität (GZG),
Goldschmidtstraße 1, 37077 Göttingen, Germany

4.1 Abstract

A new method for measurements of high CO_3^{2-} concentrations in silicate melts was established using a Attenuated Total Reflectance (µ-ATR) MIR setup connected to a Hyperion 3000 microscope and a Bruker Vertex 70 spectrometer. An absorption doublet at 1510 cm^{-1} and 1430 cm^{-1} respectively has shown to nicely separate from SiO_2 lattice vibrations at lower wavenumbers. Due to the lower sensitivity of this method, we were able to measure high CO_2 contents in experimental silicate melts that would not be measurable with established Transmission MIR measurements due to detector saturation even with thin samples of 100 µm thickness. A linear dependence of normalized peak heights to CO_2 contents measured by CSA has been verified and a linear correlation coefficient of k_{1430}= 2.28 ± 0.02 has been determined for a synthetic analogue of the leucititic eruptive material from the Pozzolane Rosse eruption of the Colli

Albani 456 ka ago.

Keywords: ATR-micro spectroscopy · ATR FTIR · silicate glasses · Carbon dioxide · CO_3^{2-} quantification · CO_2

4.2 Introduction

Besides water, carbon dioxide is the second most abundant volatile in volcanic systems. Silicate melts play a fundamental role in transporting carbon from the Earth's interior to its surface. However, CO_2 solubility is one to two orders of magnitude lower than the solubility of water under equivalent experimental conditions (Mysen et al. 1976).

Several analytical methods exist to quantify CO_2 concentration in silicate glasses. Pan et al. (1991), Thibault & Holloway (1994) and Behrens et al. (2004) used Secondary Ion Mass Spectroscopy (SIMS) to calculate the abundance of carbon in basaltic and leucititic melts. This technique uses an ion beam focused on the surface of the sample. The incoming ions spatter ionized atoms from the surface of the sample, which are collected and analysed by a mass spectrometer. The abundance of carbon is calculated from the empirical linear correlation between the count rates of ^{12}C normalized to those of ^{28}Si-, and the concentration of CO_2 in standards. This technique is dependent on an initial standardization using another technique. One of the most used complementary way to measure bulk CO_2 abundance is the Carbon-Sulfur Analyzer (CSA). The sample is combusted in a flowing oxygen stream to release all carbon in the form of CO_2. Its abundance is then determined by an infrared cell. CS-analysis is a widely used technique in experimental petrology for characterization of standards for other techniques. The measurement is a destructive but sensitive technique that requires a relatively high amount of material (approx. 5 - 50 mg depending on CO_2 concentration in the sample).

Morizet et al. (2013) established a method for quantification of CO_2 in geologically relevant glasses using confocal micro-Raman spectroscopy. They discovered a linear dependence of CO_2 concentration (bonded as CO_3^{2-}) on the full width half maximum (FWHM) of the carbonate vibrations at 1062 - 1092 cm^{-1}. Vibrations of the Q-species of aluminosilicate glasses superimpose this signal. Multiple Gaussian peaks are fitted

to this high-frequency region in an iterative process after applying a third order polynomial baseline in order to separate the carbonate signal. The technique has a high special resolution and can be used for high CO_2 concentrations above 0.2 wt% .

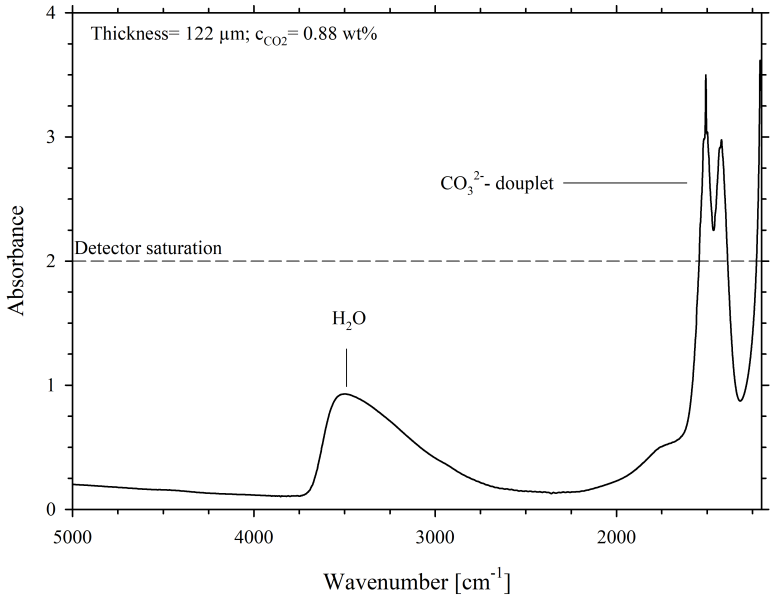

Figure 4.1: FTIR MIR absorption spectrum measured in transmission of the sample SULm-3.0. The CO_3^{2-} doublet of the spectrum is oversaturated at a thickness of 122 µm. A sample thickness of ∼60 µm would be required to quantify the CO_2 content. For samples of higher CO_2 content this problem intensifies (e.g. 15 µm for 4 wt% CO_2).

The most used method to analyse CO_2 concentration in silicate glasses is the Fourier-Transform Infrared Spectroscopy (FTIR). This is a vibration spectroscopic technique recording the interaction of electromagnetic radiation with vibration occurring at the molecular level, more specifically, the absorption of the infrared radiation. In the case of silicate glasses, the antisymmetric stretching vibrations of CO_2 and the carbonate groups are well separated from the absorbance bands of the glass matrix. The quantification of CO_2 and CO_3^{2-} is done by correlating the background subtracted Absorbance to the concentration using the Lambert-Beer law. This method however requires a calibration by an independent absolute method such as CSA for each melt composition. Moreover, it is limited to low CO_3^{2-} concentrations due to detector saturation even when using thin samples as demonstrated in Fig. 4.1. Altogether, this technique has many advantages: it is non-destructive, measures concentrations down to ppm level

and delivers information on molecular CO_2 and CO_3^{2-} groups in the analysed glass. In addition, FTIR also measures the H_2O content and speciation in silicate melts using the same technique. Lowenstern & Pitcher (2013) presented a calibration for Attenuated Total Reflectance (ATR) micro-FTIR for H_2O analyses in hydrous trachytic glasses. In addition, they observed that basaltic, basaltic andesite and dacitic glasses of known H_2O concentrations were falling along a density-adjusted calibration, allowing for quantification of water contents in calc-alkaline melts.

In this study, we introduce an alternative method to quantify CO_3^{2-} contents in CO_2-bearing glasses on the example of leucititic melts. Although the ATR-FTIR technique is less sensitive than the normal transmission FTIR, it can be very useful in the case of high CO_2 contents. It can be also valuable to quantify CO_2 contents in vesiculated samples, i.e. residual melts within crystals, since its penetration depth is only few μm and is capable of measuring spots of diameters down to approx. 5 µm. In addition, it simplifies the sample preparation, since only one side of the glass sample needs to be polished. This method can be applied to glasses with CO_3^{2-} concentration down to 0.17 wt%.

4.3 Method

4.3.1 Sample preparation

For application of this method, we synthesized a crystal and bubble free leucitite glass of the "SULm" composition from Freda et al. (2011). The homogeneity and composition of the glass were checked using a Bruker M4 Tornado micro-X-ray fluorescence (µ-RFA) spectrometer and are listed in Table 4.1. The nominally dry starting glass was saturated with CO_2 over 0.5 - 6 hours using an excess of $Ag_2C_2O_4$ as a source for CO_2 at 1375 °C and nominal pressures from 10 – 20 kbar using a piston cylinder press. For lower pressures (0.5 - 5 kbar) the nominally dry starting glass powder was saturated with CO_2 over 44 – 96 h in an IHPV at 1250 °C and an intrinsic oxygen fugacity of NNO + 3 ± 1 (see Table 4.2). The sample capsules were cut parallel to the longest axis using a Well 3242 precision diamond wire saw with a 130 µm thick wire. The smaller part of the sample was embedded in epoxy and polished on one side for ATR FTIR measurements.

Table 4.1: Glass compositions measured by micro-XRF analysis

	SiO_2	TiO_2	Al_2O_3	Fe_2O_3	MnO	MgO	CaO	Na_2O	K_2O	P_2O_5
SULm	44.75 (15)	0.97 (1)	16.63 (13)	10.77 (7)	0.27 (1)	4.03 (12)	10.97 (5)	2.50 (21)	9.11 (4)	
GKH	75.10 (21)	0.23 (1)	13.11 (9)	1.78 (3)	0.04 (1)	0.33 (6)	0.87 (2)	2.89 (23)	5.63 (4)	0.03 (2)
OTG	76.35 (25)	0.19 (1)	12.82 (9)	1.53 (3)	0.03 (1)	0.32 (6)	0.29 (1)	2.93 (29)	5.51 (5)	0.03 (3)

Micro-XRF analyses are based on 20 measurements on a large fragment of the glass
Element concentrations obtained by the standardless µ-XRF analysis were corrected using a set of 50 natural and synthetic aluminosilicate glasses with known compositions
All values show content in wt%
2σ (last decimals) is given in parentheses
All iron is given as Fe_2O_3

4.3.2 ATR-FTIR measurements

µ-ATR FTIR measurements are performed with a conventional Bruker Vertex 70 IR Spectrometer attached to a Bruker Hyperion 3000 IR Microscope. This Microscope is equipped with a 20x µ-ATR objective that has a Germanium crystal with a truncated, circular tip (d= 100 µm). The Ge crystal has a refractive index of 4.0 and an average angle of incidence at 30 °. The IR beam if focussed onto the tip of the Ge crystal and undergoes a total internal reflection on the contact surface with the sample. An evanescent field is created that is entering the medium with a lower refractive index (e.g. the sample). This evanescent field has vector components in all special orientations, can therefore interact with dipoles in all orientations. Knowing the refractive index of a basaltic glass 1.6 (Church & Johnson 1980) one can calculate the penetration depth of the beam to be 3 µm at 1430 cm^{-1} (Mirabella Jr. 1985). The beam size is defined by an optical aperture to a rectangular measurement spot and can be as small as 5 $µm^2$. Due to the small spot size and penetration depth, this setup allows for measurements of very small melt volumes such as melt inclusions. It has to be mentioned at this point that even though very small spot sizes are achievable it is recommended to use a spot size as large as possible (max. 20 $µm^2$) due to better signal to noise ratios which is critical in particular for lower CO_2 contents below 1 wt% . In contrast to regular transmission FTIR measurements the intensity of the resulting IR spectrum does not depend on the thickness of the sample but instead on the quality of the contact between the Ge crystal and the sample.

Table 4.2: Experimental conditions and volatile contents

Sample	Glaspowder [mg]	$Ag_2C_2O_4$ [mg]	H_2O [mg]	Duration [h]	Pressure [kbar]	Temperature [°C]	H_2O (IR) [wt%]	[a]A_{1430}	[a]Int_{970}	[a]A_{norm}	CO_2 (ATR) [wt%]	CO_2 (CSA) [wt%]
SULm-0.5	201.1	54.6		71	0.5	1250	0.35 (2)	0.004	100.89	0.38	0.17 (3)	0.15 (1)
SULm-1.0	202.4	54.7		72	1.0	1250	0.47 (5)	0.007	98.07	0.70	0.31 (1)	0.31 (3)
SULm-1.5	201.6	54.5		44	1.5	1250	0.36 (2)	0.009	94.46	0.91	0.40 (12)	0.40 (1)
SULm-2.0	202.1	55.7		47	2.0	1250	0.50 (3)	0.013	99.10	1.35	0.59 (3)	0.54 (2)
SULm-2.5	201.9	57.0		17	2.5	1250	0.37 (12)	0.015	98.54	1.51	0.66 (2)	0.64 (5)
SULm-3.0	200.6	58.0		76	3.0	1250	0.65 (3)	0.020	99.29	2.01	0.88 (1)	0.84 (6)
SULm-5.0	200.1	26.5		93	5.0	1250	n.d.	0.026	92.77	2.93	1.23 (4)	1.14 (8)
[c,d]SULm-10	70.2	10.8		0.5	9.0	1375	n.d.	0.039	96.30	4.04	1.77 (10)	1.82 (6)
[d]SULm-15	76.6	23.5		18.5	13.5	1375	n.d.	0.070	99.21	7.01	3.07 (4)	3.11 (12)
[d]SULm-20	70.0	27.0		22.5	18.0	1375	n.d.	0.093	95.47	9.73	4.27 (19)	4.28 (14)
SULm-40	203.2	46.3	8.6	76	3.0	1250	3.58 (16)	0.015	98.43	1.57	0.69 (1)	
SULm-80	201.9	19.8	20.6	76	3.0	1250	6.29 (45)	0.009	98.33	0.90	0.39 (1)	
GKH-C2	240.1	9.6		136	2.0	1200	1.0					[b]0.10
GKH-C1	209.4	11.8		116	3.0	1105	0.2					[b]0.17
OTG-C	241.5	6.2		93	5.0	1250	0.2					[b]0.27

A_{1430}= Peakheight of the 1430 cm^{-1} carbonate band; Int_{970}= Integral of the 970 cm^{-1} SiO_2 band; A_{norm}= normalized peakhight ot the 1430 cm^{-1} carbonate band

ε_{5200}= 1.00; ε_{4500}= 0.42 from Schanofski et al. (2019) were used for NIR H_2O determination of SULm samples.

ε_{3600}= 75 from Okumura et al. (2003) were used for MIR H_2O determination of GKH and OTG samples

2σ error (last decimals) is given in parentheses for H_2O and CO_2 values

[a]Average value of three measurements

[b]was determined by transmission MIR FTIR using ε_{2350}= 1214 from Behrens et al. (2004)

[c] experimental temperature uncertain due to thermocouple failiure

[d] Pressure in Piston Cylinder experiments was corrected for 10 % friction

4.3.3 Application of the technique

Carbon adhesive tape was used to fix the epoxy embedded samples on the microscope stage in order to prevent the sample from shifting during movement of the sample stage. Typically, 32 scans with a spectral resolution of 4 cm^{-1} from 4000 cm^{-1} to 600cm^{-1} were collected with a liquid N_2 cooled MCT detector using a Globar light source and

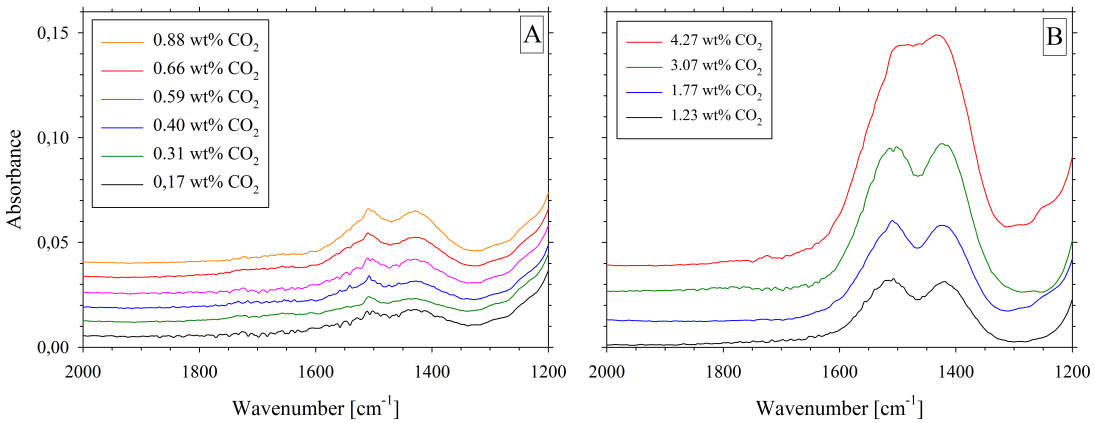

Figure 4.2: ATR FTIR spectra of all nominally dry samples of the SULm composition with (**A**) CO_2 contents below 1 wt% and (**B**) CO_2 contents above 1 wt%. Legends and spectra are organized in the same order. All spectra shown are from nominally dry samples. Spectra are normalized for Int_{970} and shifted in y-direction for better visibility. The enhanced spectral noise in the range of about 1850 to 1450 cm^{-1} is due to rotational-vibrational transitions of the bending mode of atmospheric H_2O molecules in the beam path.

a KBr beam splitter. For both, reference spectra (measured in air) and sample spectra the beam size was set to 30 x 30 µm. Pressure steps from 1 - 5 can be chosen for the contact pressure of the Germanium crystal with the sample, reflecting a force of 0.5 - 8 N. We found a pressure step of 3 to be sufficient for a reliable contact and reproducible peak heights in our epoxy embedded silicate glasses. The CO_3^{2-} doublet has shown to nicely separate from the SiO_2 lattice vibrations in ATR measurements and the entire suite of spectra for CO_2 saturated glasses from 0.17 – 4.27 wt% is shown in Fig 4.2.

4.4 Results

4.4.1 Calibration of ATR-MIR Absorbance

Since the absorbance of the MIR spectrum is highly dependent on the contact of the Germanium crystal with the sample, the spectra need to be calibrated for the quality of the contact. The baseline corrected area of the SiO_2 lattice vibration band at 970 cm−1 has shown to be a good indicator for this contact in silicate glasses and is therefore used for this purpose (Fig. 4.3). A factor of 10000 is applied to obtain convenient numbers.

$$A_{norm} = 10000 * \frac{A_{1430}}{Int_{970}}, \tag{4.1}$$

where A_{norm} is the normalized peak height of the 1430 cm^{-1} CO_3^{2-} band, A_{1430} is the baseline corrected peak height of the 1430 cm^{-1} CO_3^{2-} vibration and Int_{970} is the Integral of the baseline corrected SiO_2 lattice vibration at 970 cm^{-1}.

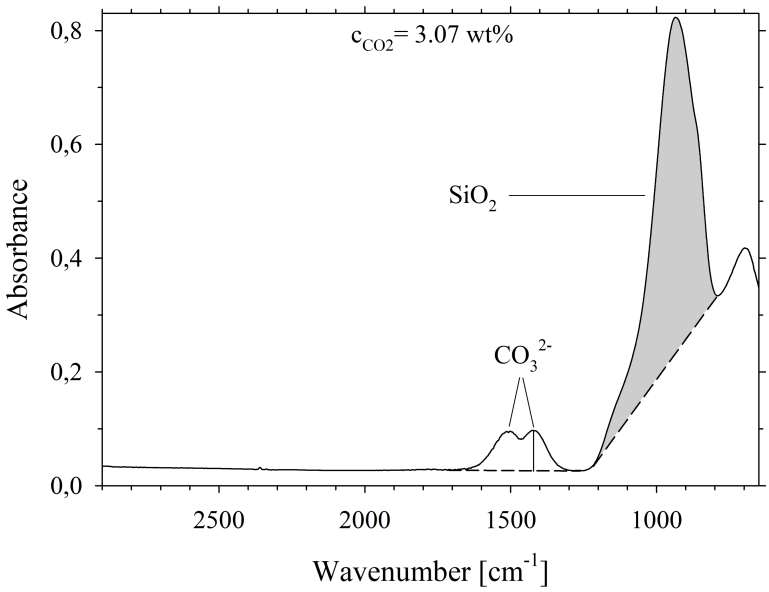

Figure 4.3: ATR FTIR spectrum of the sample SULm-15. Dashed lines are baselines applied for determination of the CO_3^{2-} peakheight at 1430 cm^{-1} and the integral of the SiO_2 lattice vibration at 970 cm^{-1}. The Integral of the SiO_2 band is used normalize the spectrum for the quality of the contact between the ATR accessory and the sample (Eq. 4.1)

In order to relate the measured, normalized peak heights to CO_2 concentrations we per-

formed a minimum of three Carbon Sulfur Analyzer (CSA) measurements per sample depending on the amount of available material and estimated CO_2 content in comparison to the detection limit of the CSA. Since bubbles trapped in the glass would dramatically increase the measured CO_2 content, the glassy samples were grounded to a coarse powder in order to crack existing volatile bubbles that are trapped in the glass. The power was checked for remaining closed bubbles in transmitted light using a stereo microscope with 40x magnification. The powder was stored in a drying furnace over night to crack open any residual bubbles by overpressure of the trapped volatile phase at 130 °C. Normalized peak heights calculated after Eq. 4.1 and CO_2 values measured by CSA are listed in Table 4.2. We found a linear correlation between the measured CO_2 concentration and the normalized peak height of the 1430 cm^{-1} band and calculated a correlation coefficient of k_{1430}= 2.28 ± 0.02 (Fig. 4.4).

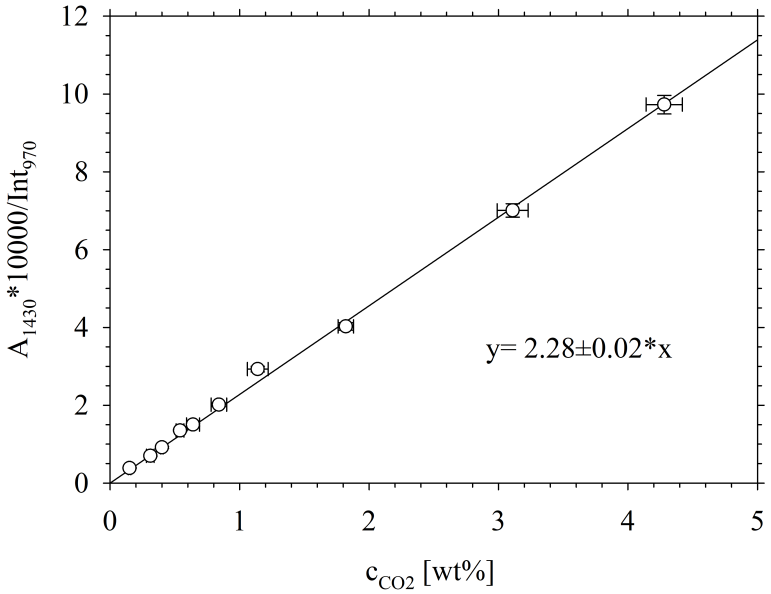

Figure 4.4: Normalized peak height A_{norm}norm vs. CO_2 content measured by CSA for all nominally dry samples of the SULm composition. Error bars represent the error propagation of 2σ errors of A_{1430} and Int_{970} parallel to the y-axis and the 2σ error of repeated CSA measurements of each sample parallel to the x-axis. Solid, straight line resembles a linear regression forced through the zero intercept. The slope of the regression is the correlation coefficient k_{1430}= 2.28 ± 0.02.

4.5 Discussion

4.5.1 Limitations

Here we synthesized glasses with CO_2 contents down to 0.17 wt% to demonstrate the capability of measuring low CO_2 contents. The relative error of this sample is quite high with 12 % as a result of the small peak height and the interference produced by atmospheric water that gets more and more relevant during measurement of small 1430 cm^{-1} peak heights. The OPUS software has an option to automatically remove atmospheric H_2O from the spectrum. We chose to do repeated measurements for good spectra with minimal atmospheric water instead of using this automatic procedure since a perfect separation of atmospheric water and the CO_3^{2-} band is questionable.

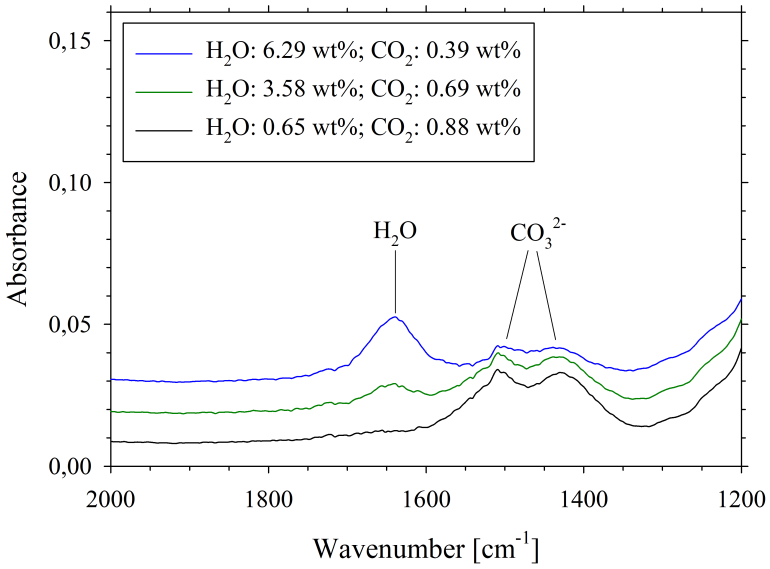

Figure 4.5: ATR FTIR spectra for H_2O bearing samples of the SULm composition in comparison to the nominally dry sample SULm-3.0 on the very bottom. Spectra are normalized for Int_{970} and shifted in y-direction for better visibility. The enhanced spectral noise in the range of about 1850 to 1450 cm^{-1} is due to rotational-vibrational transitions of the bending mode of atmospheric H_2O molecules in the beam path.

Due to the nature of the technique a certain stability of the measured samples is mandatory to realize the contact pressure of the Germanium crystal onto the sample. Measurements of foamy samples (e.g. pumice) cannot be realized and also thin sample wavers (< 100 µm) can break into pieces in some cases. That being said we were able

to use this technique for highly porous (up to 30 vol%) experimental samples embedded in epoxy and samples with complex fractures without any damage.

Since H_2O bearing samples (Fig. 4.5) show a H_2O vibration at 1640 cm^{-1} it is recommended to only use the 1430 cm^{-1} band for quantification of CO_3^{2-} in silicate glasses, since the peak height of the 1510 cm^{-1} CO_3^{2-} vibration might be slightly increased by a contribution of the H_2O vibration.

Even though it is possible to measure low CO_2 concentrations (down to 0.17 wt%), this method is most useful for silicate glasses with high CO_2 contents. This is opposite to regular transmission FTIR spectra that show a much higher sensitivity for CO_3^{2-} but, depending on the thickness of the sample quickly reach the detection limit in samples with high CO_3^{2-} contents. An advantage of µ-ATR FTIR spectra over other spectroscopic methods is the clear separation of the Carbonate doublet from the SiO_2 lattice vibrations allowing for a straight baseline. Transmission FTIR spectra often require a more complex baseline subtraction due to the overlapping of the CO_3^{2-} vibrations and silicate network vibrations. As shown by Morizet et al. (2013) the quantification of CO_3^{2-} with micro-Raman spectroscopy also requires a complex baseline subtraction as the Q-species of aluminosilicate glasses superimpose the CO_3^{2-} signal. A third order polynomial baseline needs to be applied before fitting multiple Gaussian peaks to in an iterative process in order to separate the carbonate signal.

4.5.2 CO_2 solubility of the SULm composition

Despite the demonstration of the ATR technique itself, the samples synthesized during this project can complement to the dataset of Schanofski et al. (2019) for the maximum solubility of CO_2 in the leucititic SULm composition at pressures above 3 kbar (Fig. 4.6). The samples that were synthesized using the Piston Cylinder Apparatus were equilibrated at 1375 °C compared to 1250 °C for IHPV samples. Thibault & Holloway (1994) found a strong, negative effect of temperature on the solubility of CO_2 in another Ca-rich leucitite melt. In order to compare our datasets from different temperatures, we employed a correction to our 10 – 20 kbar samples, based on the dataset of Thibault & Holloway (1994). A constant factor of 1.159 was applied to extrapolate the data to 1250 °C at constant pressure. The extrapolated data of the Piston Cylinder

experiments are in very good agreement with the CO_2 solubility below 5 kbar showing a linear increase with pressure.

During synthesis of the high pressure samples, we discovered an aragonite nanolite quench phase that crystalized in samples quenched from high pressures and was very prominent in samples with a low quench rate (40 °C/s vs. 120 °C/s). Fig. 4.7 shows the appearance of aragonite bands in the ATR spectra compared to a spectrum of pure aragonite powder measured with the diamond ATR unit of the FTIR spectrometer. In extreme cases the $\nu 3$ vibration of Aragonite is superimposed to such extend with the carbonate doublet, that it is impossible to evaluate the 1430 cm^{-1} band.

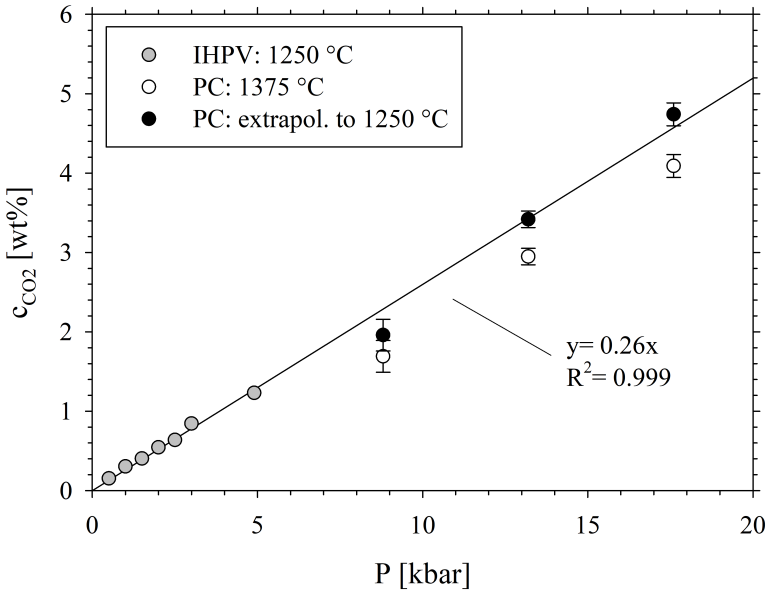

Figure 4.6: CO_2 solubility as a function of pressure for all nominally dry samples of the SULm composition. Grey data points are samples synthesized in the IHPV at 1250 °C. Errors are within the symbol size. White datapoints are samples synthesized in the Piston Cylinder Apparatus at 1375 °C corrected for 10 % friction. The CO_2 solubility of the samples synthesized at 1375 °C was extrapolated to 1250 °C for comparison (see text for details). Solid straight line resembles the linear regression of all datapoints (with exception of SULm-10 due to thermocouple failure during the experiment) and demonstrates the linear dependence of the CO_2 solubility on pressure.

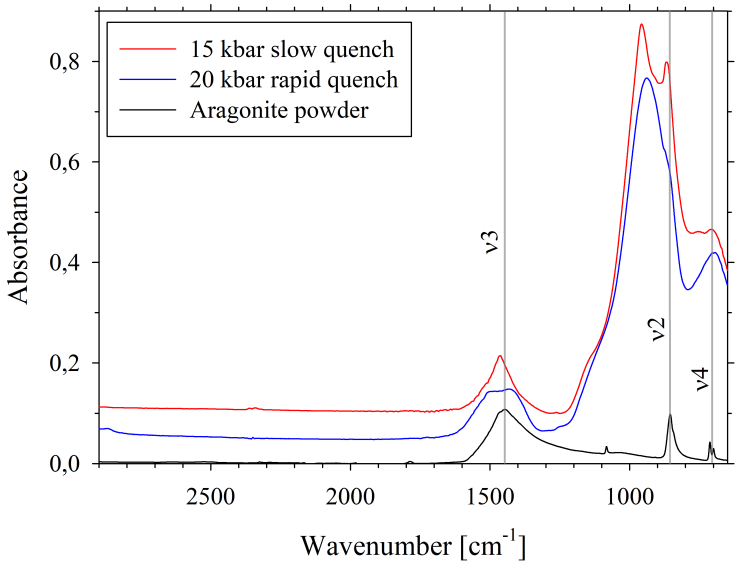

Figure 4.7: ATR FTIR spectra of samples containing Aragonite quench crystals to different extend. A scaled spectrum of Aragonite powder measured by a diamond ATR-unit is shown for comparison. Spectra are shifted in y-direction for better visibility.

4.5.3 Measuring molecular CO_2

More silicic compositions tend to incorporate CO_2 in the form of molecular CO_2 instead of or in combination with CO_3^{2-}. In transmission the molecular CO_2 band at 2350 cm-1 tends to show similar problematics as the CO_3^{2-} doublet by reaching strikingly high absorbances when CO_2 concentrations exceed 0.3 wt%, forcing the sample waver thickness down below 100 µm for quantification of the signal. In an attempt to quantify molecular CO_2 using ATR-FTIR, we saturated a natural granitic melt of the Okertal-granite and the Knaupsholz-granite with CO_2 using oxalic acid as a source for CO_2. Samples were synthesized at 2, 3 and 5 kbar, obtaining CO_2 concentrations of 0.10 wt%, 0.17 wt% and 0.27 wt% respectively as calculated from transmission FTIR measurements using an ε_{2350} value of 1214 from Behrens et al. (2004). Experimental conditions and volatile contents are listed in Tab. 4.2. ATR spectra of the granitic samples are shown in Fig. 4.8.

Background spectra, show a large variation in the area of molecular CO_2. This variation is due to atmospheric CO_2 that is present in the open parts of the Microscope.

Depending on the fluctuation, atmospheric CO_2 can either produce a positive signal (if the background measurement had less atmospheric CO_2 than the sample measurement), or a negative signal (if the background measurement had more atmospheric CO_2 than the sample measurement). Measuring molecular CO_2 using the µ-ATR method is highly affected by the atmospheric CO_2 signal due to the following reasons:

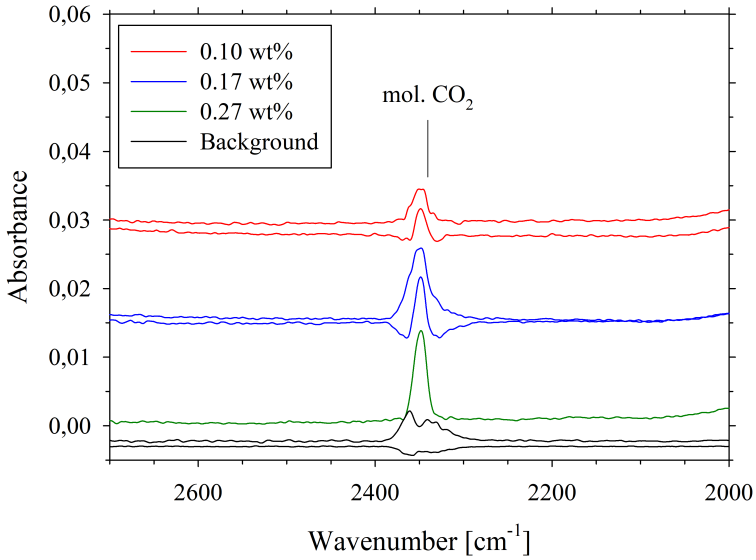

Figure 4.8: ATR FTIR spectra of granitic samples GKH-C2, GKH-C1 and OTG-C from top to bottom. In these samples all CO_2 is dissolved as molecular CO_2. Two spectra are shown for GKH-C2 and GKH-C1 respectively to demonstrate the variety of collected spectra due to variations in atmospheric CO_2. Background spectrum at the very bottom is shown for visual evaluation of the effect of atmospheric CO_2 in a best-case scenario. Spectra are shifted in y-direction for better visibility.

[1] The penetration depth of the evanescent wave is decreasing with and increasing wavenumber of the signal. At 2350 cm^{-1} the penetration depth is 1.5 µm (Mirabella Jr. 1985) effectively decreasing the signal of the band by half compared to the 1430 cm^{-1} CO_3^{2-} band.

[2] Even though the absorbance of molecular CO_2 in the sample is two orders of magnitude lower than in transmission measurements, the signal of atmospheric CO_2 in the beam path is almost unchanged compared to transmission measurements as mentioned by Lowenstern & Pitcher (2013). Therefore, atmospheric CO_2 in the beam path, which

shows a signal at the same wavenumber, strongly affects the peak shape and height of molecular CO_2 dissolved in the glass. The atmospheric correction tool of the OPUS software is not able to differentiate between these two overlapping signals and can therefore not be used to improve the sample spectra.

In order to minimize the atmospheric CO_2 signal we used two approaches. In a first attempt we purged the spectrometer with dry air for 48 h before measuring, whereas we purged the spectrometer and the microscope with gasous N_2 (99.999 % purity) using a high flux of 1000 l/h in a second one. As suggested by Lowenstern & Pitcher (2013) we covered the microscope and sample stage with a plastic shroud to allow for a N_2 atmosphere to build up in the open parts of the microscope.

Both techniques provided very comparable results. We failed to consistently measure the same amount of atmospheric CO_2 during background and sample measurements, resulting in complex and varying peak shapes in repeated measurements. The error for the quantification of molecular CO_2 introduced by atmospheric CO_2 was too large to make this a compelling alternative to transmission measurements.

4.5.4 Implications

We introduced a new and easy to use technique for quantification of CO_3^{2-} in silicate glasses. A clear linear dependence of the normalized 1430 cm^{-1} peakheight on the CO_2 content measured by CSA was found and a linear correlation coefficient (k_{1430}) of 2.28 $\pm$ 0.02 was calculated for the studied leucititic composition. The main advantages of this technique over transmission FTIR are a low afford sample preparation by requiring only one polished surface and an independence of the absorbance on the sample thickness, allowing for quantification of high CO_2 concentrations. Compared to Raman spectra, the CO_3^{2-} band is not interfered by the Q species signals of silicate network vibrations. As a result, a simple straight baseline can be applied for the carbonate doublet in ATR FTIR spectra. Additionally, ATR FTIR signals refer to a fixed sample volume that is being analysed resulting in a good reproducibility whereas the Raman signal highly depend on the focus plane.

Up to this point the main limitation for CO_2 quantification using the ATR FTIR technique is the restriction to compositions where CO_2 is bound as CO_3^{2-} exclusively since the molecular CO_2 signal in strongly interfered by atmospheric CO_2. Since the biggest factor for atmospheric CO_2 is the fluctuation of atmospheric CO_2 in the open parts of the Microscope, one may require a dedicated chamber around the microscope that can be purged with e.g. gaseous N_2 to efficiently eliminate the signal of atmospheric CO_2 and obtain consistent spectra.

References

Behrens, H., Ohlhorst, S., Holtz, F., & Champenois, M. (2004). CO_2 solubility in dacitic melts equilibrated with H_2O-CO_2 fluids: Implications for modeling the solubility of CO_2 in silicic melts. *Geochimica et Cosmochimica Acta*, 68(22), 4687–4703.

Church, B. N. & Johnson, W. M. (1980). Calculation of the refractive index of silicate glasses from chemical composition. *Geological Society of America Bulletin*, 91(10), 619.

Freda, C., Gaeta, M., Giaccio, B., Marra, F., Palladino, D. M., Scarlato, P., & Sottili, G. (2011). CO_2-driven large mafic explosive eruptions: the Pozzolane Rosse case study from the Colli Albani Volcanic District (Italy). *Bulletin of Volcanology*, 73(3), 241–256.

Lowenstern, J. B. & Pitcher, B. W. (2013). Analysis of H_2O in silicate glass using attenuated total reflectance (ATR) micro-FTIR spectroscopy. *American Mineralogist*, 98(10), 1660–1668.

Mirabella Jr., F. M. (1985). Internal Reflection Spectroscopy. *Applied Spectroscopy Reviews*, 21(1-2), 45–178.

Morizet, Y., Brooker, R. A., Iacono-Marziano, G., & Kjarsgaard, B. A. (2013). Quantification of dissolved CO_2 in silicate glasses using micro-Raman spectroscopy. *American Mineralogist*, 98(10), 1788–1802.

Mysen, B. O., Eggler, D. H., Seitz, M. G., & Holloway, J. R. (1976). Carbon dioxide in silicate melts and crystals; Part I, Solubility measurements. *American Journal of Science*, 276(4), 455–479.

Okumura, S., Nakamura, M., & Nakashima, S. (2003). Determination of molar absorptivity of IR fundamental OH-stretching vibration in rhyolitic glasses. *American Mineralogist*, 88(11-12), 1657–1662.

Pan, V., Holloway, J. R., & Hervig, R. L. (1991). The pressure and temperature dependence of carbon dioxide solubility in tholeiitic basalt melts. *Geochimica et Cosmochimica Acta*, 55(6), 1587–1595.

Schanofski, M., Fanara, S., & Schmidt, B. C. (2019). CO_2–H_2O solubility in K-rich phonolitic and leucititic melts. *Contributions to Mineralogy and Petrology*, 174(6).

Thibault, Y. & Holloway, J. R. (1994). Solubility of CO_2 in a Ca-rich leucitite: effects of pressure, temperature, and oxygen fugacity. *Contributions to Mineralogy and Petrology*, 116(1-2), 216–224.

5

Conclusions and Outlook

For the last chapter of this PhD thesis I will embed the previous chapters 2, 3 and 4 into a broader context in the form of a general conclusion and give an outlook to suggested research projects that might contribute to the presented studies.

5.1 Insights on alkali-rich volcanic eruptions from solubility and decompression experiments

Even though common empirical solubility models (e.g., Papale et al. 2006, Iacono-Marziano et al. 2012) predict the water solubility of alkali-rich melts reliably, H_2O-CO_2 solubility experiments carried out for **study I** (50 – 300 MPa; 1250 °C) have shown that the CO_2 solubility for these melt compositions is not predicted correctly. The mismatch between our experimental data and the model predictions increases with increasing pressure. Enlarging the experimental database of empirical volatile solubility models by implementation of our data could improve predictions for alkali-rich compositions. Additionally, we found evidence for the depolymerizing effect of water on the melt resulting in elevated CO_2 solubility in the fairly polymerized VES79 melt. This effect is clearly visible when plotting CO_2 solubility as a function of CO_2 fugacity, as the data of mixed H_2O-CO_2 bearing samples show a positive deviation from the trend of pure CO_2 bearing samples. Precise knowledge of the volatile solubility is mandatory for the calculation of decompression induced volatile supersaturation. The volatile supersaturation is a major driving force for magma uplift and has a large effect on the

explosivity of an eruption.

In **study II** we were focusing our attention on the SULm composition which is capable of dissolving large amounts of CO_2 (up to 8500 ppm at 300 MPa and 1250 °C). Continuous decompression experiments were performed with a decompression rate of 1 MPa/s at 1250 °C from 200 MPa to final pressures of 150, 100, 50 and 30 MPa. Here we developed a new technique for measurements of the glass porosity taking the entire sample capsule into account. This technique gives results that are very close to calculated theoretical porosities. Furthermore, we discovered a significant effect of CO_2 on the H_2O degassing behavior. In the mixed H_2O-CO_2 samples series, we found that CO_2 degasses extensively, prior to the onset of significant H_2O exsolution. The volatile supersaturation required for H_2O exsolution is however similar to the one of a pure H_2O system. As a result, large amounts of H_2O degas at low final pressures, benefitting from the previously formed CO_2 bubbles. This allows for an abrupt increase in porosity and might therefore increase the explosivity of H_2O-CO_2 bearing magmas significantly.

5.2 The missing link: Diffusivity of CO_2 in the presence of H_2O

To fully understand the degassing mechanisms of the SULm melt it is required to know the diffusion speed of the volatiles being dissolved in the melt. The diffusion speed of H_2O and CO_2 in the melt phase is an important factor for vesicle growth and versicle nucleation. The diffusivity of water is dependent on pressure, temperature, water content and melt composition. However as shown by (Schmidt et al. 2013), the melt composition has a minor effect on diffusivity and can therefore be reliably estimated on the basis of numerous existing studies (e.g., Fanara et al. 2013, Freda et al. 2003, Zhang et al. 2017). The diffusivity of CO_2 is considered to be almost independent of the anhydrous melt composition (Zhang & Ni 2010) and can therefore be predicted accurately for anhydrous systems. CO_2 diffusivity is assumed to be dependent on the H_2O content of the melt. Experimental data on CO_2 diffusivity in the presence of water is rare (Baker et al. 2005, Sierralta et al. 2002) and a better understanding would be highly valuable for the interpretation of volatile exsolution processes.

5.3 How µ-ATR FTIR could make CO_2 quantification easy

In **study III** we have successfully implemented a new method for quantification of CO_3^{2-} in silicate glasses using µ-ATR FTIR spectroscopy. This technique is capable of measuring CO_3^{2-} concentrations above 0.15 wt% and has advantages over other spectroscopic quantification techniques in specific use cases.

Morizet et al. (2013) established a CO_3^{2-} quantification technique for confocal micro-Raman spectroscopy. This technique requires a complicated baseline subtraction as due to Q-species vibrations of the aluminosilicate network that superimpose the CO_3^{2-} signal. In contrast the CO_3^{2-} signal in µ-ATR FTIR spectra is well separated and can be elaborated using a simple straight baseline. The standard technique for CO_2 quantification is transmission FTIR spectroscopy. This technique is much more sensitive to dissolved CO_2. As a consequence, one can measure concentrations of hundreds of ppm. This technique requires doubly polished sample wavers that have to be extremely thin when CO_3^{2-} concentrations exceed 0.5 wt%. In contrast µ-ATR FTIR spectroscopy uses samples that need only one polished surface and is independent of sample thickness.

CO_2 dissolved in silicate glasses is not exclusively bound as CO_3^{2-}. Instead, with increasing SiO_2 content, CO_2 is bound mostly as molecular CO_2 (Nowak et al. 2004). Up to this point however we were not able to use µ-ATR FTIR spectroscopy for quantification of molecular CO_2 due to superimposition of the signal by molecular CO_2 from the atmosphere inside the open parts of the microscope attached to the spectrometer. To erase the signal of atmospheric CO_2, a CO_2 free atmosphere would be required. This could be realized with a plexiglass box that covers the open parts of the microscope and the sample stage. Purging this Box with e.g. gaseous N_2 might eliminate the atmospheric CO_2 signal. This would allow for quantification of CO_2 regardless of bonding species (molecular CO_2 or CO_3^{2-}) and consequently enable CO_2 quantification for all silicate glass compositions.

References

Baker, D., Freda, C., Brooker, R., & Scarlato, P. (2005). Volatile diffusion in silicate melts and its effects on melt inclusions. *Annals of Geophysics*, 48(4/5), 699–717.

Fanara, S., Behrens, H., & Zhang, Y. (2013). Water diffusion in potassiumrich phonolitic and trachytic melts. *Chemical Geology*, 346, 149–161.

Freda, C., Baker, D. R., Romano, C., & Scarlato, P. (2003). Water diffusion in natural potassic melts. *Geological Society, London, Special Publications*, 213(1), 53–62.

Iacono-Marziano, G., Morizet, Y., Le Trong, E., & Gaillard, F. (2012). New experimental data and semi-empirical parameterization of H_2O–CO_2 solubility in mafic melts. *Geochimica et Cosmochimica Acta*, 97, 1–23.

Morizet, Y., Brooker, R. A., Iacono-Marziano, G., & Kjarsgaard, B. A. (2013). Quantification of dissolved CO_2 in silicate glasses using micro-Raman spectroscopy. *American Mineralogist*, 98(10), 1788–1802.

Nowak, M., Schreen, D., & Spickenbom, K. (2004). Argon and CO_2 on the race track in silicate melts: A tool for the development of a CO_2 speciation and diffusion model. *Geochimica et Cosmochimica Acta*, 68(24), 5127–5138.

Papale, P., Moretti, R., & Barbato, D. (2006). The compositional dependence of the saturation surface of H_2O+CO_2 fluids in silicate melts. *Chemical Geology*, 229(1-3), 78–95.

Schmidt, B. C., Blum-Oeste, N., & Flagmeier, J. (2013). Water diffusion in phonolite melts. *Geochimica et Cosmochimica Acta*, 107, 220–230.

Sierralta, M., Nowak, M., & Keppler, H. (2002). The influence of bulk composition on the diffusivity of carbon dioxide in Na aluminosilicate melts. *American Mineralogist*, 87(11-12), 1710–1716.

Zhang, L., Guo, X., Wang, Q., Ding, J., & Ni, H. (2017). Diffusion of hydrous species in model basaltic melt. *Geochimica et Cosmochimica Acta*, 215, 377–386.

Zhang, Y. & Ni, H. (2010). Diffusion of H, C, and O Components in Silicate Melts. *Reviews in Mineralogy and Geochemistry*, 72(1), 171–225.

6

Appendix

Contents of electronic Annex

A1.1..... Pdf version of this PhD thesis

A2.1..... Table of FTIR Parameters for VES79 samples

A2.2..... Table of FTIR parameters for SULm samples

A2.3..... Table of comparison between FTIR solubility results and numerical models

A3.1..... Fotos and redrawn sketches of all decompressed SULm samples

A3.2..... Density as a function of normalized H_2O peakheights

A3.3..... Density as a function of H_2O content